4-2015

Computational Modeling of β5-β6 Carbapenemase Loop in Wild Type and Selected Mutants of OXA-24 Class D β-Lactamase

James Roland LaFleur
Grand Valley State University

Computational Modeling of β5-β6 Carbapenemase Loop in Wild Type and Selected Mutants of OXA-24 Class D β-Lactamase

James Roland LaFleur

A Thesis Submitted to the Graduate Faculty of

GRAND VALLEY STATE UNIVERSITY

In

Partial Fulfillment of the Requirements

For the Degree of

Master of Science

Cell and Molecular Biology

April 2015

“There is no stronger drug than reality.”

Nevermore

DEDICATION

I would like to thank my family, Ellwood, Lorraine, and Tori for their limitless support and confidence in me; all of the Cell and Molecular Biology graduate students; and my close friends. A special thank you to Nick Reitz, for without him I would have been sleeping instead of typing a thesis at 4 in the morning. I can't even begin to fathom the amount of this work that was typed sitting at a kitchen table, with two Siberian huskies looking at us like we're crazy.

ACKNOWLEDGEMENTS

I would like to acknowledge both of my committee members, Dr. Christopher Lawrence, and Dr. David Leonard for their expertise and guidance; my adviser, Dr. Agnieszka Szarecka, for her knowledge, and support throughout this project; the Cell and Molecular Biology department; Brian Mullen, for contributing necessary code and statistical knowledge; this work was also supported by the National Center for Multiscale Modeling of Biological Systems (MMBioS) through National Institutes of Health Grant P41GM103712 (T.W.).

ABSTRACT

Bacterial resistance to antibiotic therapies, especially to β-lactams, is an increasing problem. B-lactamases are the main source of clinical resistance to these antibiotics, and the class D β-lactamases are one of the most rapidly expanding classes of these enzymes. The emergence of class D enzymes with the ability to hydrolyze the newest family of β-lactams - the carbapenems - is a serious concern for the healthcare system as carbapenems are last resort antibiotics: ideal for severe infections after other therapies have failed. Class D β-lactamases are very diverse in terms of sequence and substrate profile, and it remains unclear what factors affect the enzymes' ability to hydrolyze certain classes of antibiotics (e.g. carbapenems or cephalosporins). The β5-β6 loop has been previously shown to affect the substrate profile of OXA enzymes, for carbapenems in particular. This work examines the effects of selected mutations in the β5-β6 loop on the proteins' dynamics via Molecular Dynamics simulations. OXA-24 (a carbapenemase) and three mutants (M223A, G224D, P227S) were simulated for 40 nsec, and the trajectories revealed that all three mutations alter the dynamics of the enzyme. Our data show that the mutations affect the flexibility of several crucial segments of the enzyme structure, the overall compactness of the protein, as well as the size of the active site. Our results suggest that the β5-β6 loop can affect the substrate profile of OXA-24 by modulating the enzyme's dynamics in a way that is consistent with substrate profile expansion, in particular with the ability to bind 3rd generation cephalosporins.

TABLE OF CONTENTS

LIST OF TABLES

TABLE PAGE

LIST OF FIGURES

FIGURE PAGE

LIST OF SYMBOLS AND ABBREVIATIONS

CHARMM: Chemistry at Harvard Macromolecular Mechanics

CHDL: Carbapenem Hydrolyzing Class D β-Lactamase

CPase: Carbapenemase

E.C.: Enzyme Commission # (http://www.chem.qmul.ac.uk/iubmb/enzyme/)

ESBL: Extended-Spectrum β-Lactamase

GA: Genetic Algorithm

G224D: OXA-24 Glycine 224 to Aspartate mutation, AKA OXA-72

KCX: Carboxylated lysine. Residue 84 in OXA-24.

K_i: Inhibition constant.

M223A: OXA-24 Methionine 223 to Alanine mutation

MD: Molecular Dynamics

NPT: Isothermal-Isobaric conditions.

NVT: Isothermal-Isovolumetric conditions.

P227S: OXA-24 Proline 227 to Serine mutation, AKA OXA-160

Φ: Phi; dihedral angle between N-C-Cα-N atoms.

Ψ: Psi; dihedral angle between C-Cα-N-C atoms.

R_{gyr}: Radius of gyration.

RMSD: Root-Mean-Square Deviation

RMSF: Root-Mean-Square Fluctuation

TCL: Tool Command Language

VMD: Visual Molecular Dynamics

WT: OXA-24/40 Wild-Type

CHAPTER I

INTRODUCTION

1. Antibiotics

Antibiotics are chemical agents that impede the growth of bacteria (bacteriostatics) or kill the bacteria (bacteriocidals). There are many classes of antibiotics (Talaro 2011), including: (i) the β-lactams, targeting bacterial cell wall transpeptidases; (ii) polymyxins, targeting the bacterial cell membrane; (iii) sulfonamides, targeting dihydropteroate synthetases involved in folate synthesis; (iv) tetracyclines and (v) aminoglycosides, which target the 30S ribosomal subunit; (vi) quinolones, targeting DNA gyrases; (vii) macrolides, which target the 50S ribosomal subunit. These compounds have been extremely useful in saving lives. However, a misuse of antibiotics, both in human therapies, and in livestock, combined with a lack of understanding of the gravity of the problem led to the problem of bacterial resistance to antibiotics that we are experiencing today (Neu 1992; Bax 2001; CDC 2013). Solving this problem will require many changes, such as improved public education about antibiotics/antibiotic resistance, and removal of antibiotics from animal feed in addition to the development of novel antibiotic compounds (Bush 2011a).

1A. β-Lactam Antibiotics

β-lactam antibiotics target DD-transpeptidases (E.C. 3.4.16.4, also called penicillin binding proteins (PBPs)) in bacteria. DD-transpeptidases cross-link the peptidoglycan chains in bacterial cell walls, and are inhibited upon binding β-lactam

antibiotics. A lack of cross-links without these enzymes providing maintenance of the cell walls will result in cell death from lysis (Talaro 2011).

Unlike other antibiotics whose targets have human homologs, β-lactam antibiotics are the safest antibiotics available (Salkind 2001). They are also cheap to manufacture on a large scale, with a kilogram of penicillin costing only $15-20 at the beginning of the millennium (Elander 2003). The name β-lactam comes from the β-lactam ring (Fig. 1A), a cyclic amide that is found within all classes of related antibiotics (Fig. 1B-D).

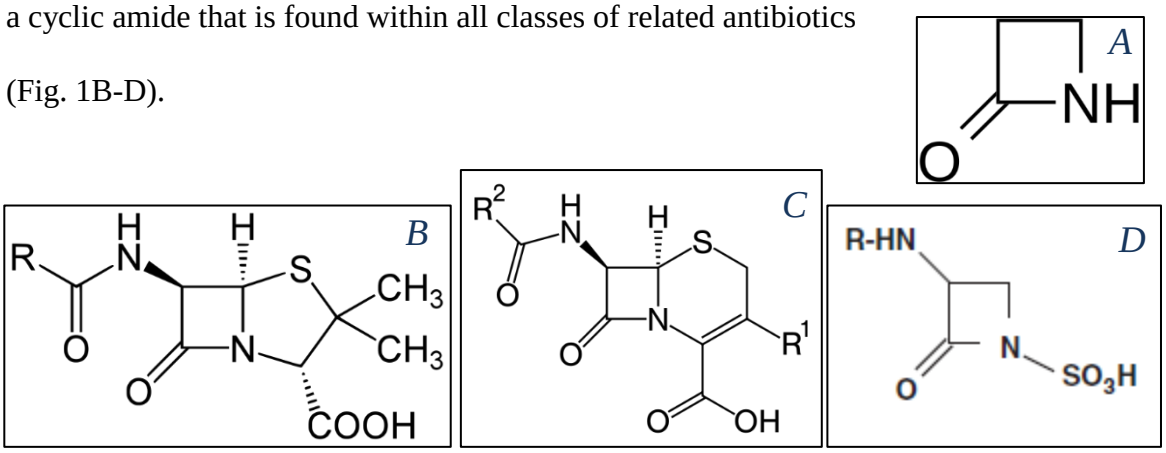

Fig. 1: β-Lactam Core Structures. *A*: β-lactam ring. *B*: Left, core structure of penicillins. *C*: Middle, core structure of cephalosporins. *D*: Right, core structure of monobactams.

The first β-lactam antibiotic discovered was penicillin in 1928 by Alexander Fleming and, it has been used clinically since the 1940s. While its discovery was an important step in treating bacterial infections, it was recognized almost immediately that penicillin was relatively ineffective against Gram-negative bacteria (Hall 1994). It was not until ampicillin entered the market in 1963 that an antibiotic was effective against both Gram-positive and Gram-negative bacteria (Medeiros 1997). However, the first penicillin resistant strain was discovered as early as 1944 (Kirby 1944). Since then multiple other types of β-lactams have been discovered and further developed, including the cephalosporins (Fig. 1B), and monobactams (Fig. 1D).

The most recent class of β-lactam antibiotics to be discovered and used clinically are the carbapenems (Fig. 2).The first carbapenem introduced into the United States was imipenem in 1987. Since then three more carbapenems have been approved for clinical use: meropenem in 1996, ertapenem in 2001, and doripenem in 2007. Carbapenem antibiotics are considered to be last resort antibiotics (Carrër 2008). While each carbapenem has a specific therapeutic role, they are generally used to treat patients with moderate to severe infections (Zhanel 2007, Keam 2008). Within the group of β-lactam antibiotics, carbapenems are considered to be clinically "stable." This term is used to describe their intrinsic resistance to many β-lactamases (i.e. β-lactamases are not able to hydrolyze the β-lactam ring in these compounds). In addition to their β-lactamase resistance, newer carbapenems are also resistant to renal dehydropeptidase (E.C. 3.4.13.19) hydrolysis, which was a common problem with imipenem. The resistance of carbapenems against most β-lactamases is attributed to a trans-α-1-hydroxyethyl group at position 6 (Fig. 2, R1 substituent). Renal dehydropeptidase resistance was accounted for due to a 1-β-methyl group placed at the R2 position (Fig. 2) (Zhanel 2007). This resistance to hydrolysis by a majority of β-lactamases made carbapenems the most important last resort clinical agents used in

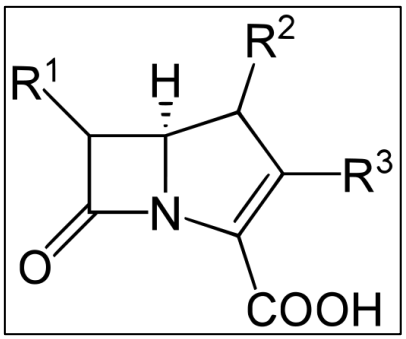

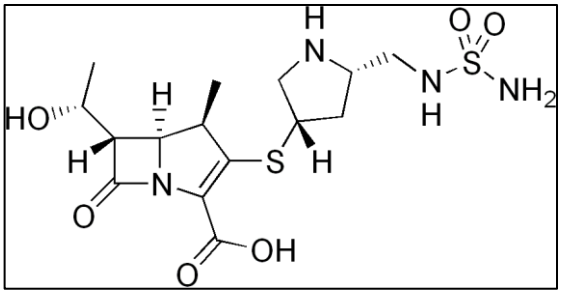

Fig. 2: Carbapenem Core Structure & Doripenem. *Top*: Core structure of carbapenems. *Bottom*: Structure of doripenem.

complicated nosocomial infections (Cornaglia 2010). Thus, emergence of strains that do inactivate carbapenems is a grave problem.

2. Clinical Aspects of Antibiotic Resistance

Many different drug-resistant bacteria species have become the root-cause of serious health complications (Sharma 2011) – a problem that is estimated to cost the U.S. economy in excess of $20 billion according to the Centers for Disease Control and Prevention (Roberts 2009; CDC 2013). Various strains of *S. aureus* are now implicated in fatal cases of sepsis, and necrotizing fasciitis due to methicillin (Boyle-Vavra 2007) and vancomycin (Bozdogan 2003) resistance. Respiratory infections as well show antibiotic resistance, with different strains of *S. pneumonia* and *S. pyogenes* providing penicillin and macrolide resistance (Albrich 2004). *Acinetobacter baumannii* has become an increasingly important pathogen, especially with bloodstream infections (CDC 2004). Much of *A. baumannii*'s resistance is due to class D β-lactamases, which will be discussed in following sections.

3. Diversity of Mechanisms of Antibiotic Resistance

Ultimately, every antibiotic exerts evolutionary pressure on bacteria to develop survival and resistance mechanisms. In the case of β-lactams, major mechanisms of resistance are: β-lactamases; the overexpression of β-lactamases in susceptible strains (Guitérrez 2007); antibiotic sensing domains (Zeng 2013); mobile genetic elements to facilitate rapid spread of resistance genes (Rumbo 2011); penicillin binding protein mutations (Katayama 2004), efflux pumps (Nakae 1999), and mutations in transporters

reducing influx and permeability of antibiotics (Li 2009). The most common mechanism is via β-lactam ring cleavage by β-lactamases.

4. β-Lactamases

4A. Classes and Diversity

β–lactamases (E.C. 3.5.2.6) are major mediators of bacterial resistance to antibiotic therapies, and pose a serious threat to the most widely used class of antibiotics (Ferech 2006). They form a large family (500+) of distinct enzymes (Bush 2010). All of these enzymes are believed to have evolved from ancestral PBPs, which helped synthesize cell walls (Kelly 1986; Massova 1998; Hall 2004)

Currently there are two classification systems for the β–lactamase family: one based on sequence similarity (Ambler 1980) and the other – based on functional profile (Bush 2010), i.e. the types of β–lactam substrates that a given subgroup can hydrolyze. According to sequence-based classification there are four classes of β-lactamases: A, B, C, and D (Hall 2005). Classes A, C, and D are serine-hydrolase enzymes (Fig. 3), while class B enzymes are metalloenzymes that use a Zn2+ ion for catalysis. In classes A, C, and D the hydrolysis process occurs in two steps: acylation of the enzyme by the antibiotic (Fig. 3A-B), and deacylation that yields in inactivated product (Fig. 3C-F).

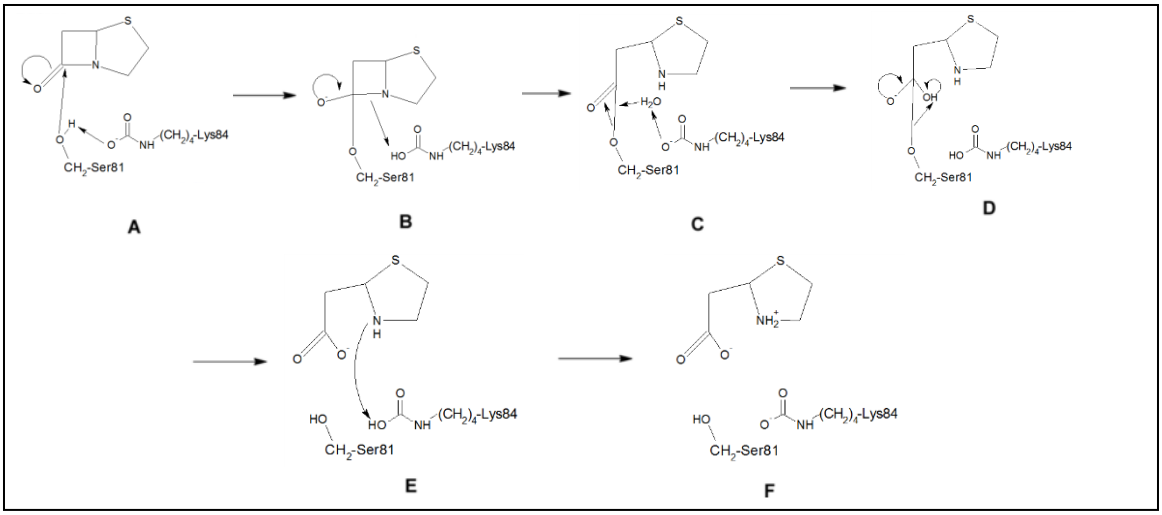

Fig. 3: Serine-based Mechanism of β-Lactam Hydrolysis. Mechanism depicts the roles of the active site serine (nucleophile), and water molecule which assists with the deacylation. The mechanism requires serine activation by a general base: a glutamate residue serves this role in class A enzymes (Matagne 1998), and a carboxylated lysine (full side chain not shown) residue in class D enzymes. Figure adapted from Che (2012).

The functional classification developed by Bush et al. (1989; 2010) divides the enzymes into groups based on their clinical activity. Factors such as substrate(s), and inhibitory molecules are taken into account. This classification has only 3 groups: Group 1 being solely cephalosporinases (class C enzymes); Group 2 being serine β-lactamases (classes A and D), containing multiple functional subgroups with some enzymes showing multispecificity towards ligands; and Group 3 being the metallo-β-lactamases (class B enzymes) (Fig. 4).

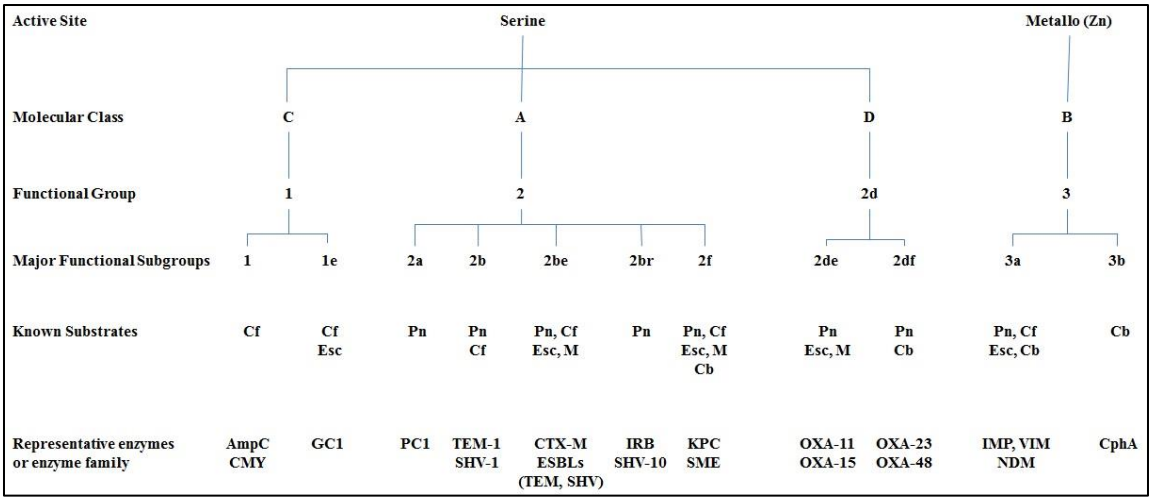

Fig. 4: Functional Classification of β-Lactamases. Abbreviations are: Cb, carbapenems; Cf, early marketed cephalosporins; CA, clavulanic acid; EDTA, ethylenediaminetetraacetic acid; Esc, Expanded spectrum cephalosporins; M, monobactam; Pn, penicillins. Figure adapted from Bush (2013).

4B. Extended-Spectrum β-Lactamases versus CPase Activity

β-lactamases that are capable of hydrolyzing third generation cephalosporins (Fig. 5), in addition to other narrow-spectrum antibiotics like penicillin are generally referred to as Extended Spectrum β-lactamases (ESBLs) (Bradford 2001). There are currently over 200 ESBLs within the molecular classes A, C, and D. Most of these enzymes do not exhibit CPase activity, and carbapenem antibiotics are thus the treatment of choice in the case of infections caused by ESBL expressing strains (Paterson 2005). However, this increased use of carbapenems in response to ESBL activity is likely a factor in applying selective pressure for organisms to acquire and express Carbapenem Hydrolyzing class D β-lactamases (CHDLs).

The molecular explanation for why certain enzymes show ESBL activity while others do not is generally attributed to the ability of the active site to accommodate the bulkier substituents that are present on third generation cephalosporins, such as

ceftazidime and ceftriaxone (Fig. 5). Specific examples will be discussed in the following sections.

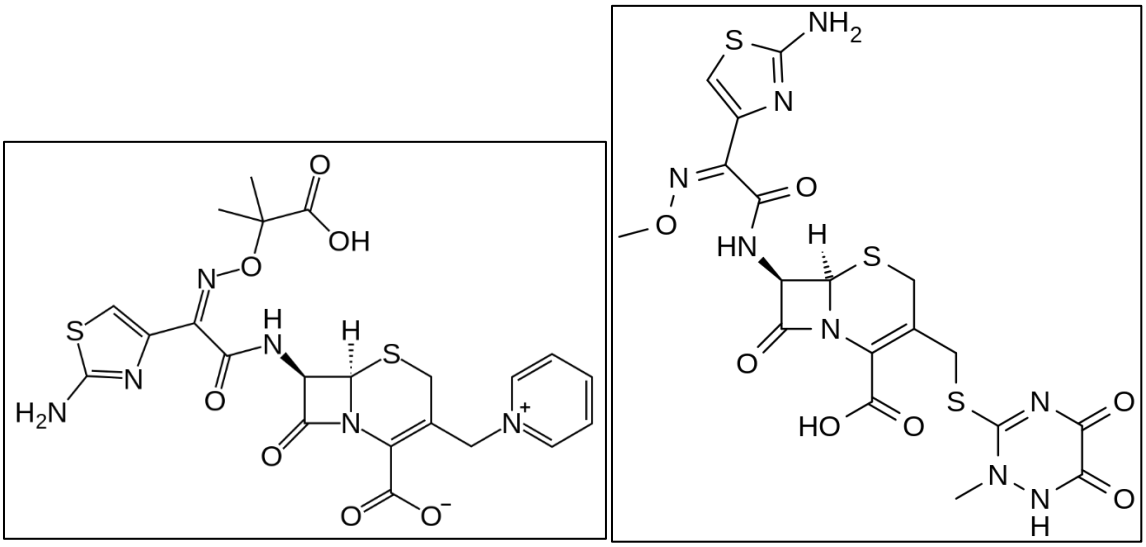

Fig. 5: Structures of Ceftazidime & Ceftriaxone. *Left*: Ceftazidime. *Right*: Ceftriaxone.

4B-1. Mutations Enlarging the Active Site Promote Cephalosporinase Activity

Numerous enzymes have gained ESBL activity through unique mutations. The class C enzyme GC1 achieved this function through a three amino acid insertion within the Ω loop (Crichlow 1999; Fig. 7). The exact sequence of the amino acids appears to play no significant role, but the length of the insertion does as it causes the Ω loop to shift and open up the active site. SHV-2, a class A enzyme, contains a Gly238Ser mutation which causes the β3 strand to shift away from the enzyme's Ω loop as Ser238 hydrogen bonds with Asn170. This ~3Å shift opens up the active site to larger substrates (Nukaga 2003). Both support the hypothesis that the size of the binding pocket is vital for accommodating large substituents. The class D enzyme, OXA-163, differs from OXA-48 (a CHDL) by a 1 amino acid substitution (S212D), and a 4 amino acid deletion (R214-P217) after the KTG family motif on the β5 strand. This sequence change causes

increased cephalosporinase activity (Poirel 2011). While the authors do not detail a structure/functional relationship for this newly gained activity, based on how previous enzymes have acquired ESBL activity the likely cause of OXA-163's ESBL activity is an opening of the active site.

Multispecificity of a β-lactamase is an undesirable trait from a clinical perspective. Since carbapenems tend to be the treatment of choice for ESBL-producing infections, and 3rd generation cephalosporins for CHDL-producing infections, bacteria which are capable of producing multispecific (i.e. both CHDL and ESBL) resistance enzymes pose a major threat to the current arsenal of antimicrobials. Any CHDL and ESBL-producing bacterium drastically limits the options for antibacterial chemotherapy to drugs with undesirable side-effects – such as those observed with linezolid, an antibiotic that when used over the long term may cause GI complications and thrombocytopenia (Kalil 2010); or polymyxins, which have shown neurotoxic effects (Grill 2011).

4B-2. OXA-24 Variant Exhibits Cephalosporinase and CPase Activity

The molecular mechanisms of ligand selection are not well understood and, given that a single amino acid substitution can have a profound effect on substrate profile (Afzal-Shah 2001; Nukaga 2003; Kaitany 2013), is it vital to elucidate (and predict) the effects of specific mutations. This can help predict evolutionary pathways of these enzymes, and perhaps lead to more effective antimicrobial chemotherapeutics. **In this project we aim to help understand the mutational effects that affect both CHDLs and ESBLs in OXA-24 and its variants.** OXA-160 is a P227S mutation of OXA-24

(Tian 2011) which confers increased resistance to third generation cephalosporins, ampicillin, and aztreonam. It increases activity against doripenem, but decreases activity against imipenem (Mitchell 2015).

4C. Class D Enzymes and OXA-24 as Focus of this Thesis

4C-1. Unique Features

There are currently over 200 unique enzymes in the class, and more are expected as the class is currently experiencing the fastest growth out of all β-lactamase subfamilies (Fig. 6). It should be noted that while the CMY class C β-lactamases, and class A KPC enzymes have higher rates of growth, the class D enzymes has the most unique enzymes of all the subfamilies.

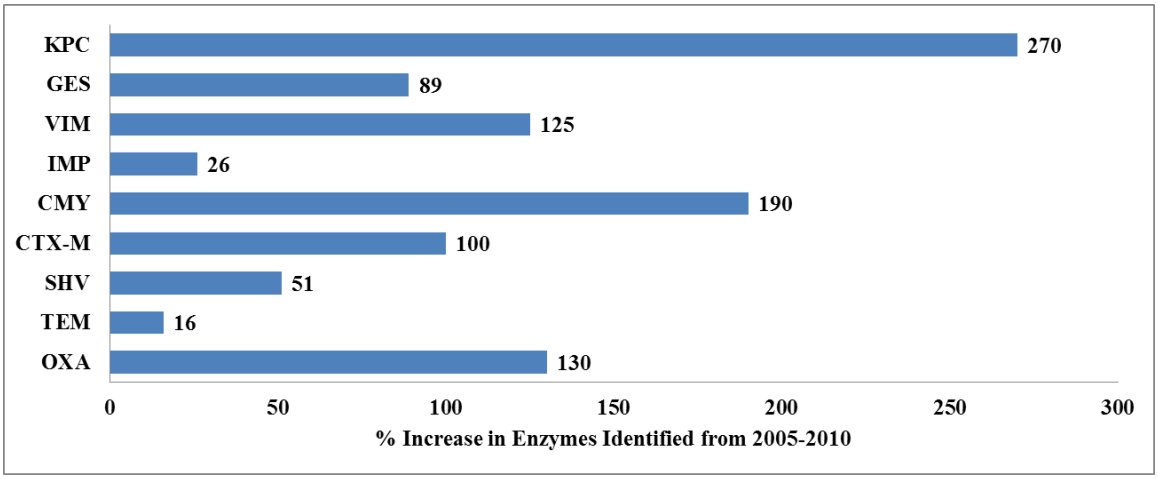

Fig. 6: Growth Rate of β-Lactamase Classes. Class D enzymes are only designated as OXA. Class A enzyme designations are TEM, SHV, CTX, GES, and KPC. Class B enzymes are IMP, and VIM. Class C enzyme family is CMY. Figure adapted from Bush et al. (2011b).

Class D β-lactamases, like the class A and C enzymes, use an active-site serine for hydrolysis (Ledent 1993), but are most likely distant relatives of these enzymes (Massova 1998) and contain many unique features. Unlike the other two classes, class D enzymes

contain a rare, modified, amino acid: a carboxylated lysine, which is critical for catalytic activity (Golemi 2001). The carboxylysine residue acts as the general base in the hydrolysis mechanism, playing a particularly essential role in the deacylation step of catalysis (Schneider 2009b).

4C-2. Conserved Motifs and Residues

In addition to the general base and catalytic serine, highly conserved motifs and residues were identified in the class D family. Highly conserved motifs include (residue numbers correspond to PDB 3ISG): P65-[AD]STFK, S115-xV, [YF]141-GN, and K212-[TS]G (Bou 2000). Highly conserved residues (>95 %) outside of those motifs are: G128, W160, I167, L184, W228, G231, and F243 as revealed by multiple sequence alignment of 80+ unique OXA sequences (Szarecka 2011).

4C-3. Structural Features

Structures of OXAs are highly conserved (as revealed by a number of crystal structures of various class D enzymes). Crystal structures are available for OXA-1 (PDB 1M6K), OXA-2 (1K38), OXA-10 (1FOF), OXA-13 (1H87), OXA-23 (4K0X), OXA-24 (2JC7), OXA-45 (4GN2), OXA-46 (3IF6), OXA-48 (3HBR), OXA-58 (4OH0), OXA-146 (4K0W), OXA-160 (4X56), and OXA-225 (4X55). The fold (Fig. 7) includes a helix-only domain, and an α/β domain. The helical domain contains the active site PASTFK motif, the P loop, and other active site stabilizing elements (e.g. Trp167). The α/β domain contains the β5-β6 loop, the K[ST]G motif, and both the N and C-termini. All of these elements will be discussed in further detail in the sections to follow.

4C-4. Class D CPases and OXA-24 Subgroup

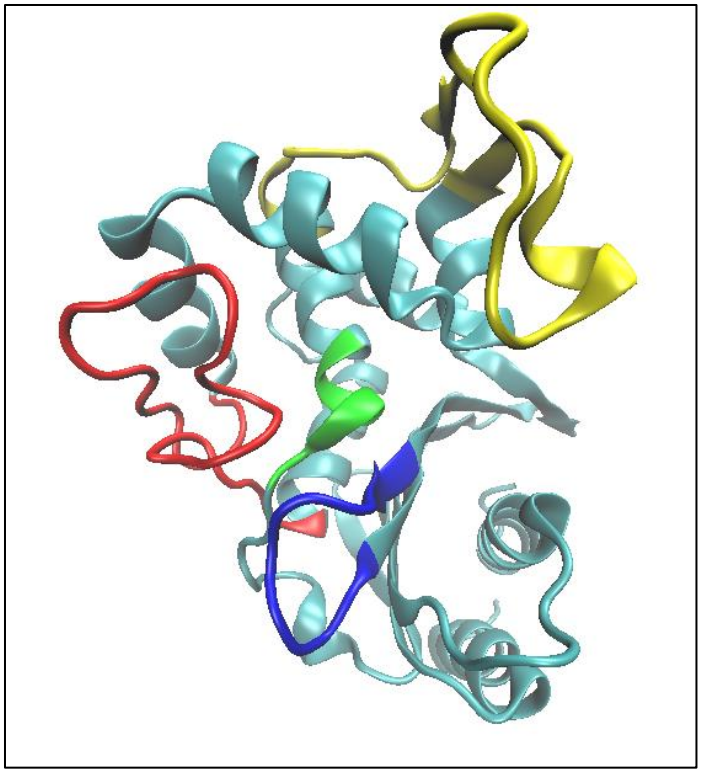

Fig. 7: Class D Conserved Secondary Elements. Catalytic PASTFK motif colored green, P loop colored yellow, Ω loop colored red, β5-β6 loop colored blue.

Fairly recently, multiple class D enzymes with CPase activity (functional subgroup 2df, Fig. 4) have been identified (Afzal-shah 2001). These newer class D members are the main source of carbapenem resistance in *A. baumannii* infections (Poirel 2006), and are becoming increasingly common (Queenan 2007). Distinct Class D CPase subgroups are OXA-23, 24, 48, 51, 58, and 228 (Bonnin 2012). **The focus of this research is on the parent enzyme OXA-24, and three OXA-24 mutants (M223A, G224D, P227S).** OXA-24 (NCBI RefSeq YP_002967455.1) is a CPase that was discovered in Spain over a decade ago in a strain of *A. baumannii* (Bou 2000). It is identical to OXA-40 and is sometimes referred to as OXA-24/40. Initially OXA-24 was thought to only be chromosomally encoded (Bou 2000), but recent studies have shown that horizontal transfer events of the $bla_{\text{oxa-24}}$ gene can occur (Rumbo 2011) resulting in an enzyme with an increased potential for pathogenic spread. OXA-24 has spread, from Spain to Portugal (Da Silva 2004), France (Quinteira 2007), Italy (D'Andrea 2009), and the United States (Tian 2011). Based on our sequence alignment OXA-24 is also a parent

enzyme to multiple variants, including OXA-25, 26, 72, 139, 143, 160, 182, 207, 231, 253, and 255. Based on the MSA I performed using M-Coffee (Wallace 2006), OXA-24 shares 99% sequence identity with OXAs-25, 26, 72, 139, 160, and 207; 88% identity with OXA-143, 231; 89% identity with OXA-182; 90% identity with OXA-253; and 87% identity with OXA-255 (Table 14, Appendix C). These group members have spread as well, such as OXA-72 in Colombia (Montealegre 2012), the United States (Tian 2011), China (Wang 2007), and Lithuania (Povilonis 2012).

OXA-24 is capable of hydrolyzing other antibiotics in addition to carbapenems. Hydrolysis of ampicillin is relatively similar to that of imipenem and doripenem (K_m/k_{cat} = 3.1 ±0.4 $\mu M^{-1}s^{-1}$ for doripenem and imipenem, 2.6 ±0.3 $\mu M^{-1}s^{-1}$ for ampicillin) (Mitchell 2015). OXA-24 binds the carbapenems much more tightly than ampicillin; the K_m for ampicillin is ~200 times greater than that of imipenem. However, OXA-24 turns over ampicillin at a much greater rate than the carbapenems (K_{cat} of 480 ±20s^{-1} for ampicillin, and 0.074 ±0.001s^{-1} and 2.1 ±0.1s^{-1} for doripenem and imipenem respectively). The hydrolysis of 3rd generation cephalosporins in quite poor: K_{cat}/K_m for cefotaxime is 0.00051 ±0.00005 $\mu M^{-1}s^{-1}$, while ceftazidime hydrolysis is not detectable (Mitchell 2015).

4D. Current Knowledge on Factors Determining ESBL or CHDL Activity in OXAs

The mechanism through which some class D enzymes acquire new function is poorly understood, and evolutionary pathways that govern the functional diversity and multispecificity within class D β-lactamases must be elucidated. Detailed information is

needed on which residues assist, and which residues hinder various stages of the catalytic cycle for various classes of β-lactams.

Several factors have been proposed in the literature with regard to the mechanism of ESBL and CHDL activities. As mentioned before, in the majority of cases, β-lactamases cannot exhibit both ESBL and CHDL activity. Thus, increased ability to hydrolyze cephalosporins reduces the ability of catalyzing carbapenems and vice-versa. OXA-160 (OXA-24 P227S) is a notable exception in this respect.

In the case of ESBL, the size of the binding pocket is vital as 3rd generation cephalosporins contain bulky substituents (Fig. 5) that need to be packed inside the active site without affecting the position of the β-lactam ring with respect to the catalytic residues. Thus, mutations that increase the size of the binding cavity should promote ESBL activity. It is equally important that no steric barriers hinder the entrance to the pocket. Indeed, Kaitany et al. (2013) suggested that the Tyr112-Met223 interaction in OXA-24 forms a bridge that prevents binding of such bulky ligands and may facilitate carbapenem binding.

In the case of CPase activity, the following factors have been proposed in the literature: (1) the ability to recruit a necessary water molecule to complete the catalytic cycle (Schneider 2009a); (2) interactions between the hydroxyl group in position R1 (Fig. 2) with the carboxylysine may diminish the latter's ability to serve as the general base (Schneider 2011); (3) intramolecular reactions such as tautomerization of the pyrroline ring within the substrate that may hinder deacylation (Schneider 2011); (4) mutations that

promote decarboxylation of the general base (Schneider 2011); (5) mutations in the loop adjacent to the catalytic center (De Luca 2011).

With regard to factor (5), a recent study by De Luca et al. (2011) reported that the β5-β6 alone is able to "switch" on the CPase activity. When OXA-10's (a non-CPase) β5-β6 sequence (residues 221-228, OXA-24 numbering) was replaced with that of OXA-24's the hybrid enzyme showed CPase activity. The authors hypothesized that the β5-β6 loop impacts the binding mode of carbapenems, facilitating hydrolysis. Thus, it is clear that this loop is involved in CHDL activity although the mechanism through which the β5-β6 loop affects substrate selection is not well understood. It should be noted that the "β5-β6" term is not technically correct when identifying the loop in OXA-24. OXA structures vary in the exact number of stands in their extended β sheet so the strand numbering varies from enzyme to enzyme. The actual loop in OXA-24 WT would be the β4-β5 loop (Fig. 36, Appendix C), but because the term was defined using OXA-48 (Docquier 2009; De Luca 2011), we have decided to continue using this nomenclature.

In addition, OXA-160 (Tian 2011) and other studies (Kaitany 2013; Mitchell 2015) revealed that single amino-acid mutations within the β5-β6 loop in CPases impart the ability to hydrolyze 3rd generation cephalosporins, i.e. a multispecific ESBL-CHDL enzyme emerged.

5. Research objectives

In light of the above findings, I have set the following aim as the research objective of my thesis:

Aim: To elucidate the mechanism through which the β5-β6 loop affects the ligand binding and selectivity of the OXA-24 enzyme, in particular the binding of 3rd generation cephalosporins and doripenem.

Hypothesis: Since the β5-β6 loop is not directly involved in the ligand binding or in hydrolysis, I hypothesize that mutations within this loop have an indirect affect – through modulating the enzyme dynamics.

Aim 1a: Analysis of Molecular Dynamics simulation trajectories of OXA-24 wild-type, M223A, G224D, and P227S mutants. Simulation trajectories (40 nsec) provide insight into the residue fluctuations in different variants, size and shape of the active site, conformational flexibility of the β5-β6 and Ω loops, and the stability of the catalytic center.

Aim 1b: Docking simulations of representative antibiotics to multiple trajectory frames. Differences in the conformational ensembles of different variants can be identified within the trajectories, and representative frames then serve as docking targets for various classes of antibiotics. This will provide insight into the ability of the variants to accommodate various types of β-lactams.

CHAPTER II

METHODS

1. Sequence Analysis

CPase sequences from the OXA-24 family were collected by performing a protein BLASTp search of the OXA-24 sequence on the non-redundant protein sequences database through the National Center for Biotechnology Information (http://www.ncbi.nlm.nih.gov/), and saving all sequences which shared ≥85% identity with OXA-24. Representative sequences from other class D families – determined via Poirel et al. (2010) - were acquired from the NCBI Protein database. This cutoff percent was self-chosen as all members of the OXA-24 subgroup share >85% identity with every other member. The lowest identity shared between two members of the OXA-24 subgroup is 86%. OXA-24 only shares 62% identity with CPase OXA-51; identities between OXA-24 and other class D CPases are lower still. Therefore, the 85% sequence identity cutoff was chosen to best represent enzymes that are currently part of the OXA-24 subgroup.

The Multiple Sequence Alignment (MSA) tool M-Coffee (Wallace 2006) was employed for motif discovery and sequence alignment. M-Coffee was run through its online server at http://tcoffee.crg.cat/apps/tcoffee/do:mcoffee (Moretti 2007). M-Coffee uses several MSA algorithms, and then combines those alignments into one, final alignment. All eight default MSA methods were utilized for aligning the collected class D sequences: PCMA (Pei 2003), POA (Lee 2002), DIALIGN-T (Subramanian 2005),

MAFFT (Katoh 2005), MUSCLE (Edgar 2004), ProbCons (Do 2005), CLUSTAL W (Thompson 1994), and T-Coffee (Notredame 2000)

2. Molecular Dynamics

2A. Theoretical Background

MD simulations are a deterministic method of modeling the physical movements of atoms within a user-defined system. While many methods exist for sampling the conformational space of proteins (e.g. Monte Carlo simulation), MD simulations allow for the conformational space to be sampled in a time-dependent manner; essentially allowing for the system to evolve on its own biological time-scale (Karplus 2002).

The determination of atomic movements requires a potential energy function; also known as a "force field." The force field approximates the energy of a system by expressing it as a function of the system's structure (atomic positions) (Fig. 8). From the potential energy, it is possible to determine the individual forces acting on each atom within the system. Then, by applying Newton's equations of motion to the *N*-atom system over small time-scales, a time-dependent evolution of the protein structure (also known as a trajectory) can be obtained.

Current force fields rely on empirical parameters; numerical constants which describe all of the potential interactions between all types of atoms present within the MD simulation. Standard sets of parameters have been developed for proteins and nucleic acids, and implemented in simulation packages such as CHARMM (Brooks 2009) or AMBER (Case 2005). However, additional parameters are needed to model novel or

modified residues. In the case of this work, additional parameters were needed to model the carboxylated lysine present within OXA-24.

$$U(\vec{R}) = \sum_{bonds} K_b(b - b_0)^2 + \sum_{angles} K_\theta(\theta - \theta_0)^2 + \sum_{Urey-Bradley} K_{UB}(S - S_0)^2 + \sum_{dihedrals} K_\varphi(1 + \cos(n\varphi - \delta)) + \sum_{impropers} K_\omega(\omega - \omega_0)^2 + \sum_{non-bonded\ pairs} \left\{ \varepsilon_{ij}^{min} \left[\left(\frac{R_{ij}^{min}}{r_{ij}} \right)^{12} - 2 \left(\frac{R_{ij}^{min}}{r_{ij}} \right)^{6} \right] + \frac{q_i q_j}{4\pi\varepsilon_0 \varepsilon r_{ij}} \right\} + \sum_{residues} U_{CMAP}(\varphi, \psi)$$

Fig. 8: CHARMM Force Field. This function determines potential energy of a conformation using the following molecular components: bonds, angles, Urey-Bradley, dihedrals, impropers, electrostatic interactions, and Van der Waals interactions. Figure adapted from Brooks et al. (2009).

In the case of the CHARMM force field the parameters fall into the following categories: force constants, equilibrium values, multiplicities (number of energy minima present during the rotation of dihedrals), and other factors such as atomic charges and Van der Waals parameters. The covalent bonds, bond angles, Urey-Bradley term – an additional harmonic term that helps reproduce crystal structure geometries and vibrational spectra more consistently by describing certain distances between the first and third atoms in an angle (MacKerell Jr 1998), though not all force fields use this term (Wang 2003) - and improper dihedrals, are all treated as "springs," i.e. represented by a

harmonic potential. The farther from their respective equilibrium values, the higher the overall energy a particular conformation will have. The non-bonded pairs portion of the equation represents the interactions between two charged particles, q_i and q_j, with a distance between them of r_{ij}. ε_0 is the permittivity of a vacuum, and ε is the classic dielectric constant of the medium separating the charged particles. The Lennard-Jones, or 12-6, potential is used to calculate Van der Waals forces between two atoms. ε_{ij}^{min} is the depth of the potential energy well between two particles, r_{ij}^{min} is the minimum distance where the two particles interact, and r_{ij} is the current distance between both atoms. CMAP is a torsional angle correction term, which helps with certain backbone inconsistencies for alanine, glycine, and proline that were observed previously in the CHARMM force field (MacKerell Jr 2004).

Modeling the protein's environment is also key to obtaining realistic trajectories. MD simulations typically use either an implicit or explicit solvent model. Implicit solvation approximates the effects of water on a simulation by modeling water as a dielectric continuum, instead of individual molecules. While these models are less computationally demanding, they fall short when modeling many important protein-water interactions (Tan 2006). Explicit solvent models include every water molecule present within the system. These models generally provide more detailed information about solvent effects on the protein, but this level of detail comes at the cost of computational speed. Explicit water models tend to differ from one another in the number of interaction points present on each water molecule. These can range from simple two-site models (Dyer 2009), to five-site models that not only model each atom, but represent the lone

electron pairs (Mahoney 2000). Typically, MD simulations use either a three-site model (such as TIP3P), or a four-site model.

2B. Computational Details

OXA-24 WT and the P227S mutant were constructed using the previously published OXA-24 WT crystal structure (PDB ID 3PAE). Mutating Pro227 to serine was accomplished using the MMTSB script library (Feig 2004). The CHARMM script library was used to add hydrogen atoms, and to create protein structure files (PSF). Protonation states were set to coincide with neutral pH. System charge was brought to 0 by selectively deprotonating Lys40 and Lys242. Both residues are incapable of directly interacting with the active site, and are exposed to the solvent; no effects of the deprotonation on the system are expected. Both structures were solvated with TIP3P (Jorgensen 1983) with the box dimensions of 90 Å x 70 Å x 65 Å.

OXA-24 G224D and the M223A were set up using a crystallographic OXA-24 G224D structure (Mitchell, unpublished data). These structures have two additional residues present on the N-terminus, an asparagine and phenylalanine. These two residues are located away from the active site and are not expected to affect the system. System charge was brought to 0 by selectively deprotonating Lys244 (identical to Lys242 in WT and P227S) for the G224D mutant; both Lys 42 (identical to Lys40 in WT and P227S) and Lys244 were deprotonated in the M223A mutant. All methods required to set up both the G224D and M223A mutant are otherwise identical to the methods employed to set up the WT and P227S mutant simulations. Box dimensions for both proteins are 90 Å × 67 Å × 62 Å.

The CHARMM22 force field (Brooks 2009) and CHARMM 35a1 simulation package were used to perform the MD simulations. Topology and parameter files were modified to include entries for the carboxylated lysine (Simakov and Wymore, unpublished data; Appendix A). All systems were minimized for 500 steps using the Steepest Descent algorithm, followed by Adopted Basis Newton-Raphson until the gradient threshold of 0.01 kcal/$Å^{-2}$ was archived. All systems were then heated from 10K to 300K over 30,000 steps (1 fsec/step). An NPT ensemble was then employed to stabilize the box conditions; done for 20,000 steps (1 fsec/step). Harmonic constraints were applied to the protein during these stages (minimization, heating, NPT): the SHAKE algorithm, which held bonds containing hydrogens near equilibrium values; and a 5 kcal/mol penalty to positional deviations on the protein's non-hydrogen atoms. The productive simulation (excluding energy minimization) was performed at the Pittsburgh Supercomputing Center using an NVT ensemble, SHAKE algorithm, Leapfrog algorithm for integration of the potential energy function, and a time-step of 2 fsec. The first 1 nsec of the NVT trajectories was treated as an equilibration period. Total NVT simulation time of all systems was 39 nsec. Rectangular periodic boundary conditions were employed; particle mesh Ewald was used for electrostatic calculations; and a non-bonded cutoff of 10 Å with a switching function was utilized throughout all stages of the simulation.

3. MD Trajectory Analysis

VMD (Humphrey 1996) was used to analyze the trajectories and render images. Frames were aligned by the protein Cα atoms using the RMSD Visualizer Tool plugin. Unless specified, frame 0 was used as the reference frame (first frame of the NVT portion of the simulation). RMSDs were calculated using the RMSD Visualizer Tool – reference

frame identical to trajectory alignment. RMSF, average structures, and R_{gyr} calculations were calculated with the Tk console using VMD's built-in functions for each. RMSF, average structures, and R_{gyr} procedures were performed using the last 22 nsec of the trajectories (see the appropriate sections in CHAPTER III).

The Python script which calculated the active site volume was written by Brian Mullen (Mullen and Szarecka, unpublished data). The code uses the Quickhull algorithm (Barber 1996), to create a convex hull with triangular facets which encloses the atoms of the specified binding pocket. Techniques for calculating volume of the resulting three-dimensional surface are extended from two-dimensional calculations. In two dimensions, the area of an arbitrary polygon can be calculated by taking the sum of the areas of a set of triangles, each with a base at one of the sides, and an apex at the center of the shape. In three dimensions, the same method can be used with tetrahedrons. The atomic selection used to define the active site can be found in Table 15 (Appendix C). The active site atoms were selected to best represent how OXA-24 accommodates substrates. Since entrance to the OXA-24 active site is essentially regulated by the Tyr112-Met223 hydrophobic bridge, atom selections were chosen to best represent this information.

Heatmaps generated from the volume script were created using the statistical software RStudio (http://www.rstudio.com/). These heatmaps were generated using Script 6 (Appendix B).

Hydrogen bonds (HB) were considered present in our simulation if the donor and acceptor heavy (oxygen, nitrogen) atoms are less than 3.2 Å from each other (Arunan 2011). When taking into account donor-hydrogen-acceptor angles, a conservative range

of 120-180° was employed. Since authors differ on what the correct geometric criteria of HB in proteins are (Arunan 2011; Torshin 2002), we decided to adopt the above ranges as representing the unequivocal and strong HB contributions. For example, other sources in the literature on the subject describe hydrogen bonding with liberal donor-acceptor distances of less than 3.9 Å, and donor-hydrogen-acceptor angles greater than 90.0° (Torshin 2002).

4. WT and P227S Structure Selection

Φ/Ψ-based selection of WT and P227S structures were performed to acquire unique conformations for molecular docking, and to detect differences between the conformational ensembles in both proteins. Every 2 psec of the last 22 nsec was loaded, and the φ and ψ angles for each β5-β6 loop residue was determined and plotted. These Ramachandran plots were subsequently overlaid to observe differences between WT and P227S. Regions on the Ramachandran plot which were occupied by only one of the enzymes were considered unique, and an individual point was chosen (by eye) to be used as a representative structure.

5. Molecular Docking

5A. Theoretical Background

Molecular docking is a computational technique for the prediction and modeling of protein-ligand interactions. Ideally, accurate binding affinities are predicted along with the correct poses of the ligand. Several algorithms have been implemented for docking, for example incremental construction algorithms – where small portions of the ligand are placed into the active site and scored for the best position, other fragments are then added

on and scored until the entire ligand is "built" into the active site (Rarey 1996); and genetic algorithms (GAs).

GAs are used by many docking programs – such as AutoDock4 (Morris 2009), and GOLD (Jones 1997) - to determine the optimal position of the ligand in relation to the receptor. GAs are conformational search algorithms that attempt to imitate the process of natural selection. The best solution to a problem (best binding position in a receptor) is therefore the solution with the best "fitness." In the case of molecular docking, the best fitness is given to the receptor-ligand conformation with the lowest energy. The Lamarckian GA present in AutoDock4 is a combination of both a GA, and a local search method. The "Lamarckian" aspect of this algorithm comes from Jean-Baptiste Lamarck, who believed that traits acquired through an individual's life will be passed on to their offspring. This is essentially a phenotypic change which brings about a genotypic change. This hybrid algorithm starts with the mapping of phenotype to genotype. All rotatable bonds and the *xyz* position of the ligand within the search box are "coded by" genes and chromosomes. For a user-specified number of individuals (i.e. population size), all of these values are randomized initially. The "fitness" (binding energy) is evaluated for all individuals and individuals are allowed to reproduce; the chromosomes and genes defining each individual's state may undergo crossing-over (depending on the user-defined rate of crossing-over). Mutation then occurs at a defined rate, which randomly alters genes. Just before the next generation begins, local searches are done at a user-defined rate. This local search - the Lamarckian aspect of the algorithm - allows for a further exploration of an individual's torsional space. The individuals that undergo a local search have their corresponding genes altered to reflect the local search.

The next generation begins, and the processes are repeated until either all generations have passed, or all energy evaluations have been performed regardless of the number of generations that have been passed. The search space of the algorithm is organized in a 3-dimensional box, or grid. This grid consists of a user-specified number of points along each of the *x*, *y*, and *z* directions. The energy of each atom type present in the ligand will be evaluated at each point using AutoDock4's free energy function, and the total ligand energy within the binding site is a combination of all of the atoms' energies.

5B. Computational Details

Docking to selected conformations was carried out using AutoDockTools4 and AutoDock4 (Morris 2009). The antibiotic structure of doripenem was downloaded and saved from PubChem (http://pubchem.ncbi.nlm.nih.gov/) in the 3D SDF format. Antibiotic 3D SDF files were converted to PDB files using the Online SMILES Translator and Structure File Generator (http://cactus.nci.nih.gov/services/translate/). The carboxylate group of doripenem was deprotonated using VMD to best represent the drug in physiological conditions. Hydrogen atoms were added to antibiotic structures using AutoDockTools4, and edited using VMD. Only polar receptor hydrogens were utilized during docking runs, and Kollman partial charges (Singh 1984) were added to receptor atoms. Search parameters regarding the GA were identical for all docking simulations:

- Grid Spacing = 0.225
- # of GA Runs = 100
- Population Size = 750
- Maximum # of Energy Evaluations = 1.0×10^8

- Maximum # of Generations = $5.0x10^4$
- Maximum # of Individuals that Automatically Survive = 1
- Rate of Gene Mutations = 0.02
- Rate of Crossover = 0.8
- GA Crossover mode = "twopt"
- Mean of Cauchy distribution for gene mutation = 0.0
- Variance of Cauchy distribution for gene mutation = 1.0
- # of generations for picking worst individual = 10

All other docking/local search parameters were set as defaults. Grid box size was dependent upon the receptor, as active site elements may have undergone rearrangements during the MD simulation. For each unique conformation, grid boxes were centered upon the following atoms, and had the following grid sizes (# of x, y, and z points):

- 3PAE_Target.pdb: Centered on Arg261's Cζ with grid size of 120x100x110. Structure used for docking validation. This is a WT OXA-24 structure which does not contain the KCX, instead an aspartate is present. Structure was modified directly from PDB 3PAE, where only one protein chain was used as the receptor for the docking of acylated doripenem.
- oxa24wtsys1.pdb: Centered on Arg261's Cζ with grid size of 120x100x110. Structure used for docking validation. This is a WT OXA-24 structure which does contain the KCX. This structure was taken from the MD setup just prior to energy minimization. Only the protein chain was used as the receptor for the docking of acylated and un-bound doripenem,

- wt_trp190.pdb: Grid box for doripenem was centered on Ser81's Oγ with grid size of 120 x 110 x 110. This is the WT structure utilized from the Trp221 φ/ψ structure selection.
- wt_pro196.pdb: Grid box for doripenem was centered on Ser81's Oγ with grid size of 110 x 100 x 110. This is the WT structure utilized from the Pro/Ser227 φ/ψ structure selection.
- ps_trp190.pdb: Grid box for doripenem was centered on Ser81's Oγ with grid size of 110 x 100 x 100. This is the P227S structure utilized from the Trp221 φ/ψ structure selection.
- ps_ser196.pdb: Grid box for doripenem was centered on Ser81's Oγ with grid size of 110 x 100 x 100. This is the P227S structure utilized from the Pro/Ser227 φ/ψ structure selection.

All docking simulations were performed using the Lamarckian GA on the Phoenix Computing Cluster at Grand Valley State University (supported by NSF Grant No. CNS-1228291). Docking results were analyzed in VMD.

CHAPTER III

RESULTS

1. Determination of OXA-24 Subfamily

The sequences retrieved from the non-redundant protein database through NCBI can be found on the following page in Table 1. Approximately 11 enzymes (as designated by Parental Enzyme) were determined to be part of the OXA-24 subgroup. Other parental CPase and non-CPase sequences were saved for comparison. The MSA that resulted from M-Coffee can be found in the Supplementary Data (Fig. 37, Appendix C). While the primary goal of the MSA was to determine if any unique motifs were present in only the OXA-24 subgroup, the members of the OXA-24 subgroup were also determined, as previous attempts to organize the class D family were incomplete (Poirel 2010). The motifs that are truly unique to only the OXA-24 subgroup are small in number. Some motifs appear in the OXA-24 family, and one other CPase subgroup. One example is a Gln50-Thr-Gln motif which appears in every member of the OXA-24 subgroup, but also in OXA-228. On the whole the MSA did not provide any additional motifs for analysis within the MD simulations. However, one unique feature of the β5-β6 loop in CPase OXAs is the presence of a hydrophobic residue (typically a valine, or isoleucine for OXAs-23 and 48) at position 225 (OXA-24 numbering). No non-CPase OXA in the table below contained a hydrophobic residue in the homologous position. This does not mean that this pattern is universal, but the trend is present amongst the enzymes collected.

Enzyme	NCBI Accession #	Parental Enzyme	CPase
OXA-1	AAA91586.2	OXA-1	No
OXA-2	YP_006953608.1	OXA-2	No
OXA-5	CAA41211.1	OXA-5	No
OXA-10	YP_008658337.1	OXA-10	No
OXA-20	AAC23554.1	OXA-20	No
OXA-23	ABK34775.1	OXA-23	Yes
OXA-24	YP_002967455.1	OXA-24	Yes
OXA-25	AAG35607.1	OXA-24	Yes
OXA-26	AAG35608.1	OXA-24	Yes
OXA-48	AAP70012.1	OXA-48	Yes
OXA-51	CAC83905.2	OXA-51	Yes
OXA-58	AAW57529.1	OXA-58	Yes
OXA-63	AAU88145.1	OXA-63	No
OXA-72	YP_008090878.1	OXA-24	Yes
OXA-139	CAQ51348.1	OXA-24	Yes
OXA-143	ACX70402.1	OXA-24	Yes
OXA-160	ADB28891.1	OXA-24	Yes
OXA-182	ADK92148.1	OXA-24	Yes
OXA-207	AFK28473.1	OXA-24	Yes
OXA-228	AFM55001.1	OXA-228	Yes
OXA-231	AFG29918.1	OXA-24	Yes
OXA-253	AGK07368.1	OXA-24	Yes
OXA-255	AGK07369.1	OXA-24	Yes

Table 1: Class D Representative Sequences. Non-CPase enzymes were collected to determine if discovered motifs were conserved amongst only CPases, or only OXA-24-related CPases. Members of the OXA-24 subgroup are shown as having OXA-24 as the parental enzyme.

2. Comparison of Mutant Dynamics

2A. Trajectory RMSDs

2A-1. All Protein RMSD

Stability of the simulations was evaluated using all-Cα RMSD of each enzyme (Fig. 9). RMSD calculations were performed using the initial frame of the NVT simulation as the reference. Trajectories were aligned by all Cα atoms.

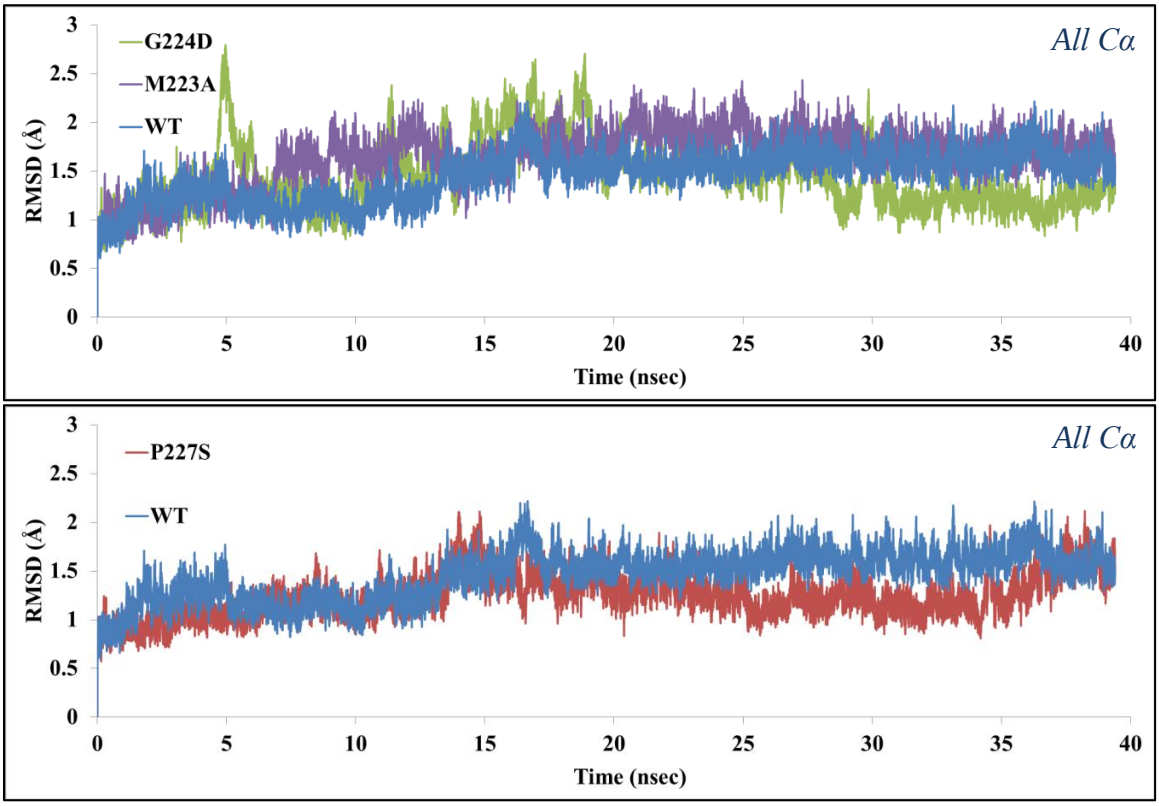

Fig. 9: All-Cα RMSD of Entire Protein.

All simulations showed the characteristic increase and leveling of all-Cα RMSD values. Because RMSD is a commonly accepted measure of structural drift throughout the simulation, WT, M223A, and P227S trajectories were considered stable as large deviations were not observed past the extended 18 nsec equilibration period.

Interestingly, the P227S mutant shows lower RMSD values than the WT for the majority of the productive trajectory (i.e. from 18 nsec onward), while the M223A mutant shows the opposite behavior. The behavior of the G224D mutant has been unique in that RMSD values vary more dramatically (for example, around the 5 and 17 nsec time points). This makes us uncertain about the successful stabilization of the G224D system. The G224D peaks are caused by large fluctuations of the N-terminus; N-terminal Cαs in the high RMSD frames deviate by ~23 Å from the reference frame (Fig. 38, Appendix C), but the N-terminal residues (His32, Ile33, Ser34) do not form interactions with other residues. While the G224D mutant may not have yet stabilized, in the following sections we use the last 22 nsec as productive trajectory. It should also be mentioned that the enzymes' P loops may not have been sufficiently sampled due to the fact that large loop movements of proteins tend to occur on the μsec timescale (Dror 2012).

2A-2. RMSD of Loops

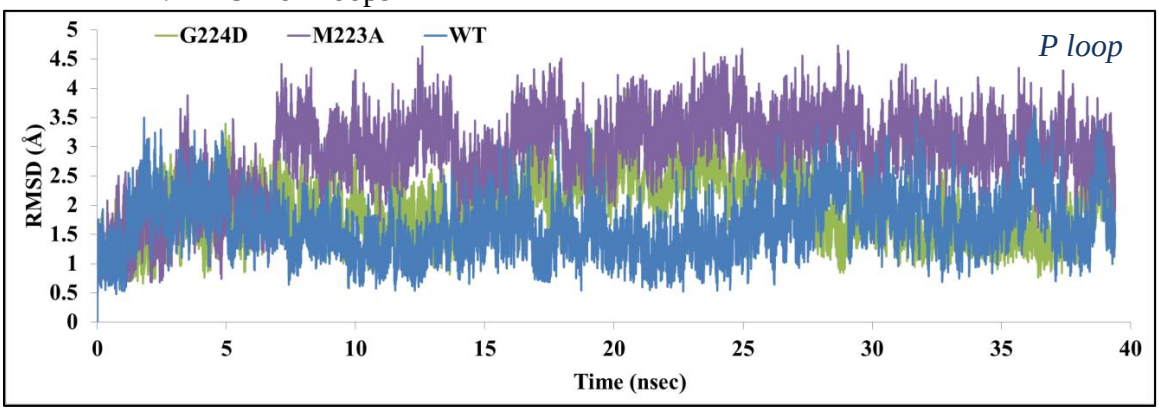

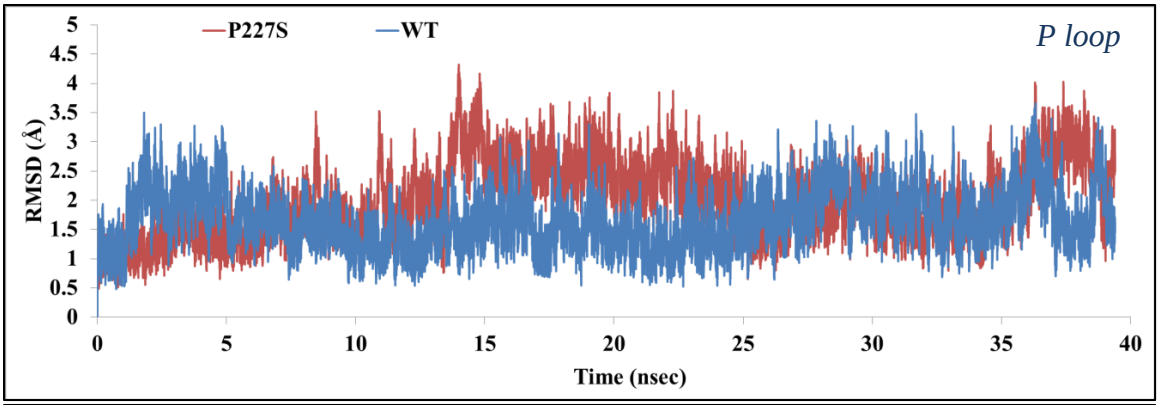
P loop
P227S
WT
RMSD (Å)
Time (nsec)

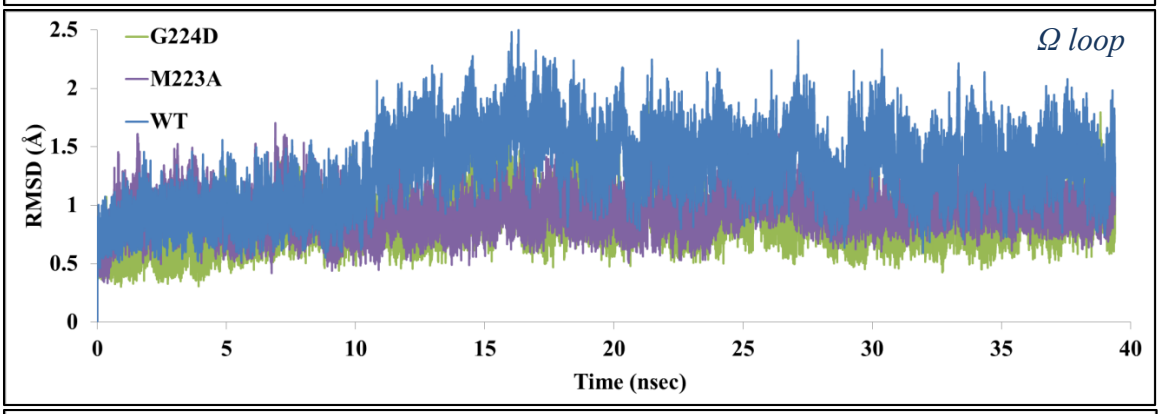
Ω loop
G224D
M223A
WT
RMSD (Å)
Time (nsec)

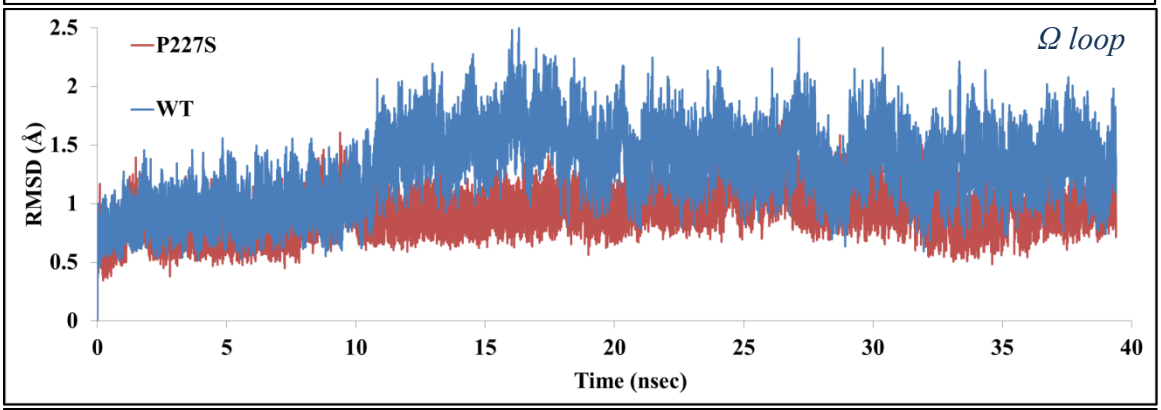
Ω loop
P227S
WT
RMSD (Å)
Time (nsec)

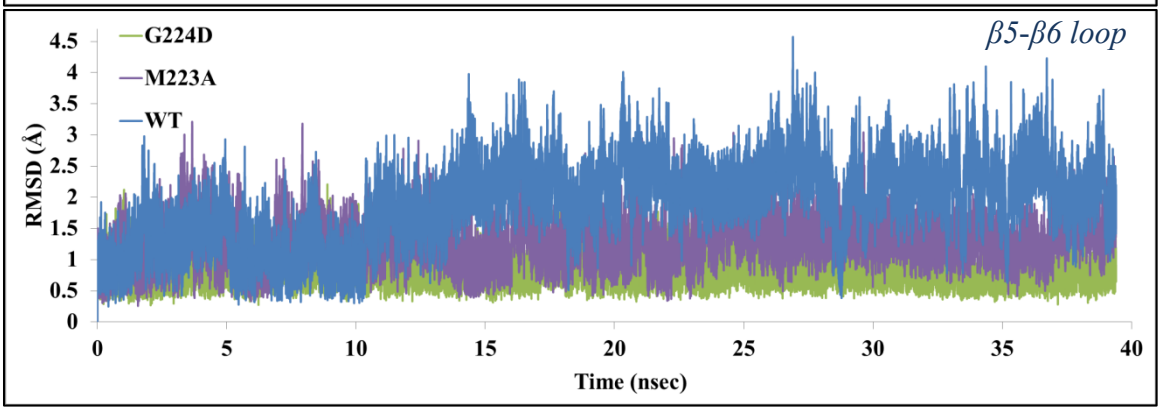
β5-β6 loop
G224D
M223A
WT
RMSD (Å)
Time (nsec)

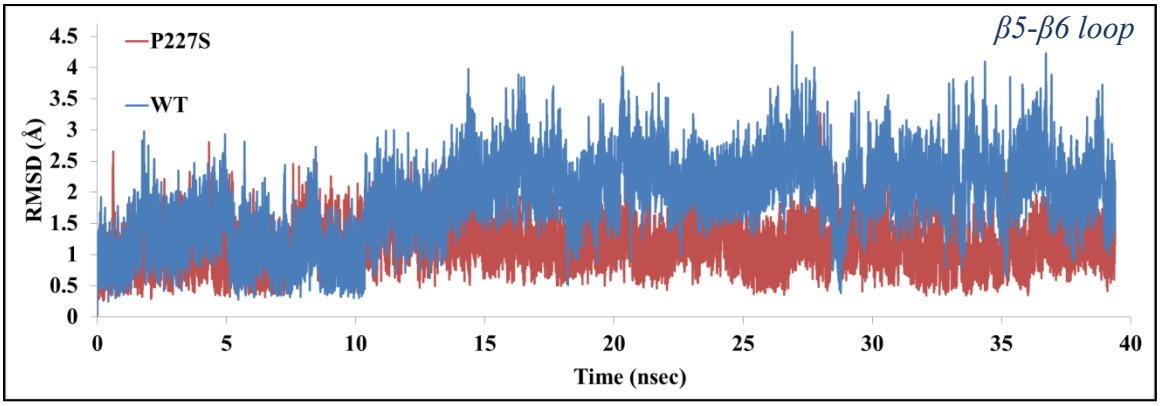

Fig. 10: Cα RMSD of Protein Loops. Residue spans are: P loop, residues 93-120; Ω loop, residues 154-176; β5-β6 loop, residues 221-228.

The RMSD drift calculations are present in Table 2.

	Whole Protein: Cα Atoms (Å)	**P Loop: Cα Atoms (Å)**	**Ω Loop: Cα Atoms (Å)**	**β5-β6 Loop: Cα Atoms (Å)**
WT	1.6 ±0.1	1.7 ±0.5	1.4 ±0.2	2.2 ±0.5
M223A	1.8 ±0.2	3.1 ±0.5	1.0 ±0.1	1.4 ±0.3
G224D	1.4 ±0.3	2.0 ±0.5	0.9 ±0.2	0.8 ±0.2
P227S	1.3 ±0.2	2.1 ±0.6	1.0 ±0.2	1.2 ±0.3

Table 2: RMSD Drift. RMSD drifts are calculated using the last 22nsec of the trajectory. RMSD drift is calculated as the average RMSD.

Loop regions were expected to contribute greatly to the overall RMSD drift. In the case of OXA-24, we were interested in the P loop, Ω loop, and the β5-β6 loop, with the P loop being particularly difficult to stabilize over a relatively short trajectory span. As shown in Table 2, we observe rather low values of RMSD for the β5-β6, and Ω loops, but the P loop experiences much higher drift overall, particularly for M223A. In all mutants both β5-β6 and Ω loops have lower RMSD values than WT overall.

2A-3. RMSD of Active Site

The modality of the active site residues was measured as the RMSD of PASTFK, KSG, SxV, and Arg261 motifs using both the RMSD of only Cα atoms, and all atoms to reveal deviations from the initial structure (Fig. 11).

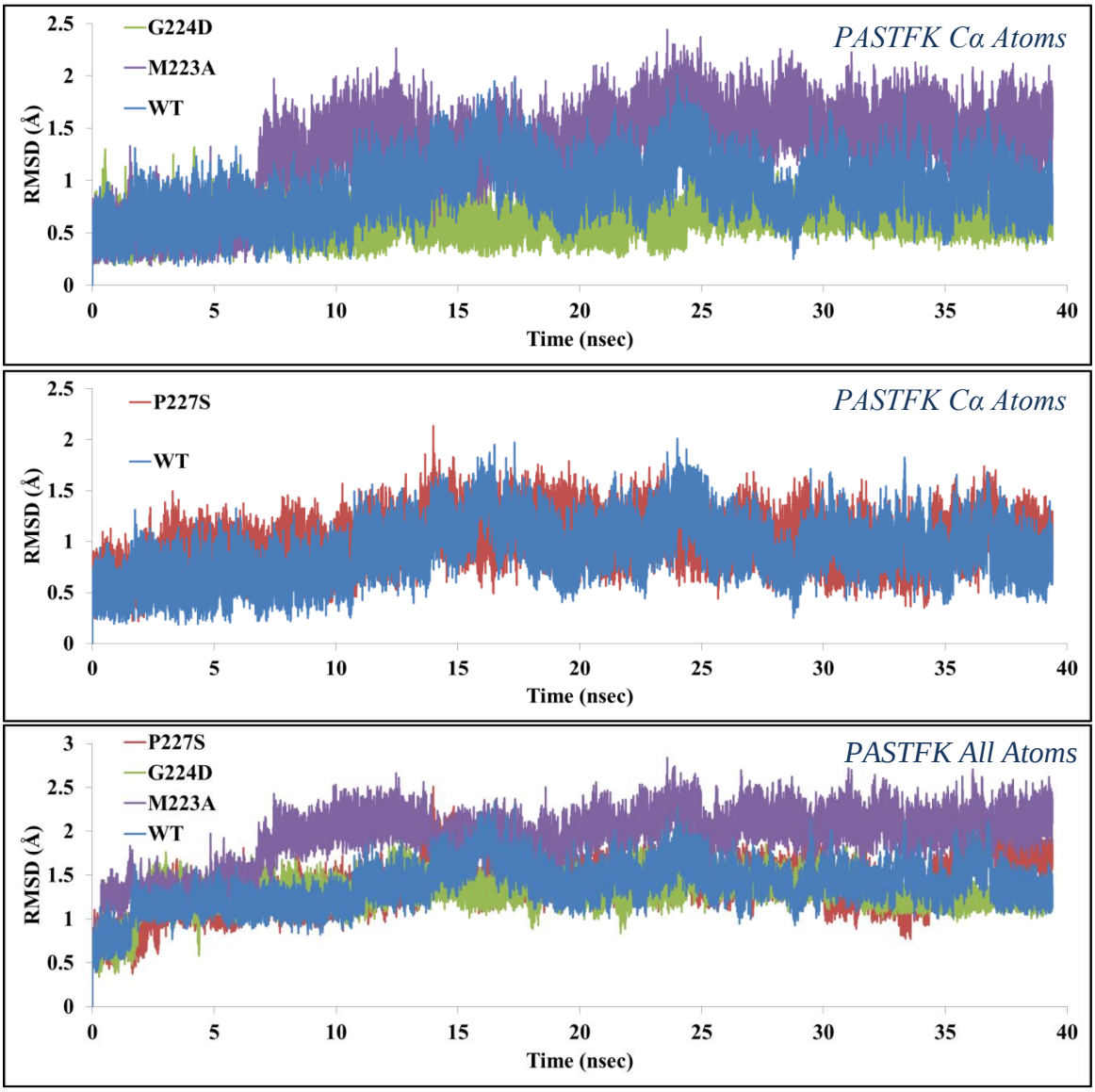

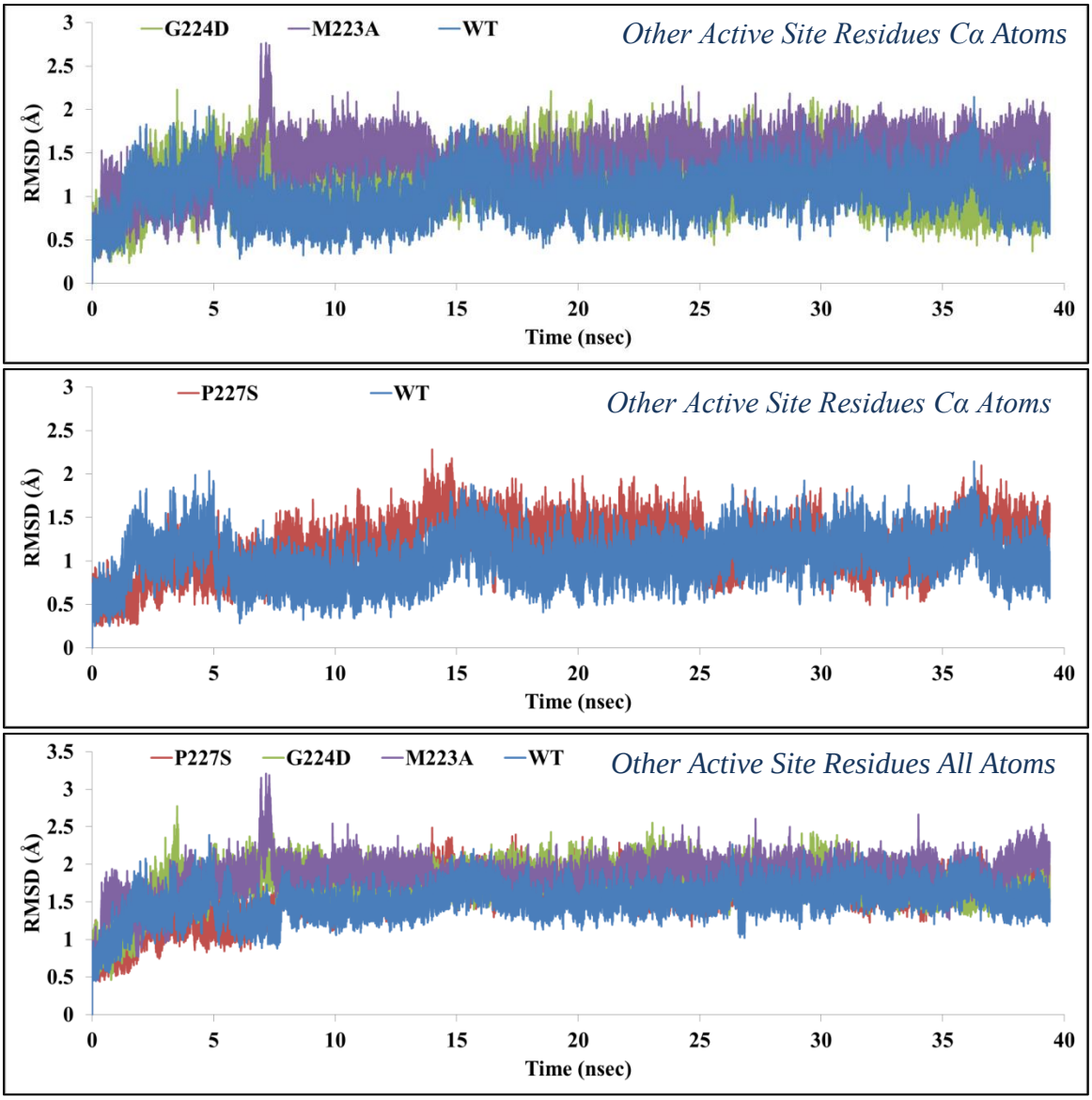

Fig. 11: RMSD of Active Site. Other active site residues are: Ser128 and Val130 (SxV motif), Lys218, Ser219, and Gly220 (KSG motif), as well as Arg261. PASTFK motif starts with Pro79.

The RMSD drift for the RMSDs in Fig. 11 are present in Table 3.

	PASTFK Motif: Cα Atoms (Å)	PASTFK Motif: All Atoms (Å)	Other Active Site Residues: Cα Atoms (Å)	Other Active Site Residues: All Atoms (Å)
WT	1.0 ±0.2	1.4 ±0.2	1.1 ±0.2	1.6 ±0.1
M223A	1.5 ±0.2	2.1 ±0.2	1.5 ±0.2	1.9 ±0.1
G224D	0.7 ±0.1	1.3 ±0.1	1.2 ±0.3	1.8 ±0.2
P227S	1.0 ±0.2	1.5 ±0.2	1.2 ±0.2	1.7 ±0.1

Table 3: RMSD Drift of Active Site. RMSD drifts are calculated using the last 22nsec of the trajectory. RMSD drift is calculated as the average RMSD. Other active site residues are: Ser128, Val130, Lys218, Ser219, Gly220, and Arg261. PASTFK motif starts with Pro79.

The PASTFK motif shows changes in RMSD in all mutants, but only large deviations in the M223A mutant when all atoms are examined. A similar pattern is present in the other active site residues, but not to the same extent. The M223A RMSD peak in Fig. 11 *Other Active Site Residues Cα/All Atoms* (around 7 nsec) corresponds to a conformational shift in the protein backbone where Ser128 and Val130 are located. Both of the residues' Cαs shift ~4 Å from the reference frame (Fig. 39, Appendix C). Overall, M223A and G224D (to a lesser extent) mutants are most affected.

2B. Internal Flexibility of Mutants

The effects of β5-β6 loop mutations on the global dynamics of the protein can also be studied through the relative average flexibilities of different regions of the protein calculated over the entire trajectory – the Root Mean Square Fluctuation (RMSF). Differences in RMSF were calculated for all mutants with respect to the WT (Fig. 12-13, Table 4).

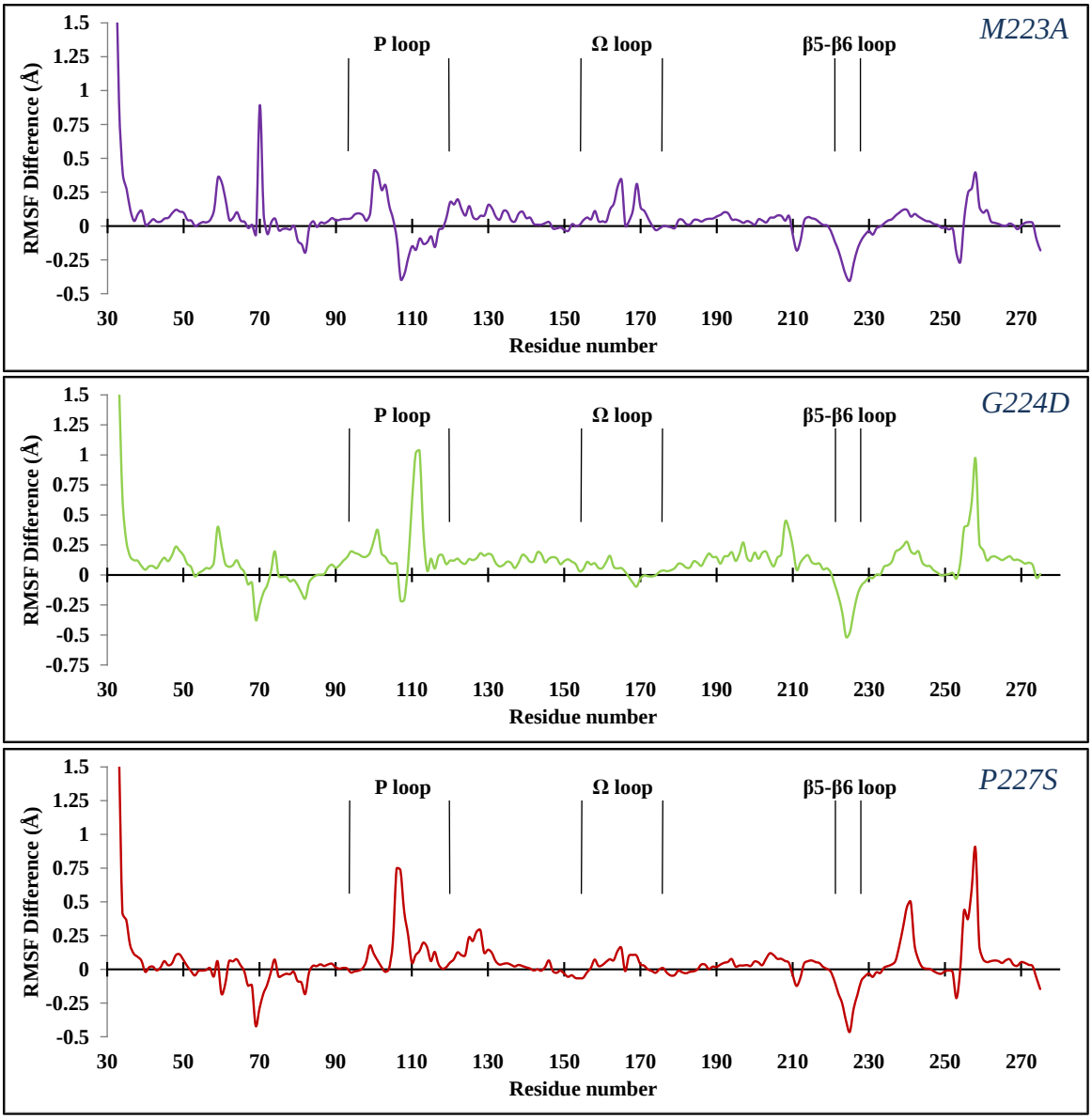

Fig. 12: ΔRMSF between Mutants & WT. *M223A*: ΔRMSF between M223A and WT. *G224D*: ΔRMSF between G224D and WT. *P227S*: ΔRMSF between P227S and WT. ΔRMSF was calculated by subtracting the Cα RMSF values of the WT from the Cα RMSF values of the specified mutant. Values above the zero line indicate increased fluctuations in the mutant over the WT, while values below the line indicate decreased fluctuations.

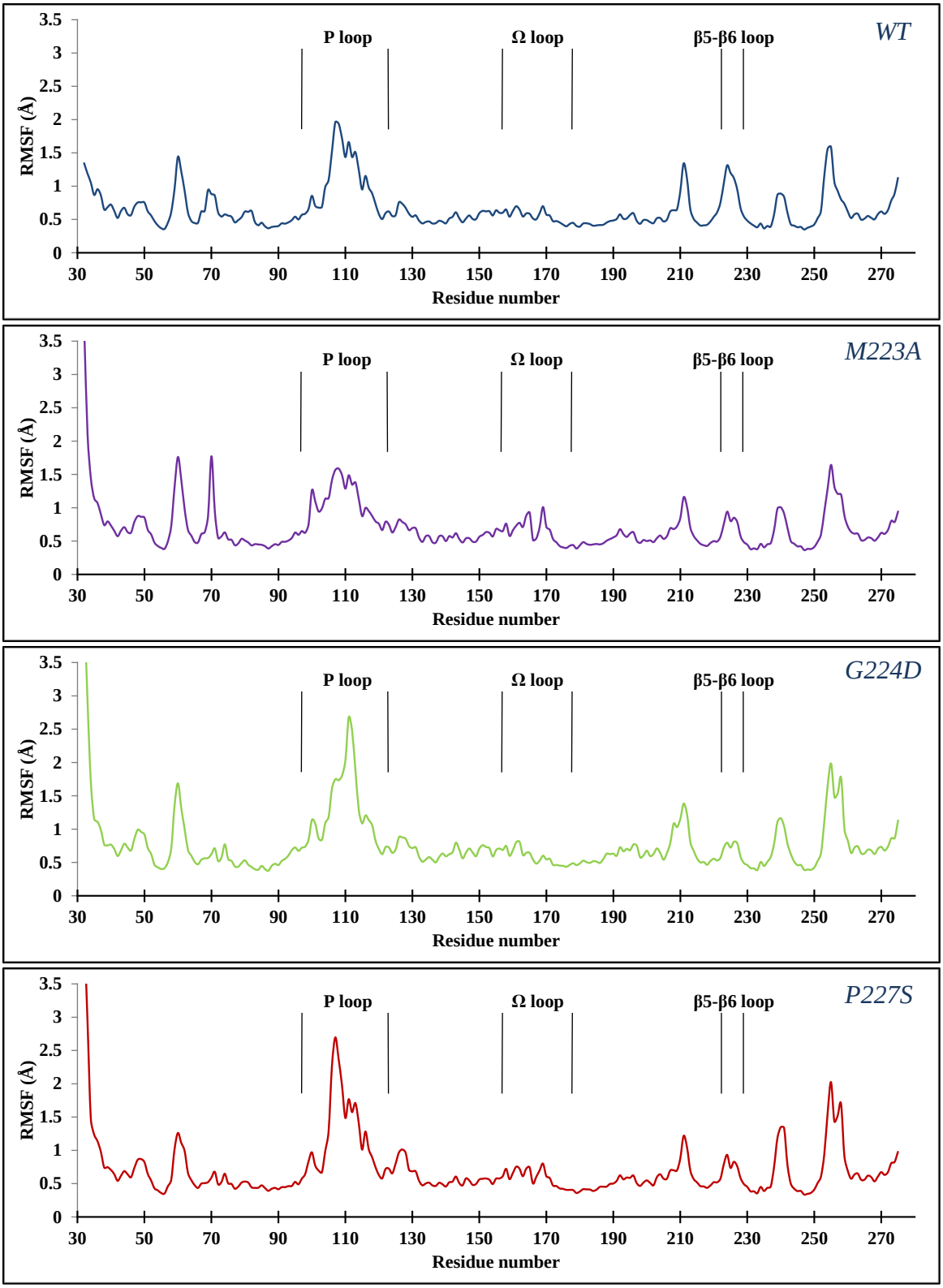

Fig. 13: RMSF of WT & Mutants.

Mutant	Residues with Decreased Fluctuations Relative to WT	Residues with Increased Fluctuations Relative to WT
M223A	80, 81, 82, 106-111, 113, 114, 116, 211, 212, 221-228, 253, 254, 274, 275	32-36, 39, 48, 49, 58-61, 64, 70, 100, 101, 102, 103, 104, 120, 121-123, 125, 130, 131, 134, 135, 139, 158, 162-165, 168-171, 192, 239, 240, 256-259, 261
G224D	69-71, 81, 82, 107, 108, 169, 222-227	32-38, 44-50, 58-60, 64, 74, 92, 93-104, 110-113, 115, 117, 118, 120, 121-123, 125-131, 135, 136, 138-148, 150-152, 156, 161, 162, 184, 185, 187-190, 192-204, 206-210, 212-215, 236-244, 254-270, 272
P227S	60, 61, 67-72, 82, 211, 222-227, 253, 275	32-37, 48, 49, 99, 100, 105-109, 111-114, 116, 122-131, 164, 165, 168, 169, 204, 205, 238-242, 255-259

Table 4: Residues with Decreased/Increased Fluctuations Relative to WT. A decrease means a ΔRMSF < -0.1Å, and an increase mean a ΔRMSF > 0.1Å. Residue numbers are colored according to the structural motif on which they are located, blue is β5-β6 loop, green is P loop, red is Ω loop, and orange is catalytic PASTFK motif.

As seen from the ΔRMSF calculations, all three β5-β6 loop mutations decrease the overall fluctuations of the loop. At least some part of the catalytic PASTFK motif also decreases in flexibility across the mutants – typically Thr82. Some residues in the Ω loop see consistent increases in total fluctuations relative to the WT as well (generally the residues around Gln162); particularly so in the M223A mutant. Curiously, all of the mutants' N-termini (residues 32-40, part of helix 1) fluctuate greatly over the WT enzyme.

Differences between the enzymes are primarily in the P loop. The area of the P loop around Thr111 fluctuates highly in the G224D trajectory. Of interest is the adjacent

residue Tyr112, which forms a hydrophobic bridge with Met223. This bridge has been implicated in ligand binding and selectivity (Schneider 2011). The RMSF for Tyr112's Cα in the WT and G224D trajectories are 1.44 Å, and 2.47 Å respectively. The P227S mutant as well shows increases in P loop flexibility over the WT. RMSF of Tyr112 also increases, but Asp106 in particular shows large a large increase in fluctuations. The M223A mutant shows a different behavior with the first (N-terminal) portion of the loop experiencing increased fluctuations, while the latter half shows decreased fluctuations.

Leu70 in M223A shows an extraordinary increase in RMSF over the WT. Leu70 is exposed to solvent, on the α2 helix, and is approximately 22 Å from the site of the M223A mutation.

Another residue of interest is Val169 in the G224D mutant, which is the only Ω loop residue to have decreased fluctuations relative to the WT; the other mutants have some Ω loop residues with increased fluctuations, but none with decreases.

2C. Average Conformations

In order to evaluate how the above changes impact the structure of each enzyme, we have calculated trajectory average structures. Average structures are limited in that side chain atoms' positions invariably become unphysical. However, they are appropriate for comparing backbone conformational changes between mutants. Average structures for each protein were determined using Script 5 (Appendix B). Average structures were aligned by all Cα atoms to allow for comparison. The comparison between the WT and mutant average structures is below (Fig. 14); the Cα RMSD between the mutant structures and WT are given in Table 5.

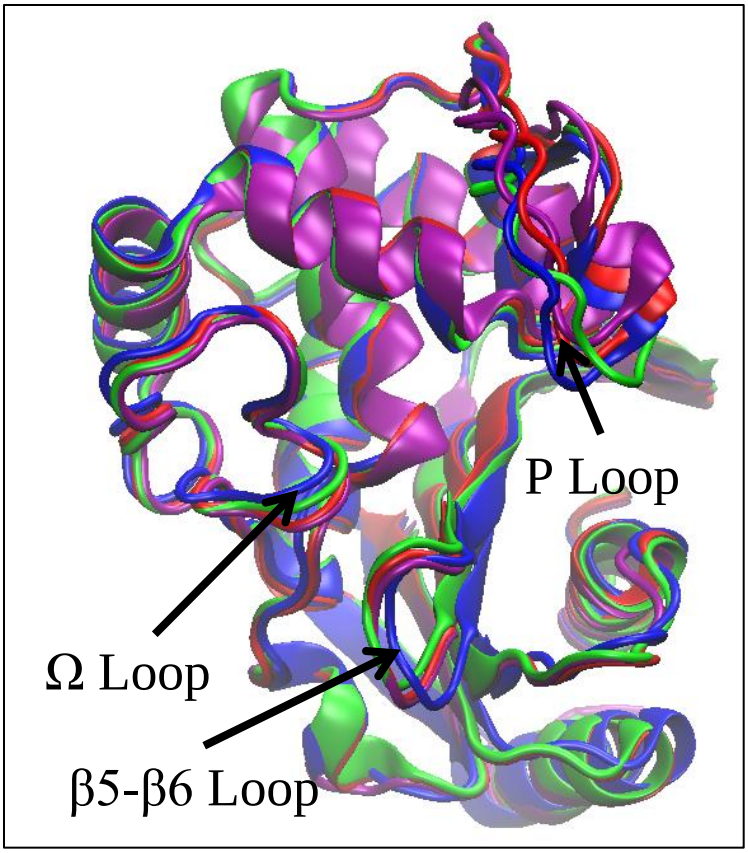

Fig. 14: Average Structures. WT average structure colored blue, M223A average structure colored purple, G224D colored green, and P227S colored red. Proteins were aligned by all Cαs.

	M223A	**G224D**	**P227S**
RMSD (Å)	1.37	1.15	1.18

Table 5: Cα RMSD between WT & Mutant Average Structures.

Common amongst the mutants' average structures is the shift of the P loop away from the β5-β6 loop. The Ω loop for all mutants has also shifted "downward" and closer to the β5-β6 loop; the M223A mutant has shifted the closest with G224D showing the least change relative to the WT. Also across all the mutants, the β5-β6 loops have all shifted towards the Ω loop, and the Ω loops have all shifted toward the β5-β6 loops as well. These trends are also illustrated by average distances between atoms in both of the loops (Table 6).

	WT Avg. (Å)	M223A Avg. (Å)	G224D Avg. (Å)	P227S Avg. (Å)
Leu168Cα - Gly222Cα	7.94 ±1.07	6.45 ±0.44	6.59 ±0.38	6.71 ±0.37
Leu168Cα - Gly/Asp224Cα	7.85 ±0.97	6.78 ±0.70	7.05 ±0.47	6.68 ±0.78
Leu168Cα - Met/Ala223Cα	9.36 ±1.09	8.18 ±0.52	8.25 ±0.36	8.13 ±0.47
Val163Cα - Gly/Asp224Cα	7.87 ±1.39	6.43 ±0.88	6.42 ±0.39	6.24 ±0.58
Val163Cα - Val225Cα	8.92 ±1.44	6.61 ±0.83	6.45 ±0.48	6.34 ±0.50

Table 6: Atomic Distances between Ω & β5-β6 Loop. Distances selected from Table 16, Appendix C.

There are few other differences between the mutants' average structures when being compared to the WT. One of the few is the shift of the α3 helix (containing the catalytic PASTFK) towards the ligand-binding space in the M223A and P227S mutants, but not G224D (Fig. 15, Table 7).

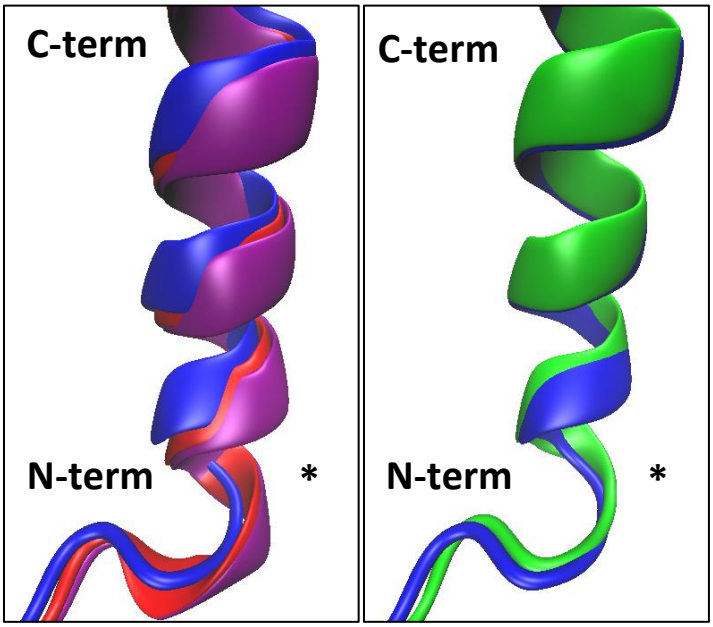

Fig. 15: Average Structures α3 Helix Shift. *Left*: WT colored blue, M223A colored purple, P227S colored red. *Right*: WT colored blue, G224D colored green. *Ligand binding space is located to the right of the helices in both images.

	WT Avg. (Å)	M223A Avg. (Å)	G224D Avg. (Å)	P227S Avg. (Å)
Ala80Cα - Gly222Cα	6.12 ±0.73	5.17 ±0.27	5.40 ±0.31	5.29 ±0.32
Ala80Cα - Trp221Cα	7.46 ±0.89	6.24 ±0.30	6.57 ±0.40	6.15 ±0.28
KCX84Cα – Ser219Cα	10.50 ±0.43	9.98 ±0.25	10.72 ±0.43	9.82 ±0.32
Ser81CA - Gly220Cα	4.87 ±0.25	4.70 ±0.24	4.83 ±0.20	4.61 ±0.25
Thr82Cα - Lys218Cα	6.65 ±0.44	6.02 ±0.20	6.66 ±0.35	5.89 ±0.24

Table 7: Atomic Distances between PASTFK & β5. Distances selected from Table 16, Appendix C.

The other difference is found when examining the average structures of the WT and M223A enzymes, Leu70's Cα is shifted ~2 Å from the WT's position. Leu70 saw a large increase in fluctuations over the WT - as detailed in the previous section (Flexibility of Mutants).

2D. Radius of Gyration

To determine the effect of the mutations on the compactness of the enzymes, we calculated the R_{gyr} for all of the proteins' heavy atoms (Fig. 16, Table 8).

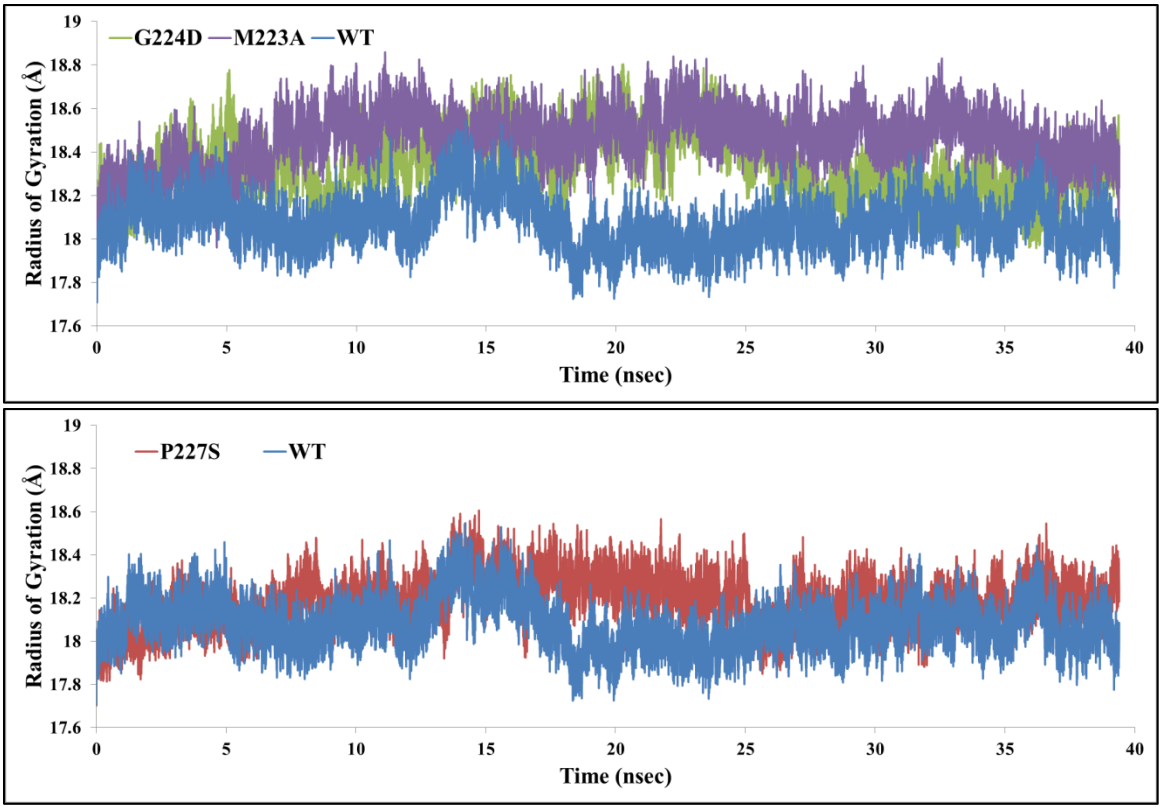

Fig. 16: Radius of Gyration. R_{gyr} values for all trajectories were determined using Script 4 (see Appendix B). *Top*: R_{gyr} comparing M223A and G224D to WT. *Bottom*: R_{gyr} comparing P227S to WT.

Trajectory:	**WT Avg.**	**M223A Avg.**	**G224D Avg.**	**P227S Avg.**
R_{gyr} (Å):	18.0 ±0.1	18.5 ±0.1	18.3 ±0.1	18.2 ±0.1

Table 8: Average R_{gyr} Values. Average R_{gyr} values calculated using the last 22 nsec of the trajectories.

All β5-β6 loop mutations appear to decrease the overall compactness of the mutants, although the difference between the WT and P227S is not dramatic. Both M223A and G224D are significantly less compact than WT throughout the majority of their respective trajectories. M223A maintains higher R_{gyr} values from 5 nsec onward, and G224D follows the same pattern until 30nsec when it begins to resemble the WT. The P227S mutant is the most similar to the WT when examining the R_{gyr}. Only for ~18% of the trajectory – from 18 nsec to about 25 nsec – does the mutant consistently

have greater R_{gyr} values than the WT. For the rest of the trajectory, they both share relatively similar values, and thus a similar level of compactness. The G224D mutant shows a similar trend, while also fluctuating to a less compact conformation from 5 to 12 nsec.

2E. Volume of Active Site

Because the size of the antibiotic and the corresponding size of the enzymatic active site are essential in the substrate selectivity of class D enzymes, we sought to determine how the volume of the active site was changing throughout the trajectories. A volume-calculation script was written in Python by Brian Mullen (Mullen and Szarecka, unpublished data). Each active site was defined using specific atoms selected from each enzyme, as the M223A and G224D mutations introduce new atoms to the definition of protein surface that is used to calculate volume. The binding pocket was divided into two parts: upper and lower. The upper part of the pocket includes the P loop residues; designed to reflect its contributions to active site volume (Fig. 17A-C). The lower part of the pocket contains the other important elements (catalytic residues, Ω loop, β5-β6 loop), and is designed to model their effects on the shape and size of the active site (Fig. 17D) where the bulky functional groups of 3rd generation cephalosporins would have to fit (refer to Fig. 5). The pocket was defined this way since an unpublished crystal structure of OXA-24 in a complex with a 3rd generation cephalosporin showed that the antibiotic's occupancy of the active site was mostly limited by the space bordered by the β5 stand, and the Ω loop (Mitchell 2015).

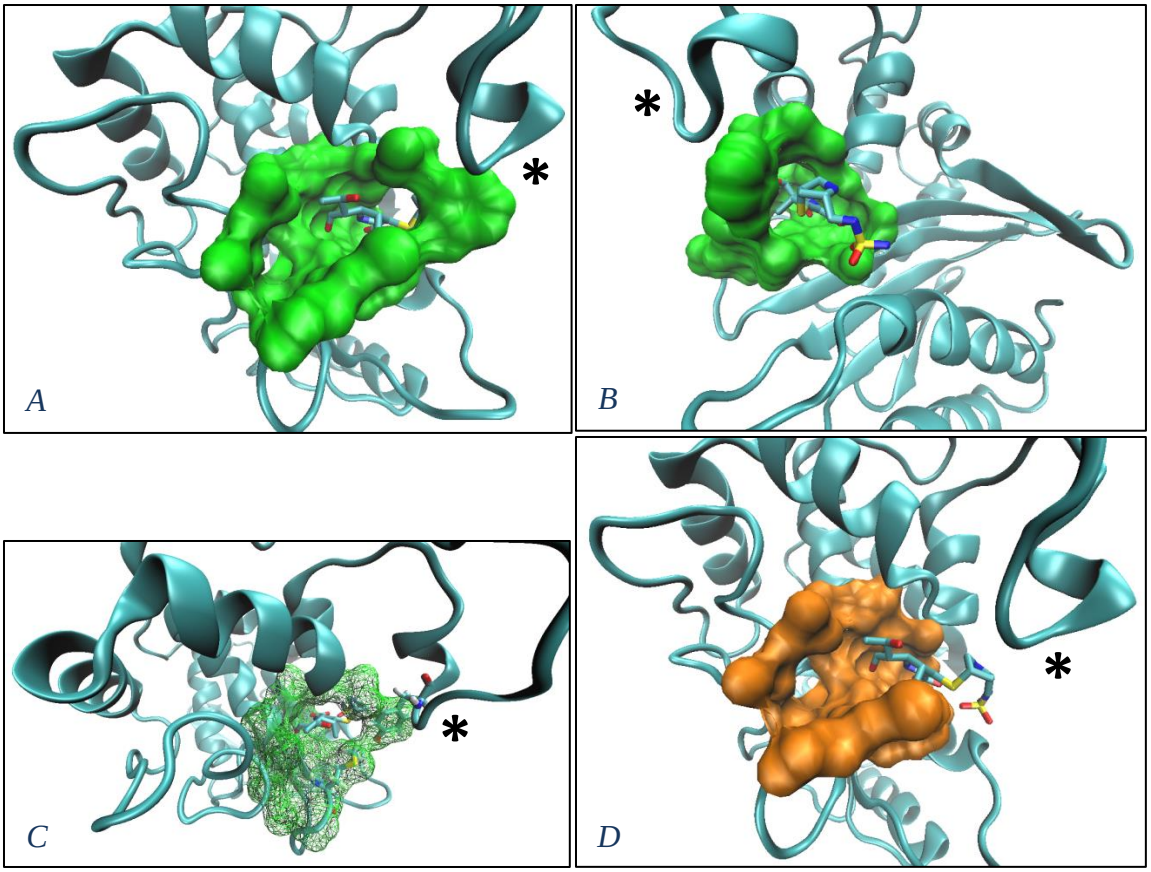

Fig. 17: Atomic Selection of Active Site. *A*: Orientation 1 of the P loop-inclusive active site selection. *B*: Orientation 2 of the P loop-inclusive active site selection. *C*: Orientation of P loop-inclusive selection showing the Tyr112-Met223 bridge. *D*: Figure of the "lower" active site, without P loop atoms. *P loop.

By creating two different selections for the active site, it is possible to see which part of the active site is contributing most to volume changes. Fig. 18 depicts how the "whole" (P loop-inclusive) active site volume changed over the trajectories for each enzyme.

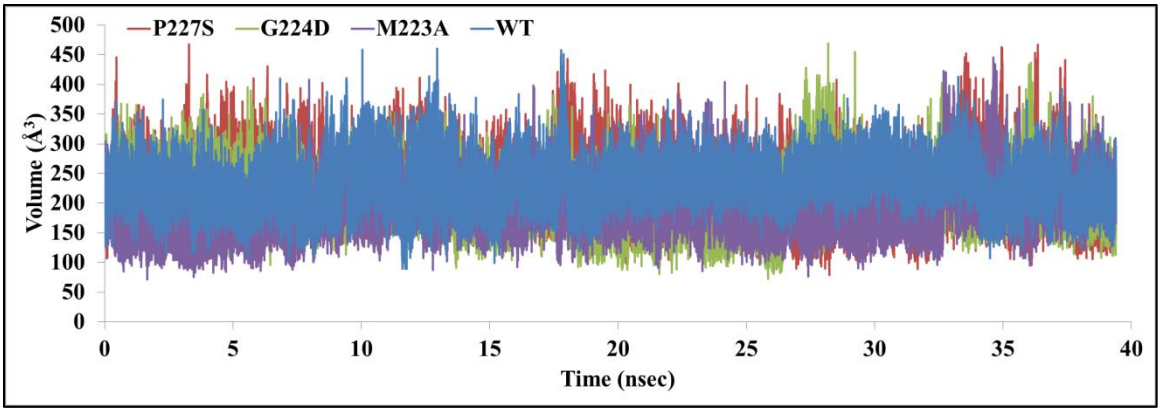

Fig. 18: Whole Active Site Volume.

Fig. 19 shows the active site volume when P loop residues are removed from the calculation. Table 9 shows the average volume and standard deviations of the two active site selections.

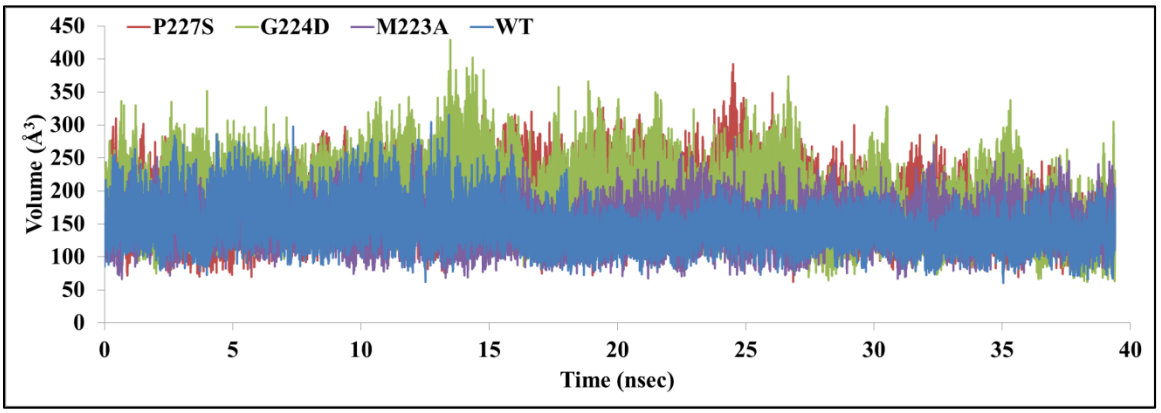

Fig. 19: Lower Active Site Volume.

	Whole Active Site Volume Avg. (Å^3)	**Lower Active Site Volume Avg. (Å^3)**
WT	236 ±34	135 ±19
M223A	199 ±43	147 ±24
G224D	196 ±42	176 ±42
P227S	219 ±51	173 ±37

Table 9: Average Active Site Volumes. Averages were calculated using the last 22 nsec of the trajectory.

The WT, which has the largest average whole active site volume, interestingly has the smallest average lower active site volume. The mutants do fluctuate to higher volumes, sometimes higher than the WT, but they all also fluctuate to lower volumes (Fig. 18). The lower active site shows the tendency of the mutants to remain at a higher volume, until the end of the trajectory where all of the enzymes to converge to similar values (Fig. 19).

We have calculated the mean distances between each atom in the user-defined active site, and the variances of those mean distances. Using these matrices it is possible to determine which atoms are contributing to the fluctuations of the each active site's volume. Fig. 20 shows both the mean distances and distance variances of the whole active site for the M223A mutant. Fig. 21 shows both the mean distances and distance variances of the whole active site for the G224D mutant. Fig. 22 and 23 show the same data for the P227S and WT enzymes respectively. Additionally, due to the fact that the defined active sites between the P227S mutant and WT are identical in both total number of atoms and atom numbering it was possible to create matrices representing the differences between the two enzymes in terms of mean distances, and the variances. Fig. 24 shows both the differences between mean distances and distance variances of the whole active site for the P227S and WT enzyme.

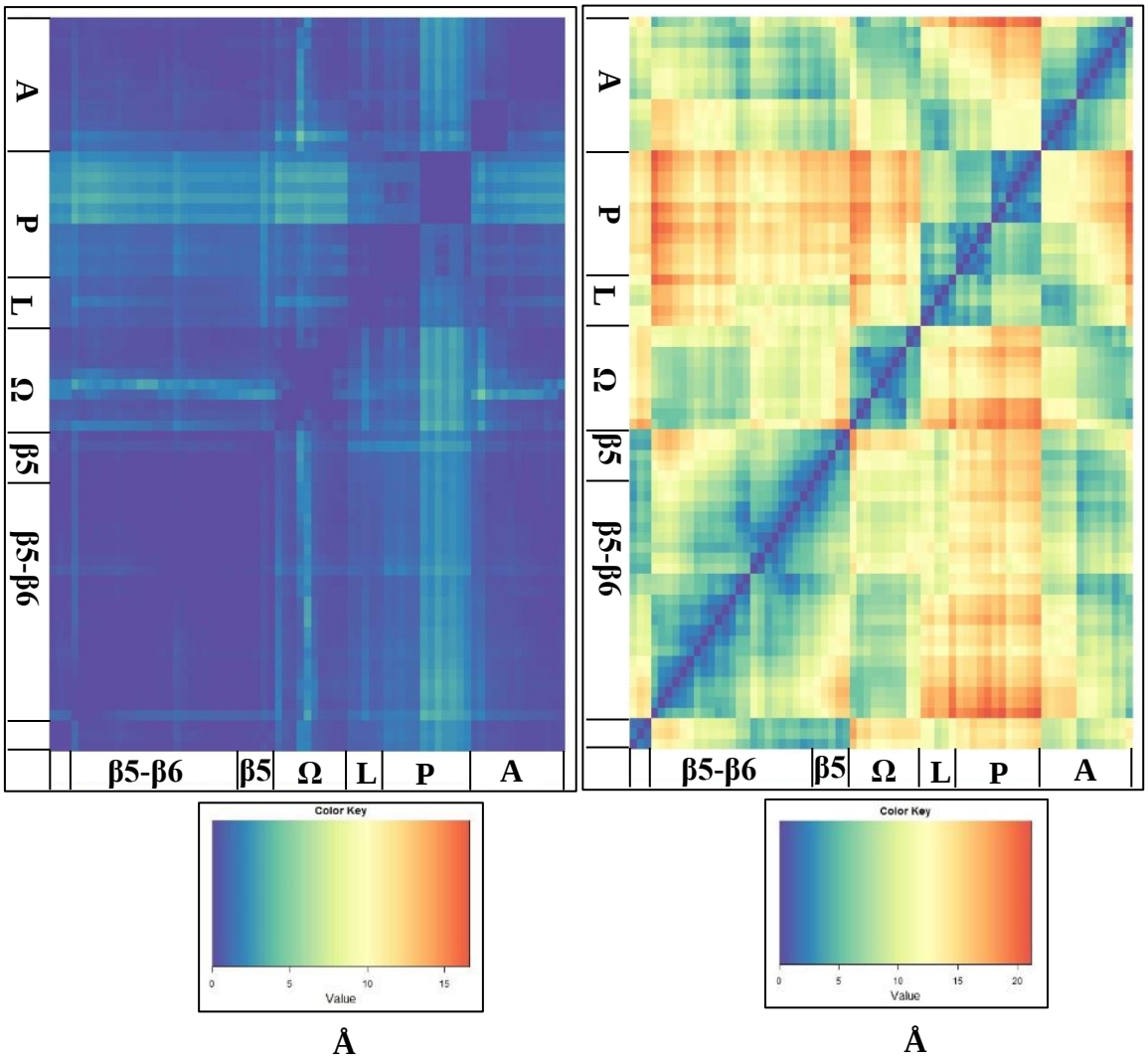

Fig. 20: Mean Distance Matrix & Distance Variances for Entire M223A Active Site. *Right*: Mean Distance Matrix. *Left*: Variance Matrix. Letters correspond to groups of atoms found within a specific area of the protein. **A**: Residues 80-84; **P**: P loop; **L**: Leu127 and Ser218; **Ω**: Ω loop; **β5**: β5 strand; **β5-β6**: β5-β6 loop; the last small region corresponds to Arg261.

The heatmaps allow us to detail which residues contribute the most to the fluctuation of the active site. Across all of the mutants, the distances between P loop and the β5-β6 loop show most of the variance. The majority of the variance in the fluctuations of the entire M223A active site stem from the distances between Tyr112 and the catalytic serine and general base, as well as all β5-β6 loop residues, Leu168, and Arg261. The single largest point of variance within M223A is the distance

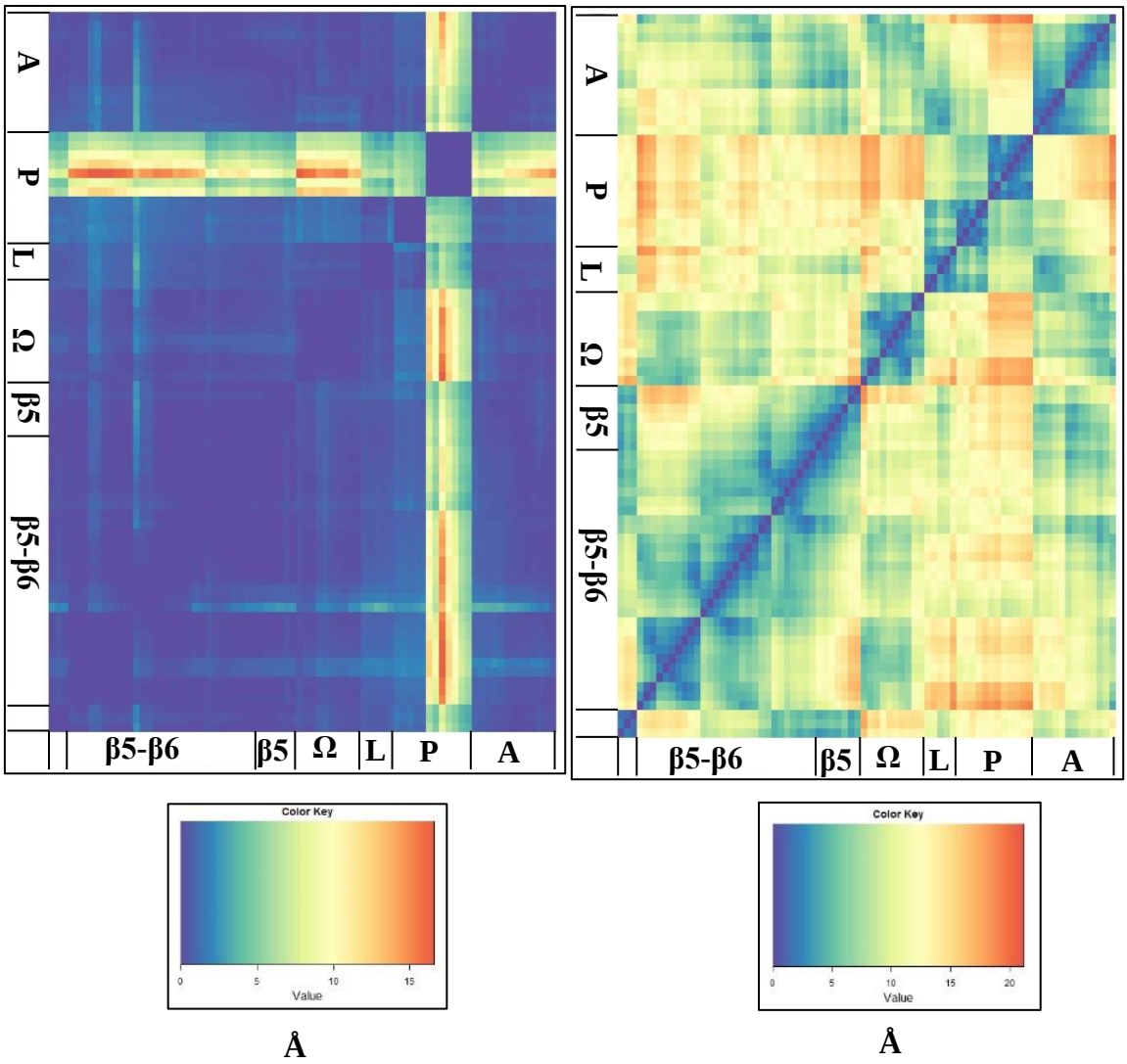

Fig. 21: Mean Distance Matrix & Distance Variances for Entire G224D Active Site. *Right*: Mean Distance Matrix. *Left*: Variance Matrix. Letters correspond to groups of atoms found within a specific area of the protein. **A**: Residues 80-84; **P**: P loop; **L**: Leu127 and Ser218; **Ω**: Ω loop;**β5**: β5 strand; **β5-β6**: β5-β6 loop; the last small region corresponds to Arg261.

between KCX84's OQ1 and Leu168's CD2. This is likely caused by the tendency for KCX84 to hydrogen bond with Ser81 and Lys218, instead of Ser81 and Trp167 – a ~6 Å shift. Variance in the G224D distances is a result of the fluctuations between Tyr112, and all other atoms in the defined active site. The largest variances, across all proteins, stem fromTyr112's side chain oxygen atom in the G224D mutant. Met223's Cε also reveals an increased variance in its distance to active site residues (Ser81,

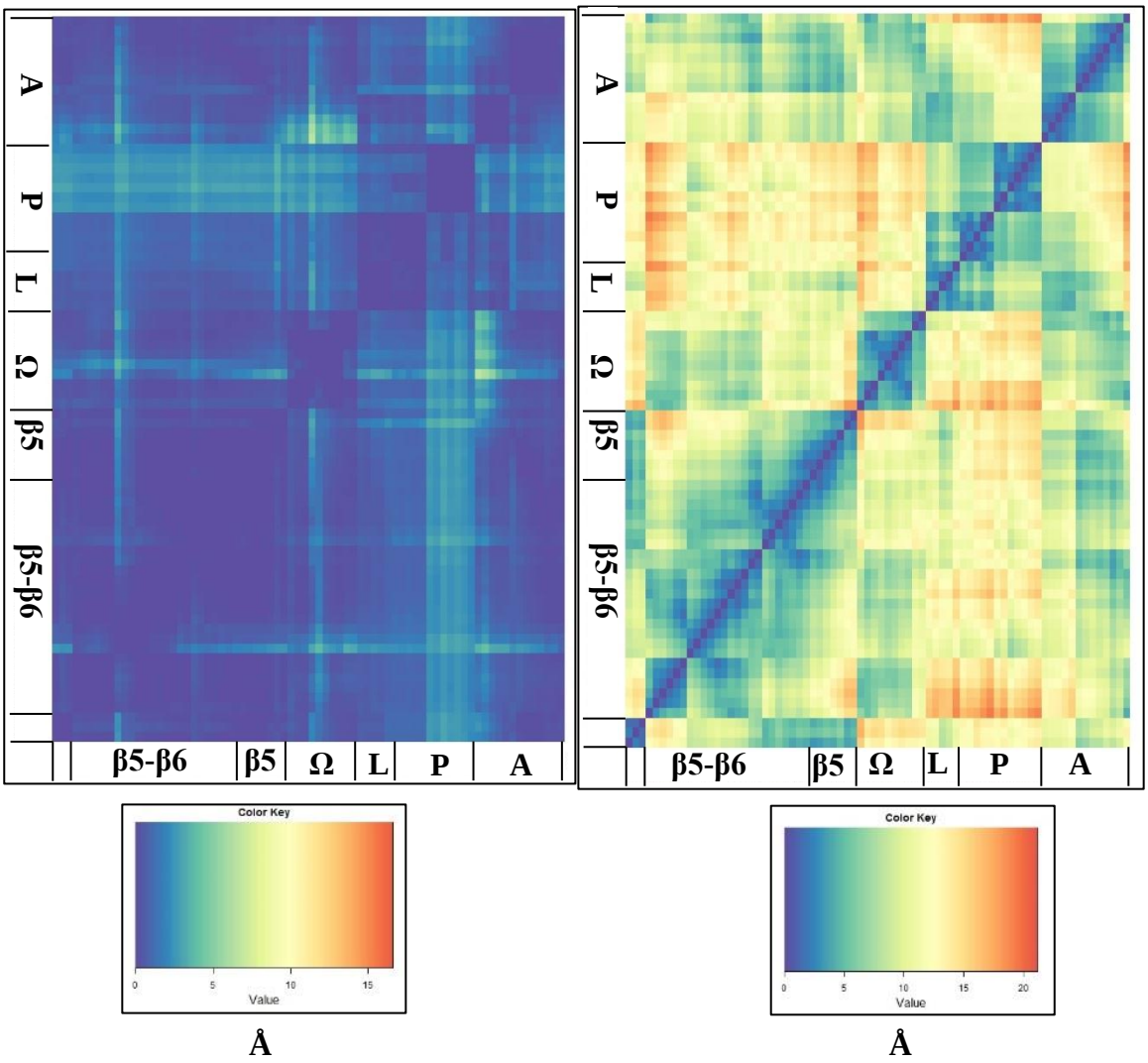

Fig. 22: Mean Distance Matrix & Distance Variances for Entire P227S Active Site. *Right*: Mean Distance Matrix. *Left*: Variance Matrix. Letters correspond to groups of atoms found within a specific area of the protein. **A**: Residues 80-84; **P**: P loop; **L**: Leu127 and Ser218; **Ω**: Ω loop;**β5**: β5 strand; **β5-β6**: β5-β6 loop; the last small region corresponds to Arg261.

KCX84), Tyr112, and Leu127 and Ser128. The P227S mutant shows increases in average distances over the WT between the P loop/Ser128 and the β5-β6 loop - though generally these increases are not more than 1 Å – and the distances between Val169 and the β5-β6 loop shows decreases. These results correspond well with the previously determined average distances (Table 16, Appendix C). The largest increase in variance – as with the M223A mutant– likely depicts the preference of the KCX

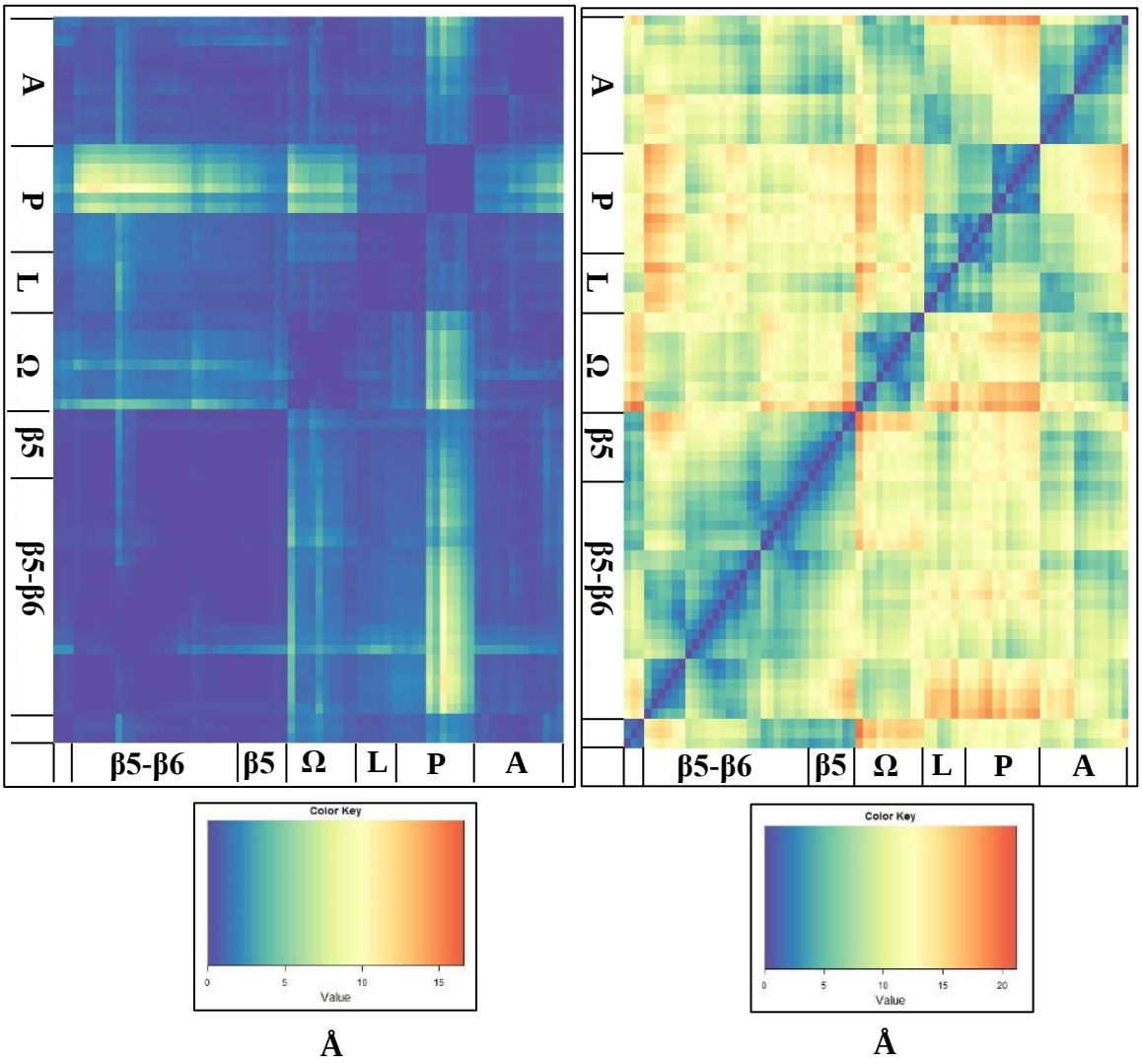

Fig. 23: Mean Distance Matrix & Distance Variances for Entire WT Active Site. *Right*: Mean Distance Matrix. *Left*: Variance Matrix. Letters correspond to groups of atoms found within a specific area of the protein. **A**: Residues 80-84; **P**: P loop; **L**: Leu127 and Ser218; **Ω**: Ω loop;**β5**: β5 strand; **β5-β6**: β5-β6 loop; the last small region corresponds to Arg261.

residue to hydrogen bond with Lys218 over Trp167. The largest decrease in P227S variance is between the side chain atoms of Tyr112 and Met223-Gly224; which may suggest that the P loop is in a fixed conformation, despite being ~1Å further from the β5-β6 loop. The WT shows the second greatest variance in P loop distances to the β5-β6 loop, which may reflect the WT loop's larger RMSF relative to the mutants. Average distances also aid in describing which residues contribute to active site

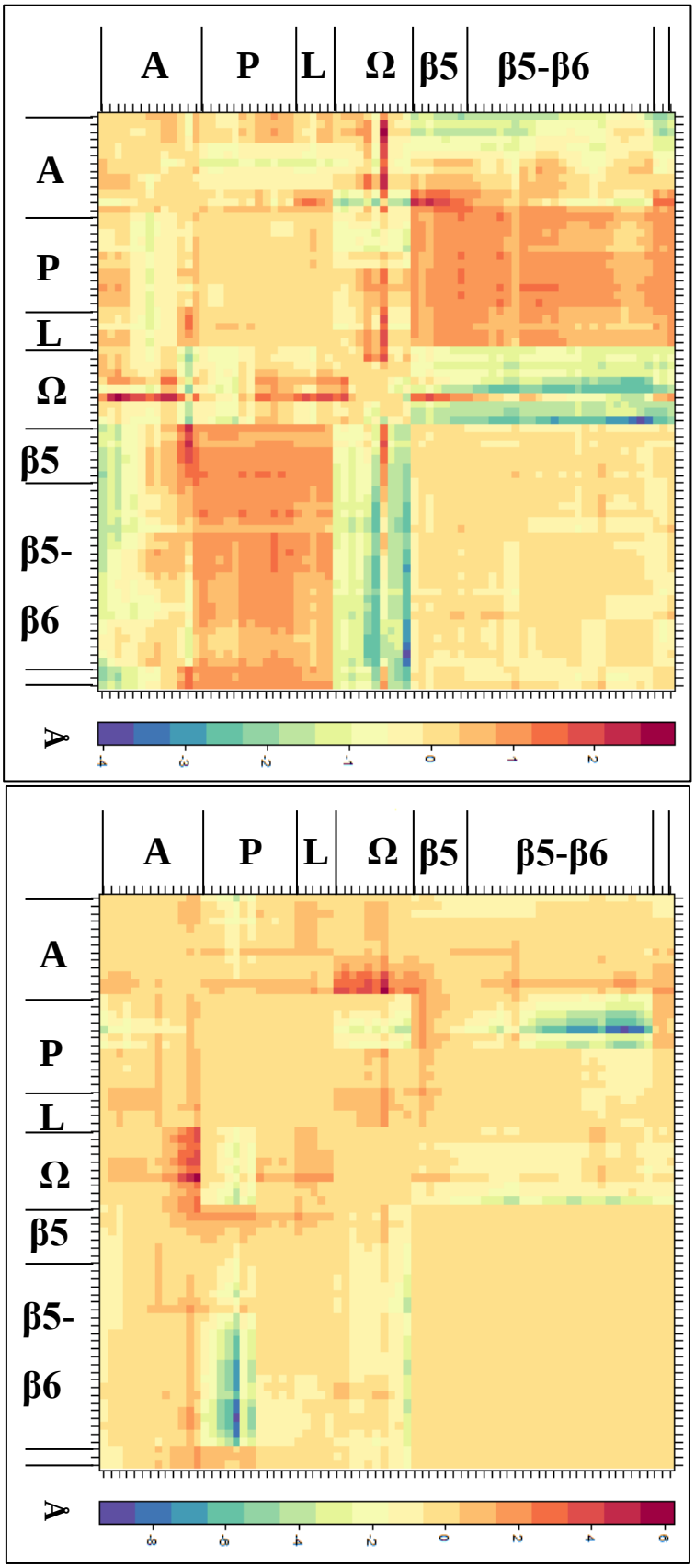

Fig. 24: Mean Distance & Variance Difference Matrices for P227S and WT. *Top*: Difference between mean distances. *Bottom*: Difference between variances of mean distances. Differences were calculated by subtracting WT values from P227S values. Therefore, red colors indicate increases in average distance and variance of P227S over WT; blue colors indicate the opposite. Letters correspond to groups of atoms found within a specific area of the protein. **A**: Residues 80-84; **P**: P loop; **L**: Leu127 and Ser218; **Ω**: Ω loop; **β5**: β5 strand; **β5-β6**: β5-β6 loop; the last small region corresponds to Arg261.

	WT Avg. (Å)	M223A Avg. (Å)	G224D Avg. (Å)	P227S Avg. (Å)
Leu168Cα - Glu251Cα	17.55 ±0.48	15.66 ±0.42	15.87 ±0.40	15.92 ±0.38
Leu168Cα - Arg261Cα	19.78 ±0.94	18.71 ±0.59	18.70 ±0.52	18.80 ±0.56
Leu168Cα - Met/Ala223Cα	9.36 ±1.09	8.18 ±0.52	8.25 ±0.36	8.13 ±0.47
Met/Ala223Cα - Arg261Cα	14.88 ±0.48	14.70 ±0.46	14.67 ±0.46	14.68 ±0.50
Met/Ala223Cα - Glu251Cα	10.71 ±0.37	10.31 ±0.33	10.67 ±0.37	10.55 ±0.37
Ser81Cα - Ser128Cα	7.90 ±0.52	8.77 ±0.48	8.09 ±0.43	7.51 ±0.82
Ser81Cα – Tyr112Cα	16.20 ±0.91	17.21 ±0.96	17.22 ±1.79	15.79 ±0.96
Ser128Cα - Ser219Cα	8.74 ±0.57	10.66 ±0.77	9.41 ±0.64	9.65 ±0.71
Ser128Oγ - Ser219Oγ	6.77 ±0.88	8.63 ±1.33	7.72 ±0.82	7.35 ±1.27
Tyr112Cα - Met/Ala223Cα	15.03 ±1.63	18.19 ±1.28	15.85 ±1.92	16.23 ±1.39

Table 10: Distances Across Active Site. Distances selected from Table 16, Appendix C.

volume differences (Table 10).

The average distances help show the P loop's role in affecting the volume of all mutants. There is a ~3 Å increase in the distance between the Cα atoms of Tyr112 and Met/Ala223 in the M223A mutant, and ~1 Å increase the P227S mutant. Also observed is an increase in the distance between the Cα atoms of Tyr112 and the catalytic Ser81 in the M223A and G224D mutants. This is also seen when examining the heatmaps. The distance between Ser128 and Ser219 increasing in all of the mutants also shows an opening of the active site. Ser128 acts as part of the "roof" of the active site, while Ser219 is located just prior to the β5-β6 loop. The distance between the Ω and β5-β6 loop is shown to decrease based on the average distances (Leu168 to Met/Ala223), and the mean distance heatmaps as well; this was observed in the previous section which described the average structures of the mutants.

3. Further Analysis of P227S Mutation

Because the P227S mutation results in a particularly striking change in substrate selectivity, additional analyses were carried out for this mutant. We examined how this mutation might affect the enzyme in two different ways: (i) as a potential hydrogen bond center, and (ii), with regard to substrate selectivity/ligand binding by docking antibiotics to unique conformations from the WT and P227S trajectories.

3A. Ser227-Glu251 Hydrogen Bond

Replacing the proline should result in an increased dihedral freedom for residue 227, which in turn would allow the β5-β6 loop to explore more conformations. We initially hypothesized that the P227S mutation would increase fluctuations of the β5-β6 loop. Interestingly, the dynamics observed during simulations reflect the opposite. As detailed in the previous section (Comparison of Mutant Dynamics), the P227S mutation results in a less flexible β5-β6 loop. The reason for this decreased flexibility is likely due to the formation of a hydrogen bond between Ser227 and Glu251 (Fig. 25).

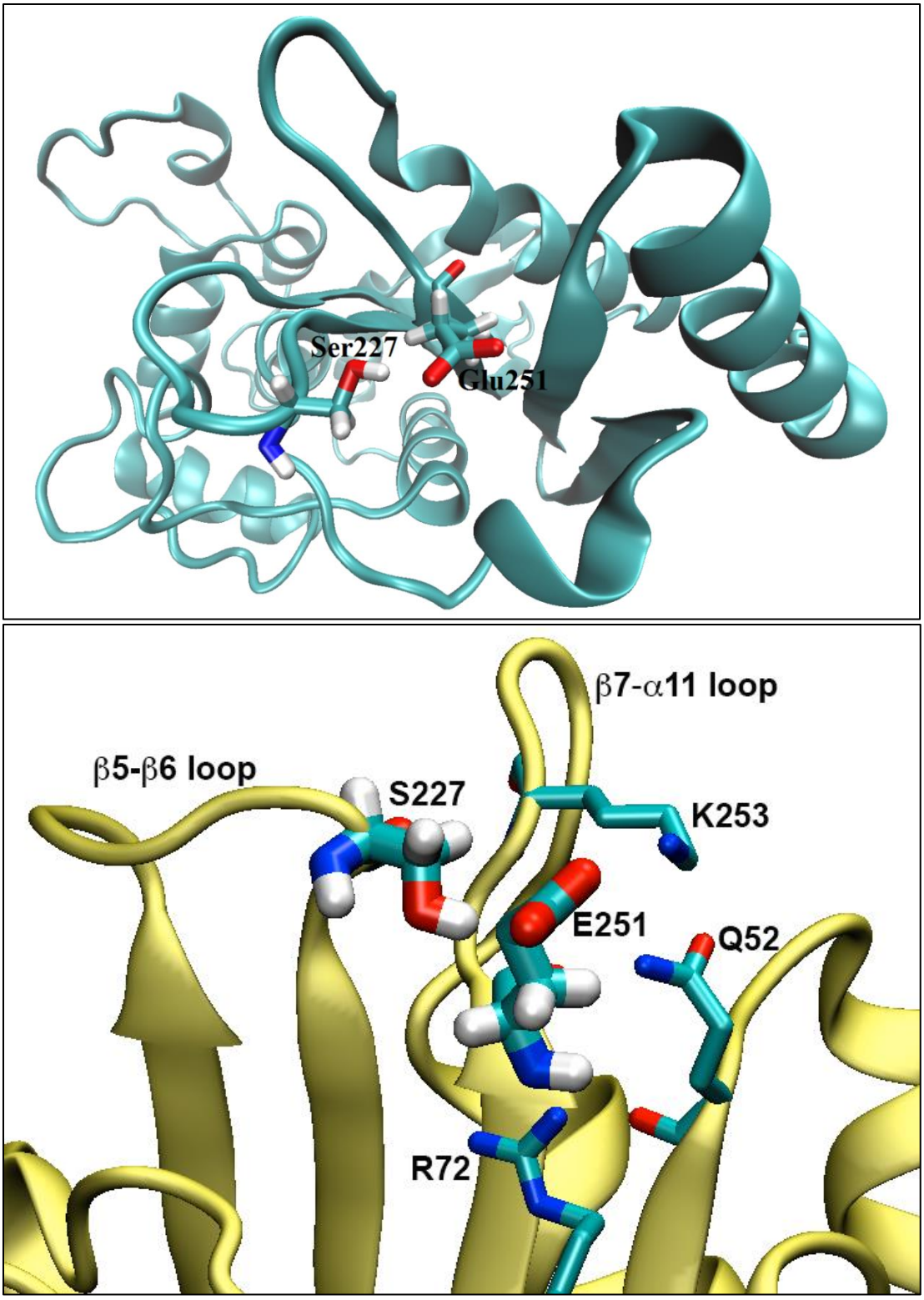

Fig. 25: Ser227-Glu251 Hydrogen Bond. *Top*: Image taken from 20.2 nsec point. Distance between donor and acceptor is 2.65 Å. Distance between hydrogen and acceptor is 1.69 Å; donor-hydrogen-acceptor angle is 176°. *Bottom*: Other hydrogen bond donors in close proximity to Glu251. Figure adapted from Mitchell et al. (2015).

Based on the hydrogen bonding criteria of a donor-acceptor distance of <3.2 Å and a donor-hydrogen-acceptor angle of 120°-180°, Ser227's Oγ hydrogen bonds to Glu251's Oε atoms during 76% of the trajectory (Fig. 26), with an average donor-acceptor distance of 2.73 ±0.99 Å while the hydrogen bond is formed (average over trajectory is 3.84 ±0.99 Å). In the WT trajectory, Pro227's Cγ is within a similar distance during 0.4% of the trajectory; Glu251 instead hydrogen bonds with Lys253, Arg72, and Gln52 for 33%, 29%, and 14% of the trajectory respectively. None of these interactions with Lys253, Arg72, and Gln52 are present in the P227S trajectory to the same extent; Glu251 in the P227S mutant hydrogen bonds to Lys253, Arg72, and Gln52 for 6%, 3%, and 7% of the trajectory respectively.

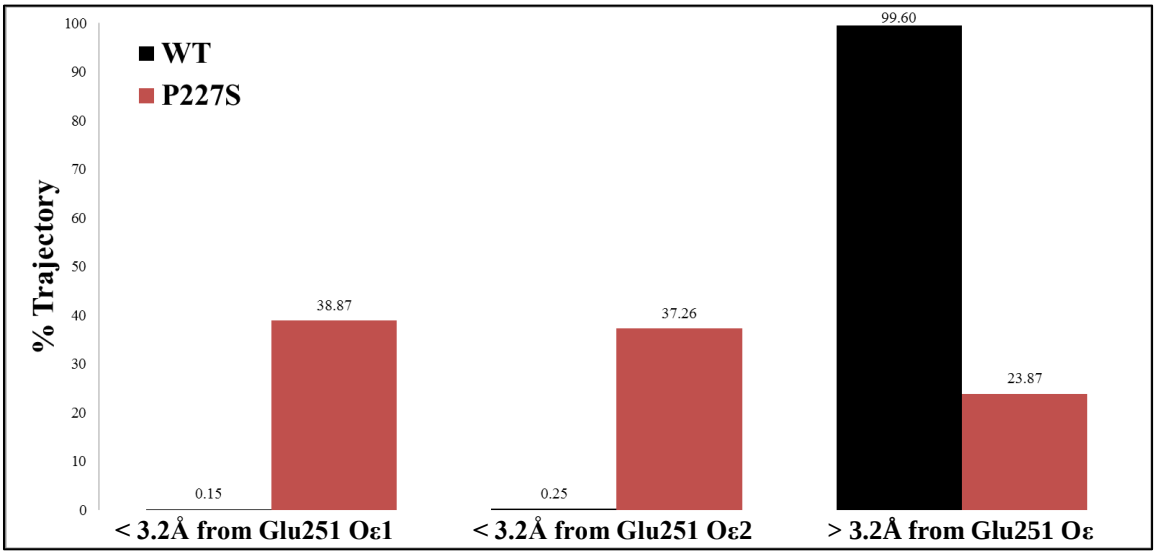

Fig. 26: Hydrogen Bonding Distance. Bars represent the distribution of frames with Ser227 (Oγ atom, red) or Pro227 (Cγ atom, black) residing within the hydrogen bonding distance from Glu251 or outside of this range. Angle criteria is not presented in figure as comparison with WT would not be possible. Figure adapted from Mitchell et al. (2015).

3B. Exploration of β5-β6 Conformations using RMSD

As we have observed changes in the overall RMSD and RMSF profiles of β5-β6 loop in the two proteins, it was likely that the loop may have different conformational ensembles. We used loop RMSD as the criterion to identify conformational clusters within each trajectory. Trajectories were aligned by all Cα atoms, and the RMSD of the β5-β6 loop was calculated. The RMSD values were sorted in the ascending order, and every 0.5 Å increment was specified as a bin. RMSD values from 0-0.5 Å were designated as Bin 1, 0.51-1.0 Å was Bin 2, etc. Two structures from each RMSD range was saved for comparison – the very first and middle structure of each 0.5 Å range of RMSD values. The structures acquired can be seen below in Fig. 27.

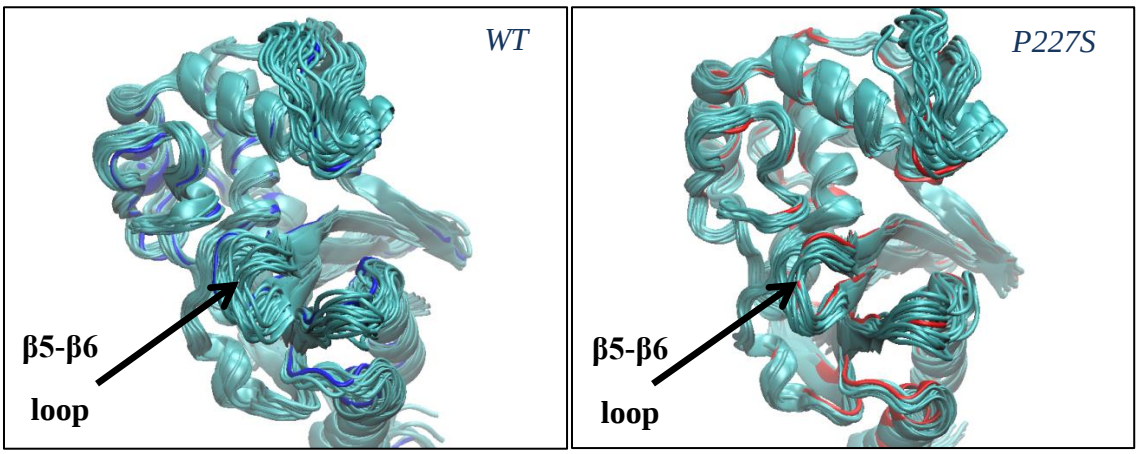

Fig. 27: WT & P227S Binned Structures. *Left*: WT structures. WT reference frame (frame 0) in dark blue. *Right*: P227S structures. P227S reference frame (frame 0) in red.

The WT trajectory contained 10 bins, P227S contained 7 bins, indicating that there is greater conformation diversity in the WT enzyme. This finding is consistent with our previous RMSD/RMSF data. The β5-β6 loop adopts two main conformation in the P227S mutant (Fig. 28). β5-β6 loops from the lowest, middle, and highest RMSD values

can be seen below in Fig. 28A-B. The new conformations show a widening of the space between the β5-β6 loop and the P loop (Fig. 28C-D), a trend which is not seen in the WT.

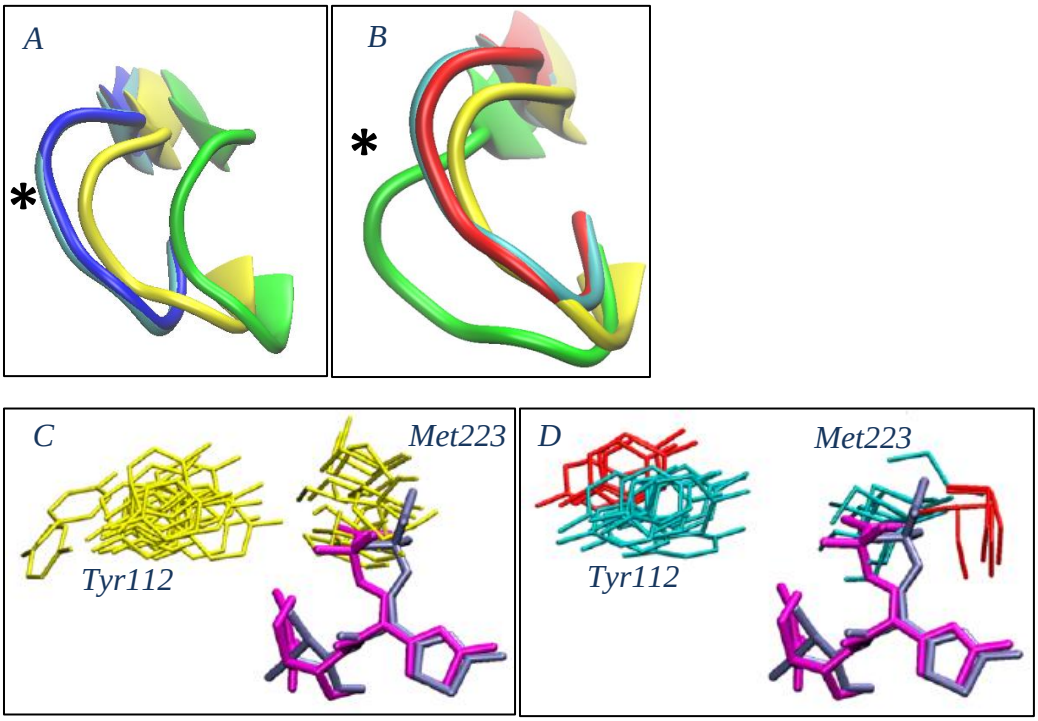

Fig. 28: Selected β5-β6 Loop Conformations from Binned Structures. *A*: Loops from WT trajectory. Reference frame is blue, 0.29 Å structure in cyan, 2.23 Å structure in yellow, 4.57 Å structure in green. *B*: Loops from P227S trajectory. Reference frame is red, 0.30 Å structure in cyan, 1.51 Å structure in yellow, 3.05 Å structure in green. *C*: Side chain positions in WT binned structures. *D*: Side chain positions in P227S binned structures. Trajectories aligned by all Cα atoms. *Ω loop located to left of β5-β6 loop in figures. *C-D* adapted from Mitchell (2015); ceftazidime (magenta), aztreonam (blue).

3C. Docking of Doripenem to Selected Trajectory Frames

Identification of different, unique conformations present in the P227S and absent in the WT trajectory would allow us an opportunity to explore different binding modes of antibiotics. Docking simulation of diverse ligands to multiple protein target frames not only has a potential to explain the ligand selectivity, but also allows us to incorporate some protein flexibility aspects into the overall docking results. In this part of the project,

we conducted a set of preliminary tests on a small number of selected frames for doripenem binding. The following sections described the process, docking parameters, and selected frames.

3C-1. Docking Protocol

The docking protocol would be considered accurate if crystallographic conformations of the acylated antibiotic could be reproduced sufficiently, and if the binding affinity (K_m, calculated by AutoDock as K_i) were consistent with *in vitro* values. The crystal structure used for the validation was OXA-24 complexed with doripenem (contained KCX84D mutation to prevent deacylation, PDB 3PAE) (Schneider 2011). The Hγ present on Ser81 was removed to best represent the physiologic state of the enzyme when using the acylated form of the antibiotic for docking (in general, hydrogens were added only to all polar atoms in the protein target).

Our first goal was to determine which Lamarckian GA settings will produce the closest agreement between the experimentally determined ligand conformation and the predicted one. As criteria we used distances between (i) Leu168 and doripenem's 6' carbon, (ii) Ser81 to the β-lactam rings' carbonyl carbon, (iii) doripenem's carboxylate oxygens to Arg261, and (iv) Trp221's backbone nitrogen to the β-lactam's carbonyl oxygen. We have tested both acylated doripenem (cleaved β-lactam ring), and intact (Michaelis complex) doripenem. Optimized Lamarckian GA parameters were population size, number of energy evaluations, number of GA runs, box size, and grid spacing. The Lamarckian GA parameters were optimized when computational time was minimized while still acquiring satisfactory docking results. A large population size (750

individuals) produced results that best represented the crystal structure. Grid spacing was reduced from 0.325 Å to 0.225 Å, and the size of the grid box was altered to include residues which are important for receptor-ligand interactions. Final CPU time was ~20 minutes per GA run.

3C-2. Docking of Acylated Doripenem

Fig. 29 shows a comparison between the crystallographic acyl-doripenem, and the docked conformation. Table 11 details important interactions between acyl-doripenem and the OXA-24 active site.

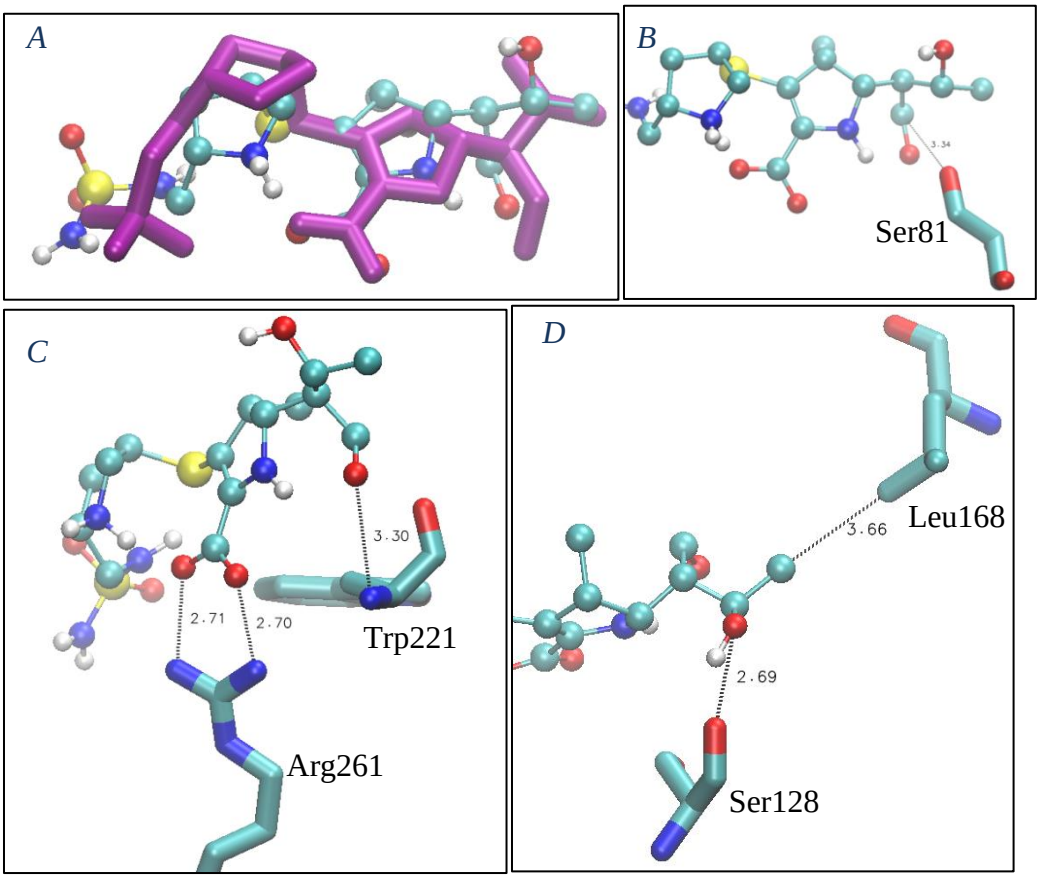

Fig. 29: Comparison of Acyl-Doripenem Structures. *A*: Structure drawn in Licorice and colored purple is the acyl-doripenem from 3PAE. The RMSD between the docked acyl-doripenem and the crystallographic acyl-doripenem is 1.4 Å. *B-D*: Structure drawn as ball-and-sticks is the docked acyl-doripenem. Residue hydrogens not present in crystal structure.

The predicted (docked) orientation of the ligand is correct with respect to the binding of the carboxylate to Arg261, and the 6' carbon/Leu168 interaction. This is a very positive outcome as the carboxylate group likely serves as the positioning anchor for the antibiotic with respect to the catalytic residues.

Among the differences between the docked acyl-doripenem and the crystallographic structure is that the 6'-oxygen atom has shifted to hydrogen bond with Ser128's backbone oxygen (Fig. 29D) instead of being oriented towards Tyr112. The 2 Å difference in the distance from Ser81 to the cleaved β-lactam carbonyl carbon may be a result of the lack of the enzyme-antibiotic covalent bond, as this could not be modeled using AutoDock4.

3C-3. Docking of Doripenem Michaelis Complex

To be able to compare the calculated binding energy with the experimental K_m for doripenem, an un-acylated version was docked to WT OXA-24. Unfortunately, the Michaelis-complex of doripenem and OXA-24 has never been determined using X-ray crystallography, so a direct comparison of the docked results to a crystal structure is not possible. Fig. 30 shows the docked doripenem structure in the OXA-24 active site.

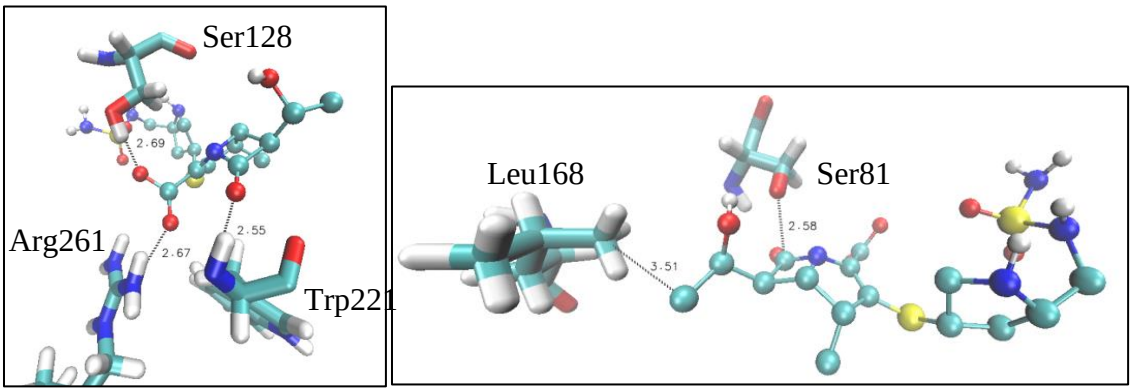

Fig. 30: Docked Michaelis Complex of Doripenem.

	Ser81 Oγ to β-lactam Carbonyl Carbon (Å)	Leu168 to 6-carbon (Å)	Trp221 Backbone Nitrogen to β-lactam Carbonyl Oxygen (Å)	Arg261 Side-chain Nitrogens to Doripenem Carboxylate Oxygens (Å)
Docked Acyl-Doripenem Structure	3.3	3.7	3.3	2.7, 2.7
Docked Doripenem Structure	2.7	3.5	2.6	2.7, 4.3
PDB 3PAE	1.3	3.2	2.7	2.9, 2.8

Table 11: Docked Doripenem Comparison in WT OXA-24. Values given are distances between specified atoms.

A number of interactions present in the crystallographic acyl-doripenem structure are also present in the docked Michaelis complex (Table 11). Namely the 6' carbon and Leu168, and the interaction between Trp221 and the carbonyl oxygen on the β-lactam ring. The distance between the catalytic serine and the β-lactam carbonyl carbon has also decreased. Interestingly, one of the carboxylate oxygen atoms of doripenem has hydrogen bonded to Ser128's side-chain oxygen (2.7 Å; Fig. 30, left) instead of Arg261 as seen in the crystal structure. The calculated K_m is 0.032μM; the experimental K_m of OXA-24 for doripenem is 0.024 ±0.003μM (Kaitany 2013).

Since key interactions were observed in both the docking of the acyl-doripenem and the Michaelis complex with good agreement, we proceeded to select unique structures in both the WT and P227S trajectories for the docking of the doripenem Michaelis complex. Although the previous RMSD-based analysis of conformational clusters provided interesting insights into the dynamics of the β5-β6 loop, we decided to pursue a different analysis (of distribution of Φ and Ψ values) that would allow us to identify more precisely unique structures to serve as docking target frames.

3C-4. Selection of Structures using Φ/Ψ Analysis

The selection of the WT and P227S structures based on the β5-β6 loop Φ and Ψ angles revealed which residues contributed the most to the structural differences of the loop structure between the two enzymes. Gly222, Met223, Gly224, Val225, Thr226, and Gln228 were found to occupy similar dihedral ranges in both enzymes (Fig. 31).

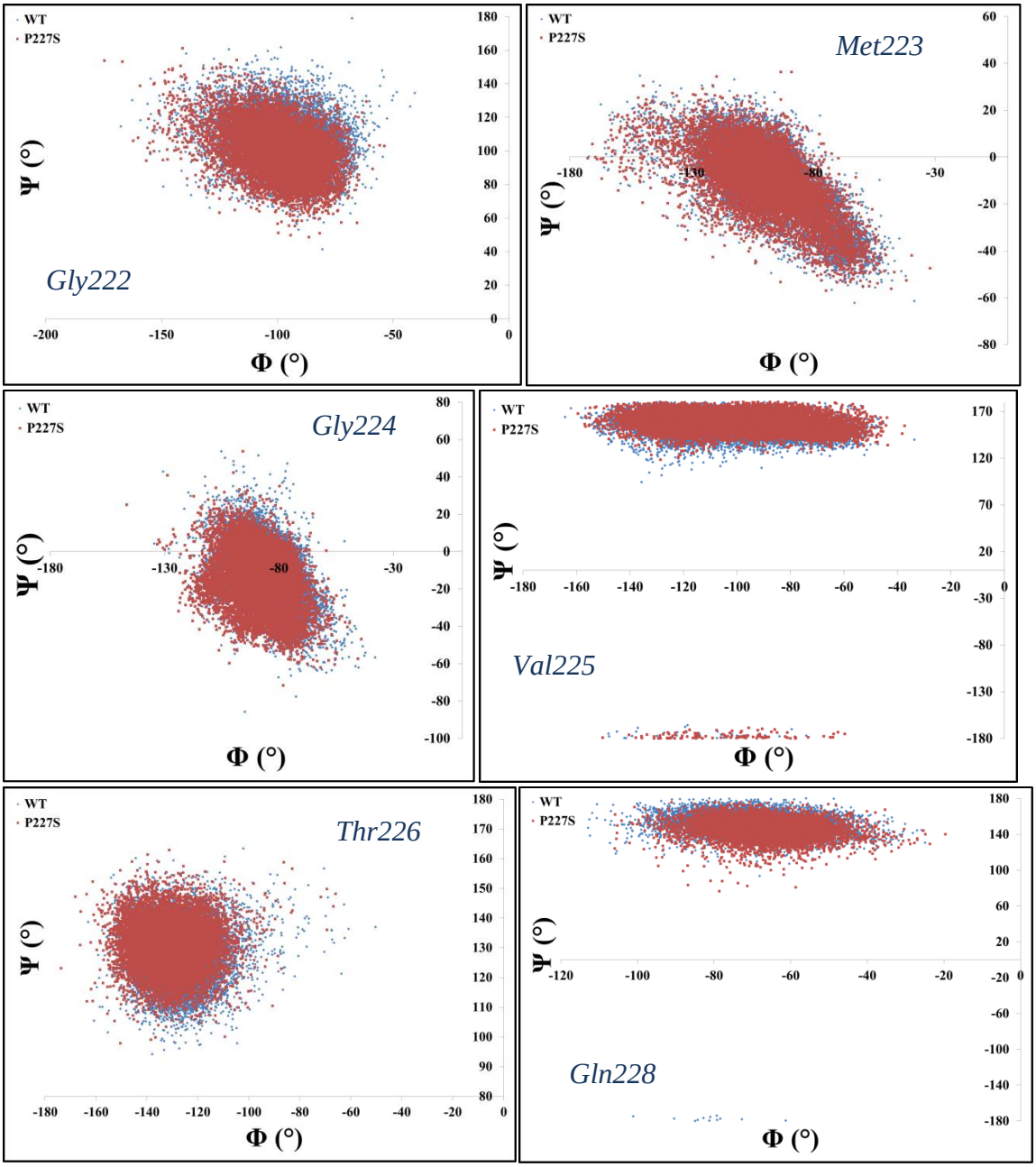

Fig. 31: Φ vs. Ψ Angles of Non-Contributing β5-β6 Residues.

Because residues in Fig. 31 adopted the same ranges dihedral angles in WT and P227S, conformational changes in the β5-β6 loop are unlikely to be caused by these residues. Further analysis of these distributions would be carried out to confirm this. However, Trp221, and Pro/Ser227 were found to adopt unique dihedral angles (Fig. 32).

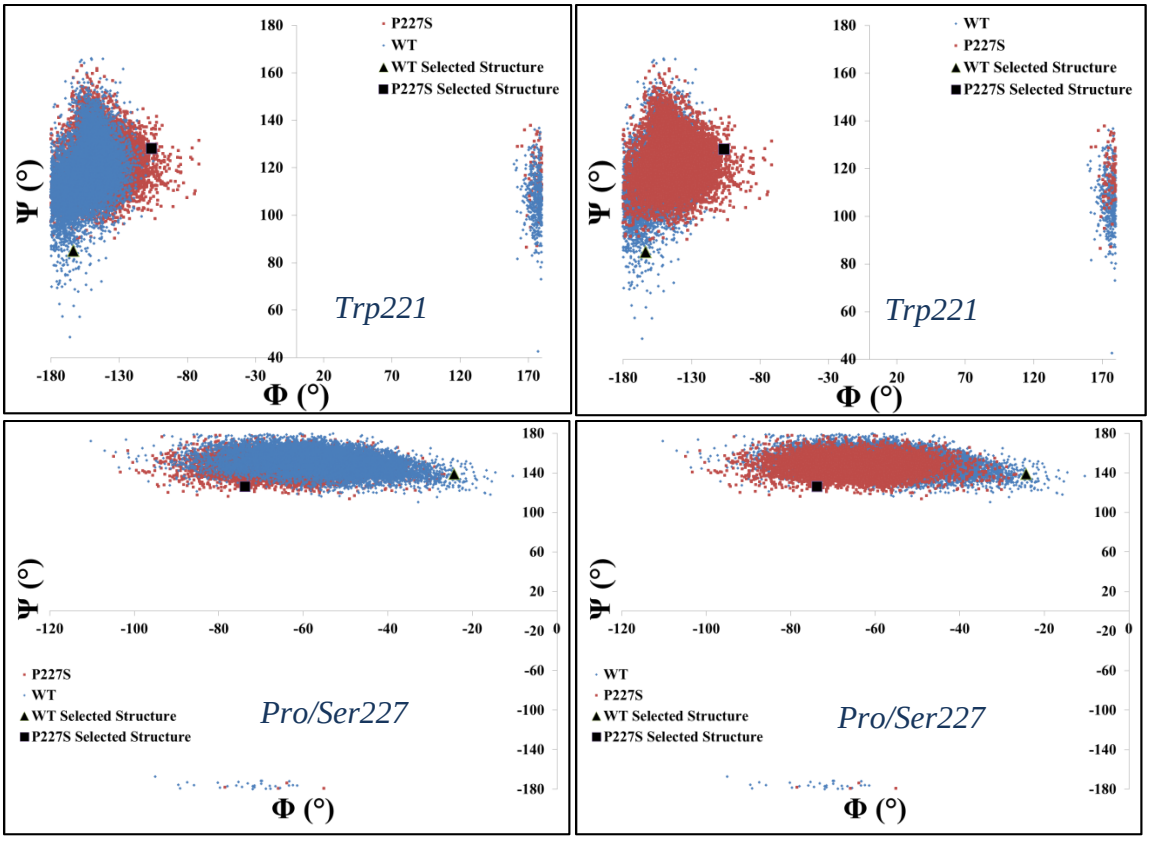

Fig. 32: Φ vs. Ψ Angles of Contributing β5-β6 Residues. *Top graphs*: Trp221 dihedral ranges; *Bottom graphs:* Pro/Ser227 dihedral ranges. WT values colored blue, P227S values colored red. Right graphs shows P227S data on top; left shows WT on top.

Thus, we were able to determine which residues in the loop adopt different conformations in P227S versus WT. We also identified some unique frames in P227S with Φ/Ψ values not observed in the WT, and vice versa that served as preliminary targets for our comparative docking tests. Given the preliminary nature of this part of our study the choice of unique frame was not rigorous. Further work including correlation analysis will be required to fully determine a much larger number of docking frames.

For this project, two structures were selected from the trajectories corresponding to unique Trp221 dihedral angles. A WT structure with Φ/Ψ values of -163.5°/85.1° was chosen to represent the range of dihedral values that the WT enzyme primarily occupied

(Fig. 32, upper right graph, *Structure A*). The corresponding P227S structure (Fig. 32, upper left graph) chosen had Φ/Ψ values of -166.1°/128.0° (*Structure B*). A WT structure with Φ/Ψ values of -24.9°/138.8° was chosen to represent the range of dihedral values in which the WT enzyme occupies more highly than P227S (Fig. 32, lower right graph, *Structure C*). The P227S structure chosen (*Structure D*) had Φ/Ψ values of -73.8°/126.0°.

A number of differences are present between the two structures chosen from the Trp221 Φ/Ψ comparison (Fig. 33).

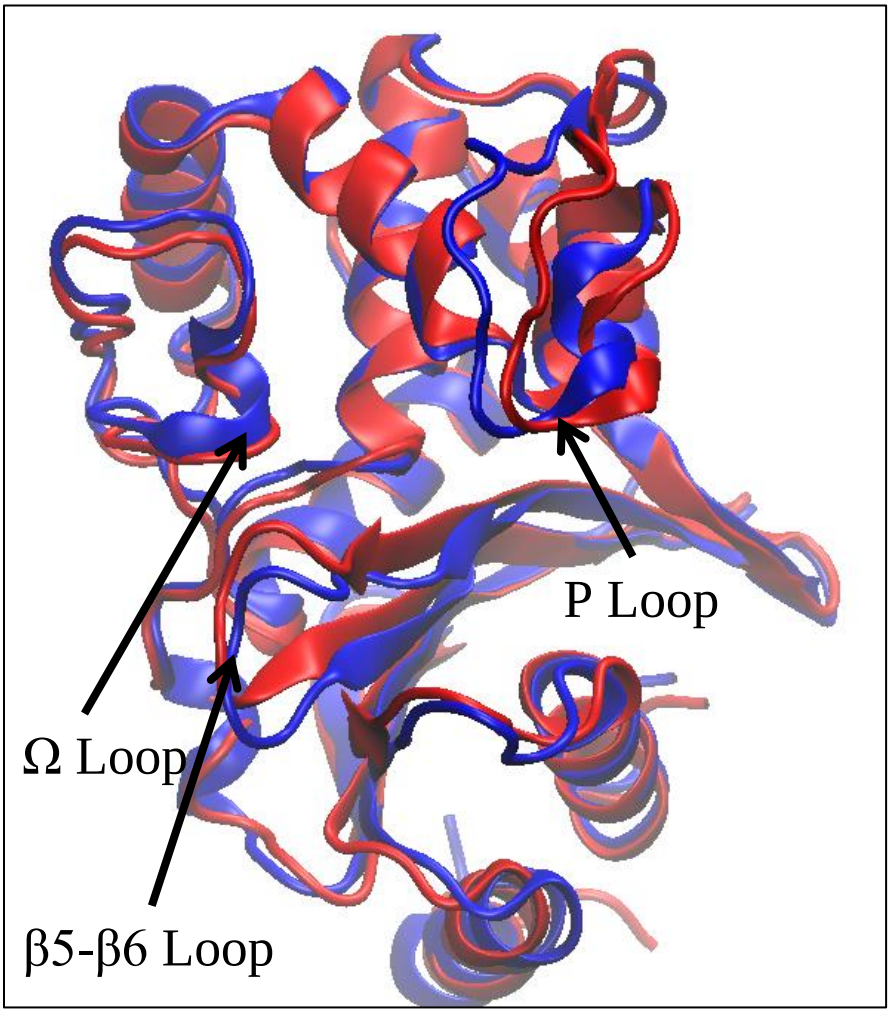

Fig. 33: Comparison of *Structure A* to *Structure B*. WT structure colored blue, P227S colored red.

The β5 strand does not end until Met223 in the P227S structure, and it ends 2 residues earlier in the WT at Trp221. The Ω loop in the WT structure acquires a partial-helix conformation from residues Phe166-Gly170.

Differences in the structures selected from the Pro/Ser227 Φ/Ψ analysis (Structures *C* and *D*) are present as well (Fig. 34). Similar to the Trp221 structures, the P loop of the P227S structure has moved away from the β5 strand, and the Ω and β5-β6 loops have shifted closer to each other. Unlike the Trp221 structures, both β5 strands end at the same residue, and the Ω loop does not acquire a partial-helix conformation within the WT structure.

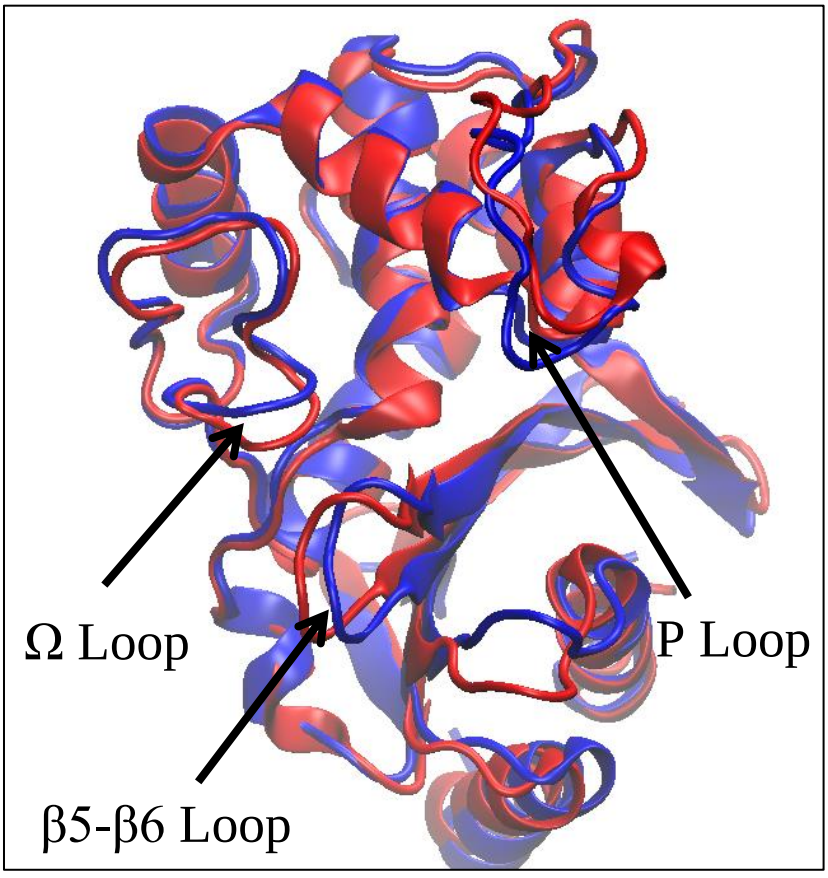

Fig. 34: Comparison of *Structure C* to *Structure D*. WT structure colored blue, P227S structure colored red.

Table 12 reiterates the Φ/Ψ analysis, and the differences between the WT and P227S structures selected for the docking of the doripenem Michaelis complex.

Structure	Φ (°)	Ψ (°)	Structure Acquired from Trajectory	Residue with Unique Φ/Ψ Value
A	-163.5	85.1	WT	Trp221
B	-166.1	128.0°	P227S	Trp221
C	-24.9°	138.8°	WT	Pro227
D	-73.8°	126.0°	P227S	Ser227

Table 12: Summary of Structures Acquired from Φ/Ψ Comparison.

These 4 structures were utilized with the previously described docking protocol (section 3C-1) to determine if unique binding modes would be present between the WT and P227S structures.

3C-5. Docking of Doripenem to Selected Structures

The previously described 4 structures (*A*, *B*, *C*, and *D*) subsequently had doripenem docked as the Michaelis complex. The docking of doripenem to these structures (Fig. 35, Table 13) produced docked complexes which had few similarities to the previously acquired Michaelis complex in Fig. 30. To try and acquire the two most plausible docked conformations, one was visually selected on the basis of the receptor-ligand interactions previously seen in the acyl-complex and the Michaelis complex (designated via "V.O." in Fig. 35 and Table 13); another structure was selected which had the most similar binding energy to that of the experimentally determined value (designated via "B.E." in Fig. 35 and Table 13).

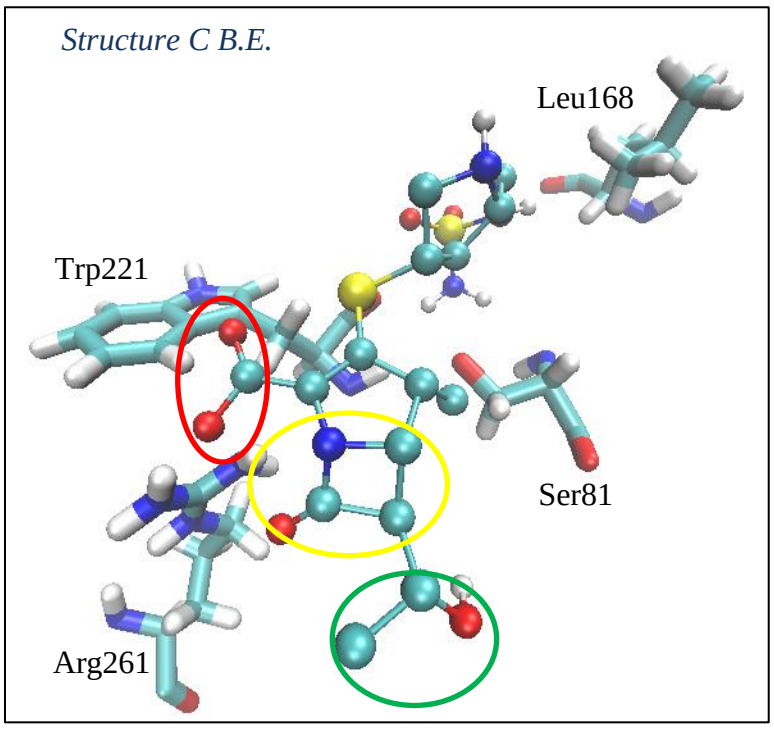

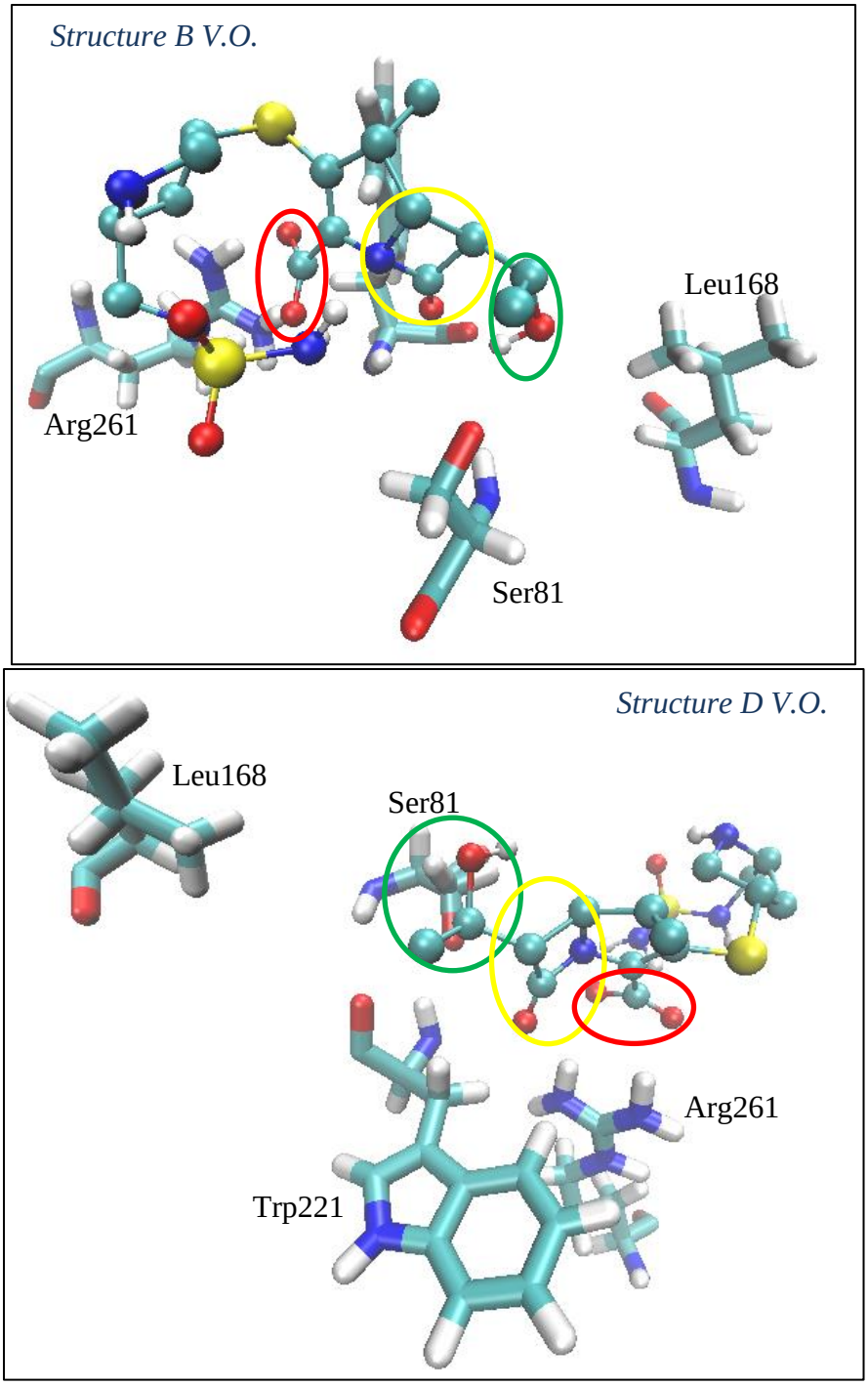

Fig. 35: Doripenem Docked to Selected Structures. Carboxylate circled in red, β-lactam ring circled in yellow, 6'-hydroxyethyl circled in green. Not all docked ligand complexes are depicted. Ligands shown above illustrate the best orientations acquired from the docking. *Top*: Most similar binding energy to the experimental value. *Middle:* Docked complex with most interactions present to some degree. *Bottom*: Nearly all interactions present, with the best Ser81 Oγ to β-lactam interaction.

	K_i (μM)	Increase/Decrease from Experimental Binding Energy (factor)	Ser81 Oγ to β-lactam Carbonyl Carbon (Å)	Leu168 to 6-carbon (Å)	Trp221 Backbone Nitrogen to β-lactam Carbonyl Oxygen (Å)	Arg261 Side-chain Nitrogens to Doripenem Carboxylate Oxygens (Å)
Ex. OXA-24	0.024 ±0.003	N/A	1.3	3.2	2.7	2.9, 2.8
OXA-24 M.C.	0.032	1.3x	2.7	3.5	2.6	2.7, 4.3
Ex. OXA-160	0.014 ±0.003	N/A	N/A	N/A	N/A	N/A
Structure A V.O.	13.62	567.5x	4.9	7.5	3.3	2.6, 3.1
Structure A B.E.	0.336	14x	8.9	15.8	8.3	2.7, 2.9
Structure B V.O.	194.76	8115x	3.7	7.8	2.9	2.8, 2.8
Structure B B.E.	0.209	8.7x	5.1	14.2	5.6	3.2, 4.2
Structure C V.O.	2.19	91.3x	4.4	6.3	2.9	2.9, 3.0
Structure C B.E.	0.115	4.8x	6.7	14.5	5.3	3.0, 4.3
Structure D V.O.	57.48	2395x	3.1	6.4	3.3	3.0, 3.3
Structure D B.E.	2.14	89.2x	7.4	14.8	6.6	6.5, 6.6

Table 13: Comparison of Docked Doripenem to WT/P227S Selected Structures. *Ex.*, experimental; *M.C.*, Michaelis Complex; *V.O.*, Orientation selected visually; *B.E.*, Orientation selected based on binding energy. Binding energies acquired from Mitchell et al. (2015). Highlighted orientations are shown in Fig. 35.

Few of the docked structure resemble the Michaelis complex acquired during the docking validation protocol. As we saw in the test runs, the majority of docked structures contain the interaction between the doripenem carboxylate and Arg261, in fact the only structure that lacks this interaction is the *Structure D B.E.* However, for this limited number of target frames the remaining interactions between the antibiotic and the protein binding pocket do not indicate productive binding. For example, the ligand orientation with the most similar binding energy to the experimental values - the *Structure C B.E.* – contains the antibiotic in a poor position for hydrolysis (Fig. 35, top). The 6'-

hydroxyethyl is >14.7 Å from Leu168 and Ser81 is ~7 Å from its target atom on the β-lactam ring. The sulfonamide tail of doripenem is also positioned on the opposite side of the active site, near the Ω and β5-β6 loops.

The ligand orientation in the *Structure D V.O.* (Fig. 37, middle) is also incorrect. Leu168 is 6.4 Å from the 6'-hydroxyethyl carbon, and the 6'-hydroxyethyl oxygen has hydrogen bonded with the carboxylated lysine (donor-acceptor distance of 3.1 Å); an interaction that is proposed to prevent the deacylation step of catalysis (Schneider 2011). Only one ligand orientation has the Ser81 Oγ to β-lactam distance under 3.5 Å: the *Structure D V.O.* None of the docked ligands have the Leu168 and 6'-hydroxyethyl within sufficient distance for a hydrophobic interaction to occur.

In summary, much more work is needed in order to develop a rigorous method of selected a large set of representative frames for docking, as well as to test more carefully the potential energy function and distribution of atomic charges in our docking model. The latter likely contributes to the problem with intact antibiotic binding.

CHAPTER IV

DISCUSSION

1. RMSD

Based on the RMSD data presented, all three substitutions in the β5-β6 loop affects the dynamics of OXA-24. The Ω and β5-β6 loops for the mutants all show less structural drift from their initial conformation than the WT, while the P loops show increased drift. The mutations also affect the active site of the enzyme. These effects are discussed in detail in part 3 (Active Site Dynamics) of this discussion.

2. Compactness and Volume

Based on the R_{gyr} as a measure of protein compactness, all 3 mutants are less compact than the WT. We hypothesized that the radius of gyration may be correlated with the active site volume (widening of the cleft between the domains), but it turned out not to be the case. Instead the volume calculations show the WT as having the greatest average whole active site volume, despite the lower R_{gyr}. It must be noted, however, that we traced the volume of the active site as a fraction of the entire cleft only. Interestingly, the volume of the lower portion of the active site increases relative to the WT enzyme, which supports the notion that a larger active site will allow the OXA enzymes to potentially accommodate and hydrolyze larger antibiotic substrates. This is consistent with X-ray data which shows that 3rd generation cephalosporins require additional space between the Ω and β5-β6 loops to accommodate bulky substituents in the 6' position. However, a larger active site may not be the only factor necessary to hydrolyze larger antibiotics. The G224D mutant also shows an increased lower active site volume relative

to both the WT and P227S, yet the mutant has been reported to hydrolyze almost all antibiotics less efficiently than WT OXA-24 (Leonard, unpublished data).

3. Active Site Dynamics

The active site is affected by mutations in the β5-β6 loop, despite having the majority of the catalytic residues located ~10 Å from the mutations. The M223A mutation appears to have the greatest impact on the dynamics of the active site. The RMSD drift of the PASTFK, SxV, KSG motif, and Arg261in the M223A mutant show the greatest increases over the WT. Conversely, the G224D mutation shows the least effects on the dynamics of the PASTFK motif. The Cα drift of the motif in the G224D mutant shows a decrease relative to the WT, while M223A and P227S are greater and similar, respectively. The average position of the α3 helix bearing the PASTFK motif in the G224D mutant is also the most similar to the WT.

All the available crystal structures show that the carboxylated lysine (KCX) has a strong preference to interact with Trp167. In our trajectories, however, the network of hydrogen bonds shifts and KCX bonds to Lys218- while maintaining the hydrogen bond with Ser81. The WT enzyme shows the most frequent occurrence of this hydrogen bond, with the G224D mutant being the 2nd most frequent, followed by the M223A mutant, and the P227S mutant with the KCX-Lys bond forming less frequently. This rearrangement of the hydrogen bond network within the active site has not been observed in crystal structures. It is unknown whether this interaction is indeed formed in solution, but it could potentially affect the carboxylation state of the general base. The environment required to encourage carboxylation in OXA-10 is dependent on Trp154 (homologous to

Trp167 in OXA-24) (Baurin 2009) and also on Val130 (Buchman 2012). The movement of the KCX towards the lysine in the family K[TS]G motif may promote decarboxylation if the distance is too great for the carboxyl group to interact with the hydrophobic tryptophan. We cannot directly observe the decarboxylation process in the MD simulations, so it is not clear what effect(s) the KCX84-Lys218 hydrogen bond would have.

4. Loop Dynamics

All three mutations generally result in increased Ω loop flexibility (apart from Val169 in the G224D mutant), and P loop flexibility. The M223A mutant is the only enzyme in which some regions of the P loop have decreased flexibility. The P loop also moves away from the β5-β6 loop consistently across all 3 mutants. The Tyr112Cα-Met223Cα distance in the WT, M223A, G224D and P227S enzymes are 15.0 ±1.6 Å, 18.2 ±1.3 Å, 15.9 ±1.9 Å, 16.2 ±1.4 Å respectively.

Surprisingly, all three 3 mutations in the β5-β6 loop mutations result in decreased flexibility of the loop. All 3 loops with mutations show not only decreased RMSF values, but the residue on the loop with the lowest flexibility remains relatively the same: both Gly/Asp224 and Val225 have the lowest flexibility across all 3 mutants. This is interesting when considering that mutations on either end of the β5-β6 loop affect the fluctuations around the same region of the loop. β5-β6 loop flexibility and conformational states have been studied in detail for the P227S mutant and the results are described in subsection 5.

Decreased β5-β6 fluctuations appear to correlate with increased P and Ω loop fluctuations across the mutants in this study. This is an important observation but a more extensive study would be necessary to show the motional correlation between the three functional loops. The G224D mutation is common amongst the OXA-24 subgroup; it appears in OXA-72, OXA-143 (Higgins 2009), OXA-182 (Kim 2010), OXA-253 (Girlich 2014), and OXA-255 (Zander 2014). It is possible that this mutation results in the same dynamic changes in each enzyme, though it is unknown how other β5-β6 mutations (T226S in OXA-182, T226I in OXA-253) will affect the enzyme's dynamics in combination with the G224D mutation. In addition, longer simulation times are needed to sample the proteins' loop conformations sufficiently in general, and the lone P loop in particular.

5. Thermostability of G224D Mutant

Based on our trajectories, we were not able to explain the reasons for the increased thermostability of the G224D mutant. While the differences in R_{gyr} between WT and G224D are statistically significant ($p < 2.2x10^{-16}$), the increased R_{gyr} of G224D does not indicate a more thermostable enzyme. It is likely that calculating solvent accessible area (via Generalized Born/Surface Area model) would be a more appropriate method. Another stability factor would be the introduction of hydrogen bonds, which has caused increased thermostability in other enzymes (Zhang 2007). But Asp224 does not form any hydrogen bonds with the protein throughout the entire trajectory. While the backbone nitrogen atoms present on the Ω loop could be possible donors, the presence of Leu168 and Val169 makes Asp224's side chain rotation toward the Ω loop unfavorable. We also considered decreased flexibility as a contributor to thermostability; many

thermostable enzymes, or enzymes found in thermophilic organisms are less flexible than enzymes found in non-thermophiles (Vihinen 1987). The G224D enzyme indeed shows decreased flexibility relative to the WT in the β5-β6 loop, and, uniquely, Val169 on the Ω loop. However, it also has the greatest number of residues with increased fluctuations relative to the WT when compared to M223A and P227S. Therefore, based on our current trajectory data we are unable to explain the phenomenon, and the increased thermostability of the G224D mutant remains an open question.

6. Effects of Ser227-Glu251 Hydrogen Bond

The substitution of proline by serine introduces not only an increased conformational freedrom for the C-terminus of the loop, but also a new hydrogen bond center. The formation of the Ser227-Glu251 hydrogen bond rearranges the hydrogen bond network around the site of the mutation, resulting in Lys253, Arg72, and Gln52 interacting less with Glu251. The hydrogen bond also affects the conformations of the β5-β6 loop. The P227S mutant's β5- β6 loop occupies two main conformational clusters. These two distinct clusters show less variability than those of WT OXA-24. The RMSD range of the conformations in the P227S mutant span about 0.3-3.1 Å, whereas the WT spans 0.3-4.6 Å. The Tyr112-Met223 hydrophobic bridge is also wider in the majority of these conformations, likely helping accommodate larger antibiotic substrates into the active site. Thus, in the case of the P227S mutant, the decreased flexibility of the β5-β6 loop is likely caused by a new hydrogen bond, and a change in the conformational ensemble.

7. Concluding Remarks

The results in this work shed light on how the class D β-lactamases achieve substrate profile changes with single amino acid mutations. Our trajectories showed the conformational and dynamics changes caused by three specific mutations, each affecting the substrate selectivity of the enzyme. In particular, we proposed a mechanism through which the P227S mutant is able to expand its catalytic profile for 3rd generation cephalosporins through active site volume changes, and a shift in the conformational equilibrium of the β5-β6 loop.

The limitation of the work is the absence of the ligand. The binding of ligands can drastically affect a protein's conformation and function (Shaanan 1983; Fermi 1984), and simulations of an acyl-enzyme complex will illustrate more accurately how class D enzyme accommodate various antibiotics, and highlight associated changes in dynamics. Particularly, the question of the carboxylated lysine's variable hydrogen bond network will likely be resolved through simulations of an enzyme-substrate complex.

These enzymes will continue to evolve and adapt to the pressures of new and old drug therapies alike, But, understanding how mutations affect one subgroup can not only help our understanding of all class D enzymes, but it can save lives as well as further work will hopefully lead to the development of improved treatments for pathogens producing these enzymes.

Literature Cited

Afzal-shah, M., Woodford, N. & Livermore, D.M. (2001) Characterization of OXA-25, OXA-26, and OXA-27, Molecular Class D β -Lactamases Associated with Carbapenem Resistance in Clinical Isolates of Acinetobacter Baumannii. *Antimicrobial Agents and Chemotherapy* **45**: 583–588.

Albrich, W. C., Monnet, D. L., & Harbarth, S. (2004) Antibiotic Selection Pressure and Resistance in *Streptococcus pneumoniae* and *Streptococcus pyogenes*. *Emerging Infectious Diseases* **10**: 514-517.

Ambler, R.P. (1980) The structure of β-lactamases. *Philosophical Transactions of the Royal Society B* **289**: 321-331.

Arunan, E., Desiraju, G.R., Klein, R.A., Sadlej, J., Scheiner, S., Alkorta, I., Clary, D.C., Crabtree, R.H., Dannenberg, J.J., Hobza, P., Kjaergaard, H.G., Legon, A.C., Mennucci, B., & Nesbitt, D.J. (2011) Definition of the hydrogen bond (IUPAC Recommendations 2011). *Pure & Applied Chemistry* **83**: 1637-1641.

Barber, C.B., Dobkin, D.P., & Huhdanpaa, H. (1996) The quickhull algorithm for convex hulls. *ACM Transactions on Mathematical Software* **22**: 469-483.

Baurin, S., Vercheval, L., Bouillenne, F., Falzone, C., Brans, A., Jacquamet, L., Ferrer, J., Sauvage, E., Dehareng, D., Frère, J., Charlier, P., Galleni, M., & Kerff, F. (2009) Critical Role of Tryptophan 154 for the Activity and Stability of Class D *β*-Lactamases. *Biochemistry* **48**: 11252-11263.

Bax, R., Bywater, R., Cornaglia, G., Goossens, H., Hunter, P., Isham, V., Jarlier, V., Jones, R., Phillips, I., Sahm, D., Senn, S., Struelens, M., Taylor, D. & White, A. (2001) Surveillance of antimicrobial resistance - what , how and whither? *Clinical Microbiology and Infection* **7**: 316–325.

Bonnin, R.A., Ocampo-Sosa, A.A., Poirel, L., Guet-Revillet, H., & Nordmann, P. (2012) Biochemical and Genetic Characterization of Carbapenem-Hydrolyzing β-Lactamase OXA-229 from *Acinetobacter bereziniae*. *Antimicrobial Agents and Chemotherapy* **56**: 3923-3927.

Bou, G., Oliver, A., Martínez-beltrán, J., Bou, N. & Marti, S. (2000) OXA-24, a Novel Class D β -Lactamase with Carbapenemase Activity in an *Acinetobacter baumannii* Clinical Strain. *Antimicrobial Agents and Chemotherapy* **44**: 1556–1561.

Boyle-Vavra, S., & Daum, R. S. (2007) Community-acquired methicillin-resistant Staphylococcus aureus: the role of Panton-Valentine leukocidin. *Laboratory Investigation* **87**: 3-9.

Bozdogan, B., Esel, D., Whitener, C., Browne, F. A., & Appelbaum, P. C. (2003) Antibacterial susceptibility of a vancomycin-resistant Staphylococcus aureus strain isolated at the Hershey Medical Center. *Journal of Antimicrobial Chemotherapy* **52**: 864-868.

Bradford, P.A. (2001) Extended-Spectrum *β*-Lactamases in the 21st Century: Characterization, Epidemiology, and Detection of This Important Resistance Threat. *Clinical Microbiology Reviews* **14**: 933-951.

Brooks, B.R., Brooks III, C.L., Mackerell, A.D., Nilsson, L., Petrella, R.J., Roux, B., Won, Y., Archontis, G., Bartels, C., Boresch, S., Caflisch, A., Caves, L., Cui, Q., Dinner, A.R., Feig, M., Fischer, S., Gao, J., Hodoscek, M., Im, W., Kuczera, K., Lazaridis, T., Ma, J., Ovchinnikov, V., Paci, E., Pastor, R.W., Post, C.B., Pu, J.Z., Schaefer, M., Tidor, B., Venable, R.M., Woodcock, H.L., Wu, X., Yang, W., York, D.M., and Karplus, M. (2009) CHARMM: The Biomolecular Simulation Program. *Journal of Computational Chemistry* **30**: 1545-1615.

Buchman, J.S., Schneider, K.D., Lloyd, A.R., Pavlish, S.L., & Leonard, D.A. (2012) Site-Saturation Mutagenesis of Position V117 in OXA-1 *β*-Lactamase: Effects of Side Chain Polarity on Enzyme Carboxylation and Substrate Turnover. *Biochemistry* **51**: 3143-3150.

Bush, K. (1989) Characterization of β-Lactamases. *Antimicrobial Agents and Chemotherapy* **33**: 259-263.

Bush, K. & Jacoby, G. A. (2010) Updated functional classification of beta-lactamases. *Antimicrobial Agents and Chemotherapy* **54**: 969–976.

Bush, K., Courvalin, P., Dantas, G., Davies, J., Eisenstein, B., Huovinen, P., Jacoby, G.A., Kishany, R., Kreiswirth, B.N., Kutter, E., Lerner, S.A., Levy, S., Lewis, K., Lomovskaya, O., Miller, J.H., Mobashery, S., Piddock, L.J.V., Projan, S., Thomas, C.M., Tomasz, A., Tulkens, P.M., Walsh, T.R., Watson, J.D., Witkowski, J., Witte, W., Wright, G., Yeh, P., & Zgurskaya, H.I. (2011a) Tackling antibiotic resistance. *Nature Reviews Microbiology* **9**: 894-896.

Bush, K., & Fisher, J.F. (2011b) Epidemiological Expansion, Structural Studies, and Clinical Challenges of New β-Lactamases from Gram-Negative Bacteria. *Annual Review of Microbiology* **65**: 455-478.

Bush, K. (2013) Proliferation and significance of clinically relevant β-lactamases. *Annals of the New York Academy of Sciences* **1277**: 84-90.

Carrër, A., Poirel, L., Eraksoy, H., Cagatay, A., Badur, S. & Nordmann, P. (2008) Spread of OXA-48-positive carbapenem-resistant Klebsiella pneumoniae isolates in Istanbul, Turkey. *Antimicrobial Agents and Chemotherapy* **52**: 2950–2954.

Case, D.A., Cheatham III, T.E., Darden, T., Gohlke, H., Luo, R., Merz Jr, K.M., Onufriev, A., Simmerling, C., Wang, B., & Woods, R.J. (2005) The Amber Biomolecular Simulation Programs. *Journal of Computational Chemistry* **26**: 1668-1688.

Centers for Disease Control and Prevention (CDC). (2004) Acinetobacter baumannii Infections Among Patients at Military Medical Facilities Treating Injured U.S. Service Members, 2002--2004. *Morbidity and Mortality Weekly Report* **53**: 1063-1066.

Centers for Disease Control and Prevention (CDC). (2013) http://www.cdc.gov/drugresistance/threat-report-2013/pdf/ar-threats-2013-508.pdf

Che, T., Bonomo, R.A., Shanmugam, S., Bethel, C.R., Pustazi-Carey, M., Buynak, J.D., & Carey, P.R. (2012) Carboxylation and Decarboxylation of Active Site Lys 84

Controls the Activity of OXA-24 *β*-Lactamase of *Acinetobacter baumannii*: Raman Crystallographic and Solution Evidence. *Journal of the American Chemical Society* **134**: 11206-11215.

Cornaglia, G. & Rossolini, G.M. (2010) The emerging threat of acquired carbapenemases in Gram-negative bacteria. *Clinical Microbiology and Infection* **16**: 99–101.

Crichlow, G.V., Kuzin, A.P., Nukaga, M., Mayama, K., Sawai, T., & Knox, J.R. (1999) Structure of the Extended-Spectrum Class C β-Lactamase of *Enterobacter cloacae* GC1, a Natural Mutant with a Tandem Tripeptide Insertion. *Biochemistry* **38**: 10256-10261.

D'Andrea, M.M., Giani, T., D'Arezzo, S., Capone, A., Petrosillo, N., Visca, P., Luzzaro, F., & Rossolini, G.M. (2009) Characterization of pABVA01, a Plasmid Encoding the OXA-24 Carbapenemase from Italian Isolates of *Acinetobacter baumannii*. *Antimicrobial Agents and Chemotherapy* **53**: 3528–3533.

Da Silva, G.J., Quinteira, S., Bértolo, E., Sousa, J.C., Gallego, L., Duarte, A., & Peixe, L. (2004) Long-term dissemination of an OXA-40 carbapenemase-producing *Acinetobacter baumannii* clone in the Iberian Peninsula. *The Journal of Antimicrobial Chemotherapy* **54**: 255–258.

De Luca, F., Benvenuti, M., Carboni, F., Pozzi, C., Rossolini, G.M., Mangani, S., & Docquier, J.-D. (2011) Evolution to carbapenem-hydrolyzing activity in noncarbapenemase class D β-lactamase OXA-10 by rational protein design. *PNAS* **108**: 18424–18429.

Do, C.B., Mahabhashyam, M.S., Brudno, M., & Batzoglou, S. (2005) ProbCons: probabilistic consistency-based multiple sequence alignment. *Genome Research* **15**: 330-340.

Docquier, J.D., Benvenuti, M., Calderone, V., Giuliani, F., Kapetis, D., De Luca, F., Rossolini, G.M., & Mangani, S. (2010) Crystal Structure of the Narrow-Spectrum OXA-46 Class D β-Lactamase: Relationship between Active-Site Carbamylation and Inhibition by Polycarboxylates. *Antimicrobial Agents and Chemotherapy* **54**: 2167-2174.

Docquier, J.D., Calderone, V., De Luca, F., Benvenuti, M., Giuliani, F., Bellucci, L., Tafi, A., Nordmann, P., Botta, M., Rossolini, G.M., & Mangani, S. (2009) Crystal Structure of the OXA-48 β-Lactamase Reveals Mechanistic Diversity among Class D Carbapenemases. *Chemistry & Biology* **16**: 540–547.

Dror, R.O., Dirks, R.M., Grossman, J.P., Xu, H., & Shaw, D.E. (2012) Biomolecular Simulation: A Computational Microscope for Molecular Biology. *Annual Review of Biophysics* **41**: 429-452.

Dyer, K.M., Perkyns, J.S., Stell, G., & Pettitt, B.M. (2009) Site-renormalised molecular fluid theory: on the utility of a two-site model of water. *Molecular Physics* **107**: 423-431.

Edgar, R.C. (2004) MUSCLE: multiple sequence alignment with high accuracy and high throughput. *Nucleic Acids Research* **32**: 1792-1797.

Elander, R.P. (2003) Industrial production of β-lactam antibiotics. *Applied Microbiology and Biotechnology* **61**: 385–392.

Feig, M., Karanicolas, J. & Brooks, C.L. (2004) MMTSB Tool Set: enhanced sampling and multiscale modeling methods for applications in structural biology. *Journal of Molecular Graphics & Modelling* **22**: 377–395.

Ferech, M., Coenen, S., Malhotra-Kumar, S., Dvorakova, K., Hendrickx, E., Suetens, C. & Goossens, H. (2006) European Surveillance of Antimicrobial Consumption (ESAC): outpatient antibiotic use in Europe. *The Journal of Antimicrobial Chemotherapy* **58**: 401–407.

Fermi, G., Perutz, M.F., & Shaanan, B. (1984) The Crystal Structure of Human Deoxyhemoglobin at 1.74 Å Resolution. *Journal of Molecular Biology* **175**: 159-174.

Girlich, D., Damaceno, Q.S., Oliveira, A.C., & Nordmann, P. (2014) OXA-253, a Variant of the Carbapenem-Hydrolyzing Class D β-Lactamase OXA-143 in *Acinetobacter baumannii*. *Antimicrobial Agents and Chemotherapy* **58**: 2976-2978.

Golemi, D., Maveyraud, L., Vakulenko, S., Samama, J.P. & Mobashery, S. (2001) Critical involvement of a carbamylated lysine in catalytic function of class D β-lactamases. *PNAS* **98**: 14280–14285.

Grill, M.F., & Magnati, R.K. (2011) Neurotoxic effects associated with antibiotic use: management considerations. *British Journal of Clinical Pharmacology* **72**: 381-393.

Guitérrez, O., Juan, C., Cercenado, E., Navarro, F., Bouza, E., Coll, P., Perez, J.L., & Oliver, A. (2007) Molecular Epidemiology and Mechanisms of Carbapenem Resistance in *Pseudomonas aeruginosa* Isolates from Spanish Hospitals. *Antimicrobial Agents and Chemotherapy* **51**: 4329-4335.

Hall, G. (1994) The Evolution of Antibiotic Resistance: A Modern Catastrophe. *Bios* **65**: 133–138.

Hall, B.G. & Barlow, M. (2004) Evolution of the serine β-lactamases: past, present and future. *Drug Resistance Updates* **7**: 111–123.

Hall, B.G., & Barlow, M. (2005) Revised Ambler classification of β-lactamases. *Journal of Antimicrobial Chemotherapy* **55**: 1050-1051.

Higgins, P.G., Poirel, L., Lehmann, M., Nordmann, P., & Seifert, H. (2009) OXA-143, a Novel Carbapenem-Hydrolyzing Class D β-Lactamase in *Acinetobacter baumannii*. *Antimicrobial Agents and Chemotherapy* **53**: 5035-5038.

Humphrey, W., Dalke, A., & Schulten, K. (1996) VMD: Visual Molecular Dynamics. *Journal of Molecular Graphics* **14**: 33-38.

Jones, G., Willett, P., Glen, R.C., Leach, A.R., & Taylor, R. (1997) Development and Validation of a Genetic Algorithm for Flexible Docking. *Journal of Molecular Biology* **267**: 727-748.

Jorgensen, W.L., Chandrasekhar, J., Madura, J.D., Impey, R.W., & Klein, M.L. (1983) Comparison of simple potential functions for simulating liquid water. *The Journal of Chemical Physics* **79**: 926-935.

Kaitany, K.J., Klinger, N.V., June, C.M., Ramey, M.E., Bonomo, R.A., Powers, R.A., & Leonard, D.A. (2013) Structures of the Class D Carbapenemases OXA-23 and OXA-146: Mechanistic Basis of Activity against Carbapenems, Extended-Spectrum Cephalosporins, and Aztreonam. *Antimicrobial Agents and Chemotherapy* **57**: 4848-4855.

Kalil, A.C., Murthy, M.H., Hermsen, E.D., Neto, F.K., Sun, J., & Rupp, M.E. (2010) Linezolid versus vancomycin or teicoplanin for nosocomial pneumonia: A systematic review and meta-analysis. *Critical Care Medicine* **38**: 1802-1808.

Katayama, Y., Zhang, H., & Chamber, H.F. (2004) PBP 2a Mutations Producing Very-High-Level Resistance to Beta-Lactams. *Antimicrobial Agents and Chemotherapy* **48**: 453-459.

Katoh, K., Kuma, K., Toh, H., & Miyata, T. (2005) MAFFT version 5: improvement in accuracy of multiple sequence alignment. *Nucleic Acids Research* **33**: 511-518.

Karplus, M., & McCammon, J.A. (2002) Molecular dynamics simulations of biomolecules. *Nature Structural Biology* **9**: 646-652.

Keam, S.J. (2008) Doripenem: A Review of its Use in the Treatment of Bacterial Infections. *Drugs* **68**: 2021–2057.

Kelly, J.A., Dideberg, O., Charlier, P., Wery, J.P., Libert, M., Moews, P.C., Knox, J.R., Duez, C., Fraipont, C. & Joris, B. (1986) On the Origin of Bacterial Resistance to Penicillin: Comparison of a β-Lactamase and a Penicillin Target. *Science* **231**: 1429–1431.

Kim, C., Lee, Y., Lee, H., Woo, G., Song, W., Kim, M., Lee, W., Jeong, S.H., Lee, K., & Chong, Y. (2010) Prevalence and diversity of carbapenemases among imipenem-nonsesceptible *Acinetobacter* isolates in Korea: emergence of a novel OXA-182. *Diagnostic Microbiology & Infectious Disease* **68**: 432-438.

Kirby, W. M. (1944) Extraction of a Highly Potent Penicillin Inactivator from Penicillin Resistant Staphylococci. *Science* **99**: 452-453.

Ledent, P., Raquet, X., Joris, B., Van Beeumen, J. & Frère, J.M. (1993) A comparative study of class-D β-lactamases. *The Biochemical Journal* **292**: 555–562.

Lee, C., Grasso, C., & Sharlow, M.F. (2002) Multiple sequence alignment using partial order graphs. *Bioinformatics* **18**: 452-464.

Li, X., & Nikaido, H. (2009) Efflux-Mediated Drug Resistance in Bacteria: an Update. *Drugs* **69**: 1555-1623.

MacKerell Jr, A.D., Bashford, D., Bellot, M., Dunbrack Jr, R.L., Evanseck, J.D., Field, M.J., Fischer, S., Gao, J., Guo, H., Ha, S., Joseph-McCarthy, D., Kuchnir, L., Kuczera, K., Lau, F.T.K., Mattos, C., Michnick, S., Ngo, T., Nguyen, D.T., Prodhom, B., Reiher III, W.E., Roux, B., Schlenkrich, M., Smith, J.C., Stote, R., Straub, J., Watanabe, M., Wiórkiewicz-Kuczera, J., Yin, D., & Karplus, M. (1998) All-Atom Empirical Potential for Molecular Modeling and Dynamics Studies of Proteins. *The Journal of Physical Chemistry B* **102**: 3586-3616.

MacKerell Jr, A.D., Feig, M., & Brooks III, C.L. (2004) Extending the treatment of backbone energetics in protein force fields: Limitations of gas-phase quantum

mechanics in reproducing protein conformational distributions in molecular dynamics simulations. *Journal of Computational Chemistry* **25**: 1400-1415.

Mahoney, M.W., & Jorgensen, W.L. (2000) A five-site model for liquid water and the reproduction of the density anomaly by rigid, nonpolarizable potential functions. *Journal of Chemical Physics* **112**: 8910-8922.

Massova, I. & Mobashery, S. (1998) Kinship and Diversification of Bacterial Penicillin-Binding Proteins and β-Lactamases. *Antimicrobial Agents and Chemotherapy* **42**: 1–17.

Matagne, A., Lamotte-Brasseur, J., & Frère, J.-M. (1998) Catalytic properties of class A β-lactamases: efficiency and diversity. *Biochemical Journal* **330**: 581-598.

Medeiros, A.A. (1997) Evolution and Dissemination of β-lactamases Accelerated by Generations of β-lactam Antibiotics. *Clinical Infectious Diseases* **24**: S19–S45.

Mitchell, J.M., Clasman, J.R., June, C.M., Kaitany, K.J., LaFleur, J.R., Taracila, M.A., Klinger, N.V., Bonomo, R.A., Wymore, T., Szarecka, A., Powers, R.A., & Leonard, D.A. (2015) Structural Basis of Activity against Aztreonam and Extended spectrum Cephalosporins for Two Carbapenem-Hydrolyzing Class D β-Lactamases from *Acinetobacter baumannii*. *Biochemistry* **54**: 1976-1987.

Montealegre, M.C., Maya, J.J., Correa, A., Espinal, P., Mojica, M.F., Ruiz, S.J., Rosso, F., Vila, J., Quinn, J.P., & Villegas, M.V. (2012) First Identification of OXA-72 Carbapenemase from *Acinetobacter pittii* in Colombia. *Antimicrobial Agents and Chemotherapy* **56**: 3996–3998.

Moretti, S., Armougom, F., Wallace, I.M., Higgins, D.M., Jongeneel, C.V., & Notredame, C. (2007) The M-Coffee web server: a meta-method for computing multiple sequence alignments by combining alternative alignment methods. *Nucleic Acids Research* **35**: W645-W648.

Morris, G.M., Huey, R., Lindstrom, W., Sanner, M.F., Belew, R.K., Goodsell, D.S., & Olson, A.J. (2009) AutoDock4 and AutoDockTools4: Automated Docking with Selective Receptor Flexibility. *Journal of Computational Chemistry* **30**: 2785-2791.

Nakae, T., Nakajima, A., Ono, T., Saito, K., & Yoneyama, H. (1999) Resistance to β-Lactam Antibiotics in *Pseudomonas aeruginosa* Due to Interplay between the MexAB-OprM Efflux Pump and β-Lactamase. *Antimicrobial Agents and Chemotherapy* **43**: 1301-1303.

Neu, H.C. (1992) The Crisis in Antibiotic Resistance. *Science* **257**: 1064–1073.

Notredame, C., Higgins, D.G., & Heringa, J. (2000) T-Coffee: A novel method for fast and accurate multiple sequence alignment. *Journal of Molecular Biology* **302**: 205-217.

Nukaga, M., Mayama, K., Hujer, A.M., Bonomo, R.A., & Knox, J.R. (2003) Ultrahigh Resolution Structure of a Class A β-Lactamase: On the Mechanism and Specificity of the Extended-spectrum SHV-2 Enzyme. *Journal of Molecular Biology* **328**: 289-301.

Paetzel, M., Danel, F., de Castro, L., Mosimann, S.C., Page, M.G.P., & Strynadka, N.C.J. (2000) Crystal Structure of the Class D β-lactamase OXA-10. *Nature Structural Biology* **7**: 918-925.

Paterson, D.L. & Bonomo, R.A. (2005) Extended-Spectrum β-Lactamases: A Clinical Update. *Clinical Microbiology Reviews* **18**: 657-686.

Pei, J., Sadreyev, R., & Grishin, N.V. (2003) PCMA: fast and accurate multiple sequence alignment based on profile consistency. *Bioinformatics* **19**: 427-428.

Pernot, L., Frénois, F., Rybkine, T., L'Hermite, G., Petrella, S., Delettré, J., Jarlier, V., Collatz, E., & Sougakoff, W. (2001) Crystal Structure of the class D β-lactamase OXA-13 in the native form and in complex with meropenem. *Journal of Molecular Biology* **310**: 859-874.

Poirel, L. & Nordmann, P. (2006) Carbapenem resistance in *Acinetobacter baumannii*: mechanisms and epidemiology. *Clinical Microbiology and Infection* **12**: 826–836.

Poirel, L., Naas, T., & Nordmann, P. (2010) Diversity, Epidemiology, and Genetics of Class D β-Lactamases. *Antimicrobial Agents and Chemotherapy* **54**: 24-38.

Poirel, L., Castanheira, M., Carrër, A., Rodriguez, C.P., Jones, R.N., Smayevsky, J., & Nordmann, P. (2011) OXA-163, an OXA-48-Related Class D β-Lactamase with Extended Activity Toward Expanded-Spectrum Cephalosporins. *Antimicrobial Agents and Chemotherapy* **55**: 2546-2551.

Povilonis, J., Seputiene, V., Krasauskas, R., Juskaite, R., Miskinyte, M., Suziedelis, K., & Suziedeliene, E. (2012) Spread of carbapenem-resistant *Acinetobacter baumannii*

carrying a plasmid with two genes encoding OXA-72 carbapenemase in Lithuanian hospitals. *Journal of Antimicrobial Chemotherapy* **68**: 1000-1006.

Queenan, A.M. & Bush, K. (2007) Carbapenemases: the Versatile β-Lactamases. *Clinical Microbiology Reviews* **20**: 440–458.

Quinteira, S., Grosso, F., Ramos, H., & Peixe, L. (2007) Molecular Epidemiology of Imipenem-Resistant *Acinetobacter haemolyticus* and *Acinetobacter baumannii* Isolates Carrying Plasmid-Mediated OXA-40 from a Portuguese Hospital. *Antimicrobial Agents and Chemotherapy* **51**: 3465–3466.

Rarey, M., Kramer, B., Lengauer, T., & Klebe, G. (1996) A Fast Flexible Docking Method using an Incremental Construction Algorithm. *Journal of Molecular Biology* **261**: 470-489.

Roberts, R.R., Hota, B., Ahmad, I., Scott II, D., Foster, S.D., Abbasi, F., Schabowski, S., Kampe, L.M., Ciavarella, G.G., Supino, M., Naples, J., Cordell, R., Levy, S.B., & Weinstein, R.A. (2009) Hospital and Societal Costs of Antimicrobial-Resistant Infections in a Chicago Teaching Hospital: Implications for Antibiotic Stewardship. *Clinical Infectious Diseases* **49**: 1175-1184.

Rumbo, C., Fernández-Moreira, E., Merino, M., Poza, M., Mendez, J.A., Soares, N.C., Mosquera, A., Chaves, F. & Bou, G. (2011) Horizontal Transfer of the OXA-24 Carbapenemase Gene via Outer Membrane Vesicles: a New Mechanism of Dissemination of Carbapenem Resistance Genes in *Acinetobacter baumannii*. *Antimicrobial Agents and Chemotherapy* **55**: 3084–3090.

Salkind, A.R., Cuddy, P.C. & Foxworth, J.W. (2001) Is This Patient Allergic to Penicillin? An Evidence-Based Analysis of the Likelihood of Penicillin Allergy. *The Journal of the American Medical Association* **285**: 2498–2505.

Santillana, E., Beceiro, A., Bou, G., & Romero, A. (2007) Crystal structure of the carbapenemase OXA-24 reveals insights into the mechanism of carbapenem hydrolysis. *PNAS* **104**: 5354-5359.

Schneider, K.D., Karpen, M.E., Bonomo, R.A, Leonard, D.A., & Powers, R.A. (2009a) The 1.4 Å Crystal Structure of the Class D β-lactamase OXA-1 Complexed with Doripenem. *Biochemistry* **48**: 11840–11847.

Schneider, K.D., Bethel, C.R., Distler, A.M., Hujer, A.M., Bonomo, R. A. & Leonard, D.A. (2009b) Mutation of the Active Site Carboxy-Lysine (K70) of OXA-1 β-Lactamase Results in a Deacylation-Deficient Enzyme. *Biochemistry* **48**: 6136–6145.

Schneider, K.D., Ortega, C.J., Renck, N.A., Bonomo, R.A., Powers, R.A., & Leonard, D.A. (2011) Structures of the Class D Carbapenemase OXA-24 from *Acinetobacter baumannii* in Complex with Doripenem. *Journal of Molecular Biology* **406**: 583–594.

Shaanan, B. (1983) Structure of Human Oxyhemoglobin at 2.1 Å Resolution. *Journal of Molecular Biology* **171**: 31-59.

Sharma, A. (2011) Antimicrobial resistance: No action today, no cure tomorrow. *Indian Journal of Medical Microbiology* **29**: 92-92.

Singh, U.C., & Kollman, P.A. (1984) An approach to computing electrostatic charges for molecules. *Journal of Computational Chemistry* **5**: 129-145.

Smith, C.A., Antunes, N.T., Toth, M., & Vakulenko, S.B. (2014) Crystal Structure of the Carbapenemase OXA-58 from *Acinetobacter baumannii*. *Antimicrobial Agents and Chemotherapy* **58**: 2135-2143.

Subramanian, A.R., Weyer-Menkhoff, J., Kaufmann, M., & Morgenstern, B. (2005) DIALIGN-T: An improved algorithm for segment-based multiple sequence alignment. *BMC Bioinformatics* **6**: 66.

Sun, T., Nukaga, M., Mayama, K., Braswell, E.H., & Knox, J.R. (2003) Comparison of β-lactamases of classes A and D: 1.5-Å crystallographic structure of the class D OXA-1 oxacillinase. *Protein Science* **12**: 82-91.

Szarecka, A., Lesnock, K.R., Ramirez-Mondragon, C.A., Nicholas Jr, H.B., & Wymore, T. (2011) The Class D β-lactamase family: residues governing the maintenance and diversity of function. *Protein Engineering, Design & Selection* **24**: 801-809.

Talaro, K. P., & Chess, B. (2011) Foundations in Microbiology 8th Edition. McGraw-Hill Higher Education, New York, 937p.

Tan, C., Yang, L., & Luo, R. (2006) How Well Does Poisson-Boltzmann Implicit Solvent Agree with Explicit Solvent? A Quantitative Analysis. *The Journal of Physical Chemistry B* **110**: 18680-18687.

Thompson, J., Higgins, D., & Gibson, T. (1994) CLUSTAL W: improving the sensitivity of progressive multiple sequence alignment though sequence weighting, position-

specific gap penalties and weight matrix choice. *Nucleic Acids Research* **22**: 4673-4690.

Tian, G.-B., Adams-Haduch, J.M., Bogdanovich, T., Pasculle, A.W., Quinn, J.P., Wang, H.-N., & Doi, Y. (2011) Identification of Diverse OXA-40 group Carbapenemases, Including a Novel Variant, OXA-160, from *Acinetobacter baumannii* in Pennsylvania. *Antimicrobial Agents and Chemotherapy* **55**: 429-432.

Torshin, I.Y., Weber, I.T., & Harrison, R.W. (2002) Geometric criteria of hydrogen bonds in proteins and identification of 'bifurcated' hydrogen bonds. *Protein Engineering* **15**: 359-363.

Vihinen, M. (1987) Relationship of protein flexibility to thermostability. *Protein Engineering, Design & Selection* **1**: 477-480.

Wallace, I.M., O'Sullivan, O., Higgins, D.G., & Notredame, C. (2006) M-Coffee: combining multiple sequence alignment methods with T-Coffee. *Nucleic Acids Research* **34**: 1692-1699.

Wang, J., Wolf, R.M., Caldwell, J.W., Kollman, P.A., & Case, D.A. (2003) Development and Testing of a General Amber Force Field. *Journal of Computational Chemistry* **25**: 1157-1174.

Wang, H., Guo, P., Sun, H., Wang, H., Yang, Q., Chen, M., Xu, Y., & Zhu, Y. (2007) Molecular Epidemiology of Clinical Isolates of Carbapenem-Resistant

Acinetobacter spp. from Chinese Hospitals. *Antimicrobial Agents and Chemotherapy* **51**: 4022–4028.

Zander, E., Bonnin, R.A., Seifert, H., & Higgins, P.G. (2014) Characterization of $bla_{OXA-143}$ Variants in *Acinetobacter baumannii* and *Acinetobacter pittii*. *Antimicrobial Agents and Chemotherapy* **58**: 2704-2708.

Zeng, X., & Lin, J. (2013) Beta-lactamase induction and cell wall metabolism in Gram-negative bacteria. *Frontiers in Microbiology* **4**: doi: 10.3389/fmicb.2013.00128.

Zhanel, G.G., Wiebe, R., Dilay, L., Thomson, K., Rubinstein, E., Hoban, D.J., Noreddin, A.M., & Karlowsky, J. A. (2007) Comparative Review of the Carbapenems. *Drugs* **67**: 1027-1052.

Zhang, W., Mullaney, E.J., & Lei, X.G. (2007) Adopting Selected Hydrogen Bonding and Ionic Interactions From *Aspergillus fumigatus* Phytase Structure Improves the Thermostability of *Aspergillus niger* PhyA Phytase. *Applied and Environmental Microbiology* **73**: 3069-3076.

APPENDIX A

KCX TOPOLOGY AND PARAMETERS

The topology and force-field entries for the carboxylated lysine (Simakov and Wymore, unpublished data) are detailed as follows:

KCX CHARMM Topology

```
PRES   KCX    -1.00 ! Patch for carboxylated Lysine, ns
GROUP
ATOM CE   CT2     0.060
ATOM HE1  HA      0.090
ATOM HE2  HA      0.090
ATOM NZ   NECA   -0.810
ATOM HZ1  H       0.300
ATOM CX   CC      0.690
ATOM OQ1  OC     -0.710
ATOM OQ2  OC     -0.710
DELETE ATOM HZ2
DELETE ATOM HZ3
BOND NZ CX
BOND  CX OQ1
BOND CX OQ2
IMPR  CX NZ OQ1 OQ2
```

KCX CHARMM Force-field Parameters

Bond Parameters

CT2	NECA	380.00	1.4300
H	NECA	440.00	1.0280
CC	NECA	320.00	1.4617

Angle Parameters

CT3	CT2	NECA	67.70	110.93

CT2 CT2 NECA	67.70	110.93
HA CT2 NECA	51.50	107.50
CC NECA CT2	50.00	115.00
CT2 NECA H	60.00	110.00
CC NECA H	60.00	110.00
NECA CC OC	80.00	110.00

Torsional Parameters

HA CT2 CT3 HA	0.1600	3	0.00
HA CT3 CT2 NECA	0.0400	3	0.00
HA NECA CT2 CT3	1.1000	1	180.00
CC NECA CT2 CT3	0.2000	3	0.00
CC NECA CT2 CT2	1.1000	1	180.00
CC NECA CT2 CT2	0.2000	3	0.00
H NECA CT2 HA	0.0000	1	0.00
CC NECA CT2 HA	0.0000	1	0.00
CT2 NECA CC OC	2.2000	2	180.00
CT3 CT2 NECA H	0.2000	3	0.00
CT2 CT2 NECA H	0.2000	3	0.00

H	NECA	CC	OC	1.9250 2	180.00

Improper Parameters

CC	NECA	OC	OC	96.0000	0.0000

Non-bonded Parameters (L-J, ε, $R_{min}/2$)

NECA	0.000000	-0.200000	1.850000

APPENDIX B

TCL SCRIPTS

All syntax is presented in size 11 Courier New, single-spaced font. All scripts are inputted as directed into the VMD Tk Console unless otherwise specified. Location within the syntax where user-specified variables are defined are highlighted yellow.

Script 1: AnimateTRJs

```
    proc animatetrjs {start end fileformat} {
  set filename [format $fileformat [expr $start]]
  incr start
  puts "Reading initial frame in TRJ sequence $filename"
  mol load dcd $filename

  puts "Reading TRJ files as an animation..."
  for {set i $start} {$i <= $end} {incr i 1} {
    set filename [format $fileformat [expr $i]]
    animate read dcd $filename
  }
}
```

Use: To load .trj files consecutively into VMD. Copy and paste entire script into VMD TK console. Trajectory files must be located within the current directory.

User-specified variables: N/A

Example Input: `animatetrjs 5 50 "oxa24-wt-sys1-dyn%d.trj"`

The above example loads all frames from oxa24-wt-sys1-dyn5.trj through, and including, oxa24-wt-sys1-dyn50.trj.

Example Output: N/A

Script 2: Load every other frame:

```
proc eo_frame {start end fileformat} {
  set filename [format dcd [expr $start]]
  for {set i $start} {$i <=$end} {incr i 1} {
    set filename [format $fileformat [expr $i]]
    mol addfile $filename type dcd step 2
  }
}
```

Use: Similar to Script 1, except loads every other frame of the defined range of trajectory files.

User-specified variables: N/A

Example Input: `eo_frame 5 50 "oxa24-wt-sys1-dyn%d.trj"`

Example Output: N/A

Script 3: Whole protein Cα RMSF

```
set outfile [open filename.dat w]
set sel [atomselect top "protein and name CA"]
set rmsf "[measure rmsf $sel]"
for {set i 0} {$i < [$sel num]} {incr i} {
  puts $outfile "[expr {$i+1}] [lindex $rmsf $i]"
}
close $outfile
```

Use: Measures RMSF of all Cαs throughout the loaded frames, and prints the residue-RMSF data into a .dat file within the current directory. Script must be pasted, in its entirety, into the VMD Tk Console.

User-specified variables:

`outfile` → File to which all data will be outputted; named "filename.dat."

`sel` → Atomic selection for which RMSF will be calculated.

Example Input: N/A. Code runs automatically when copied and pasted into VMD Tk Console.

Example Output: Script outputs two columns in the user-specified file. The first column is the residue number, the second is the RMSF value in Å.

Example:

```
1   1.345243
2   1.190847
3   1.055538
4   0.868406
5   0.954798
```

Script 4: Radius of gyration

```
set mol [molinfo top]
set out [open filename.dat w]
set sel [atomselect top "protein and not hydrogen"]
for {set i 0} {$i <= 96000} {incr i} {
$sel frame $i
$sel update
puts $out "$i [measure rgyr $sel]"
}
close $out
```

Use: Measures the radius of gyration (not including hydrogens) throughout the loaded frames, and prints the frame-R_{gyr} data into a .dat file. The user must specify the filename to which the information is to be written [filename.dat]; and the number of frames loaded

User-specified variables:

`out` →The file to which R_{gyr} data will be outputted; named "filename.dat."

`sel` → Atomic selection for which R_{gyr} will be calculated.

Example Input: N/A. Code runs automatically when copied and pasted into VMD Tk Console.

Example Output:

1 17.70242
2 17.75708
3 17.78677
4 17.82501
5 17.84038

Script 5: Average Structure

```
set var [atomselect top "protein"]
set averagestructure [measure avpos $var]
set newvar [atomselect top "protein"]
$newvar set {x y z} $averagestructure
$newvar writepdb filename.pdb
```

Use: Determines the average structure from the loaded frames, and outputs a PDB file containing the corresponding coordinates. Script is run line by line in the VMD TK Console.

User-specified variables:

`var` →The selection to which average coordinates are to be determined. Selections are defined using standard VMD syntax.

`filename.pdb` → The filename to which the average coordinates will be outputted in PDB format; named "filename.pdb."

Example Input: N/A. Run code line by line in VMD TK Console.

Example Output: N/A. Output is a PDB file which can be opened normally in VMD.

Script 6: Heatmap Generator

```
#  Format the data into R matrices
row.names(matrix1) <- matrix1$Atom
row.names(matrix2) <- matrix2$Atom
matrix1_2 <- matrix1[,2:#1]
matrix2_2 <- matrix2[,2:#2]
m1dm <- data.matrix(matrix1_2)
m2dm <- data.matrix(matrix2_2)

# Create color palette
myPalette <- colorRampPalette(rev(brewer.pal(11, "Spectral")))

# Create Heatmaps
heatmap.2(MATRIX, Rowv=NA, Colv=NA, col=myPalette,
breaks=seq(0,20,by=0.1), symm=TRUE, trace="none",
dendrogram="none")
matrix1_heatmap <- levelplot(m1dm, col.regions=myPalette,
scales=list(x=list(rot=90)), ylab = "Y-Label", xlab="X-Label")
matrix2_heatmap <- levelplot(m2dm, col.regions=myPalette,
scales=list(x=list(rot=90)), ylab = "Y-Label", xlab="X-Label")
testmat <- m2dm - m1dm
diff_heatmap <- levelplot(testmat, col.regions=myPalette,
scales=list(x=list(rot=90)), ylab = "Y-Label", xlab="X-Label")
```

Use: Code produces heatmaps similar to Figs. 19-24. Requires the following packages: gplots, Lattice, RColorBrewer. Script written by Brian Mullen.

User-specified variables:

#1 → Input n-1 total matrix observations. In **Example Input**, wt2 had 76 total observations, so 76-1=75.

#2 → Input n-1 total matrix observations. In **Example Input**, p227s2 had 76 total observations, so 76-1=75.

Example Input:

```
View(`p227s_full`)
`p227s` <- read.csv("~/Downloads/p227s_VarDistanceMatrix.csv")
 View(`p227s`)
wt <- read.csv("~/Downloads/wt_VarDistanceMatrix.csv")
 View(wt)

#  Format the data into R matrices
row.names(wt) <- wt$Atom
row.names(p227s) <- p227s$Atom
wt2 <- wt[,2:75]
p227s2 <- p227s[,2:75]
wdm <- data.matrix(wt2)
pdm <- data.matrix(p227s2)

# Create color palette
myPalette <- colorRampPalette(rev(brewer.pal(11, "Spectral")))

# Create Heatmaps
wt_heatmap <- levelplot(wdm, col.regions=myPalette,
scales=list(x=list(rot=90)), ylab = "Y-Label", xlab="X-Label")
p227s_heatmap <- levelplot(pdm, col.regions=myPalette,
scales=list(x=list(rot=90)), ylab = "Y-Label", xlab="X-Label")
testmat <- pdm - wdm
diff_heatmap <- levelplot(testmat, col.regions=myPalette,
scales=list(x=list(rot=90)), ylab = "Y-Label", xlab="X-Label")
```

Example Output: See heatmaps in Figs. 19-24.

APPENDIX C

SUPPLEMENTARY DATA

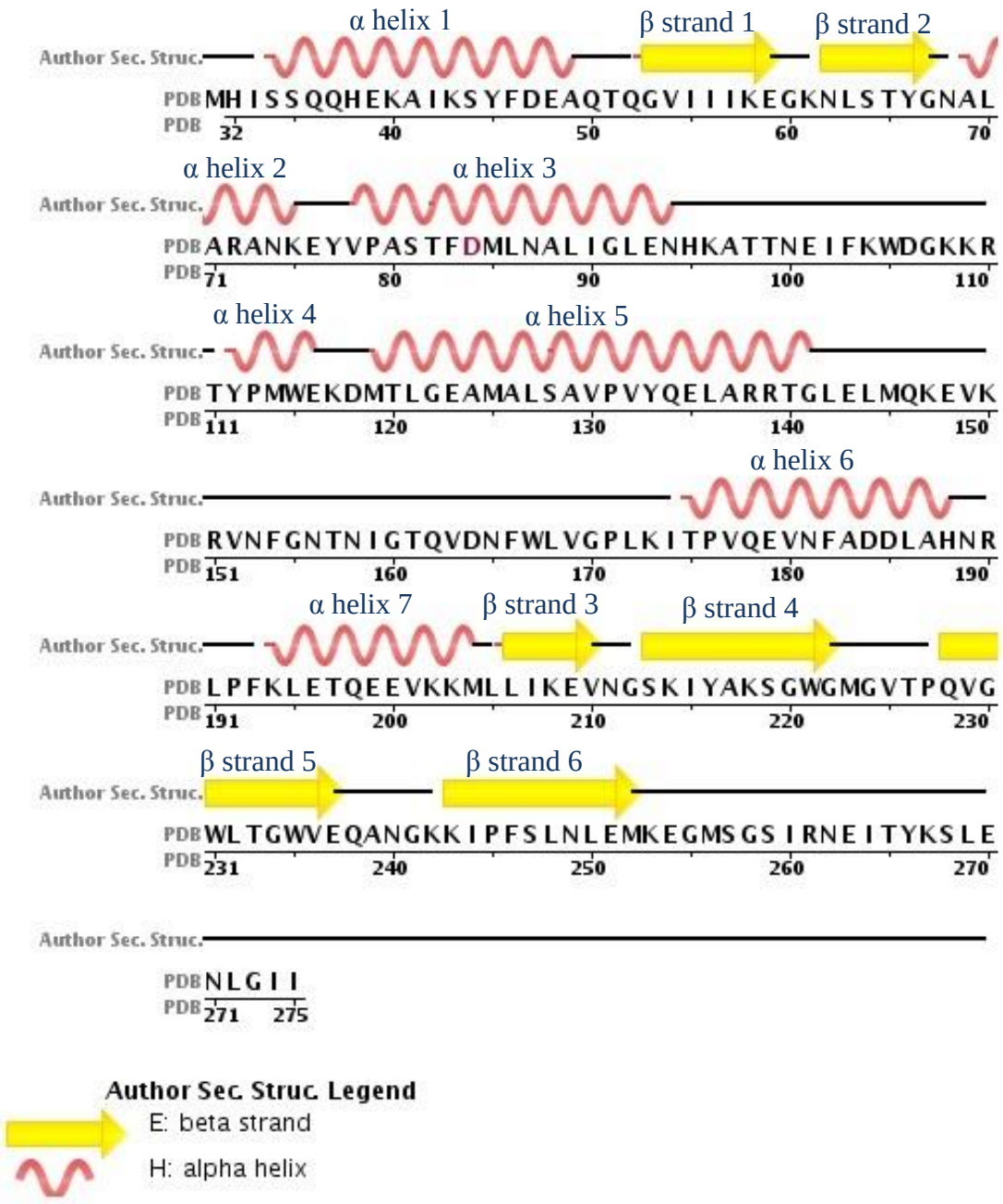

Fig. 36: Secondary Structure Diagram of OXA-24. Secondary structure was assigned by Schneider et al. (2011). WT OXA-24 contains a lysine in position 84, this structure has an introduced aspartate mutation to prevent substrate deacylation. PDB 3PAE.

	OXA-24	OXA-25	OXA-26	OXA-72	OXA-139	OXA-143	OXA-160	OXA-182	OXA-207	OXA-231	OXA-253	OXA-255
OXA-24	100	99	99	99	99	87	99	89	99	87	89	87
OXA-25	99	100	98	98	98	86	98	88	98	86	89	86
OXA-26	99	98	100	99	99	87	99	88	99	87	89	86
OXA-72	99	98	99	100	99	88	99	89	99	87	90	87
OXA-139	99	98	99	99	100	87	99	88	99	87	89	86
OXA-143	87	86	87	88	87	100	87	93	87	99	93	92
OXA-160	99	98	99	99	99	87	100	88	99	87	89	86
OXA-182	89	88	88	89	88	93	88	100	88	92	93	92
OXA-207	99	98	99	99	99	87	99	88	100	87	89	86
OXA-231	87	86	87	87	87	99	87	92	87	100	93	92
OXA-253	89	89	89	90	89	93	89	93	89	93	100	95
OXA-255	87	86	86	87	86	92	86	92	96	92	95	100

Table 14: Percent Identity Matrix of OXA-24 Subgroup.

WT	M223A	G224D	P227S	WT	M223A	G224D	P227S
VAL78CG2	VAL78CG2	VAL78CG2	VAL78CG2	GLY220N	GLY220N	GLY220N	GLY220N
ALA80CA	ALA80CA	ALA80CA	ALA80CA	GLY220CA	GLY220CA	GLY220CA	GLY220CA
ALA80CB	ALA80CB	ALA80CB	ALA80CB	GLY220C	GLY220C	GLY220C	GLY220C
ALA80C	ALA80C	ALA80C	ALA80C	GLY220O	GLY220O	GLY220O	GLY220O
SER81N	SER81N	SER81N	SER81N	TRP221N	TRP221N	TRP221N	TRP221N
SER81CA	SER81CA	SER81CA	SER81CA	TRP221CA	TRP221CA	TRP221CA	TRP221CA
SER81CB	SER81CB	SER81CB	SER81CB	TRP221CB	TRP221CB	TRP221CB	TRP221CB
SER81OG	SER81OG	SER81OG	SER81OG	TRP221CG	TRP221CG	TRP221CG	TRP221CG
LYS84CE	LYS84CE	LYS84CE	LYS84CE	TRP221CD1	TRP221CD1	TRP221CD1	TRP221CD1
LYS84NZ	LYS84NZ	LYS84NZ	LYS84NZ	TRP221CD2	TRP221CD2	TRP221CD2	TRP221CD2
LYS84CX	LYS84CX	LYS84CX	LYS84CX	TRP221CE3	TRP221CE3	TRP221CE3	TRP221CE3
LYS84OQ1	LYS84OQ1	LYS84OQ1	LYS84OQ1	TRP221C	TRP221C	TRP221C	TRP221C
LYS84OQ2	LYS84OQ2	LYS84OQ2	LYS84OQ2	TRP221O	TRP221O	TRP221O	TRP221O
TYR112CG	TYR112CG	TYR112CG	TYR112CG	GLY222CA	GLY222CA	GLY222CA	GLY222CA
TYR112CD1	TYR112CD1	TYR112CD1	TYR112CD1	GLY222C	GLY222C	GLY222C	GLY222C
TYR112CE1	TYR112CE1	TYR112CE1	TYR112CE1	GLY222O	GLY222O	GLY222O	GLY222O
TYR112CZ	TYR112CZ	TYR112CZ	TYR112CZ	MET223N		MET223N	MET223N
TYR112OH	TYR112OH	TYR112OH	TYR112OH	MET223CA		MET223CA	MET223CA
TYR112CD2	TYR112CD2	TYR112CD2	TYR112CD2	MET223CB		MET223CB	MET223CB
TYR112CE2	TYR112CE2	TYR112CE2	TYR112CE2	MET223CG		MET223CG	MET223CG
TRP115NE1	TRP115NE1	TRP115NE1	TRP115NE1	MET223SD		MET223SD	MET223SD
TRP115CE2	TRP115CE2	TRP115CE2	TRP115CE2	MET223CE		MET223CE	MET223CE
TRP115CZ3	TRP115CZ3	TRP115CZ3	TRP115CZ3	MET223C		MET223C	MET223C
TRP115CZ2	TRP115CZ2	TRP115CZ2	TRP115CZ2		ALA223N		
TRP115CH2	TRP115CH2	TRP115CH2	TRP115CH2		ALA223CA		
LEU127O	LEU127O	LEU127O	LEU127O		ALA223CB		
SER128CB	SER128CB	SER128CB	SER128CB		ALA223C		
SER128OG	SER128OG	SER128OG	SER128OG	GLY224N	GLY224N		GLY224N
SER128C	SER128C	SER128C	SER128C	GLY224CA	GLY224CA		GLY224CA
SER128O	SER128O	SER128O	SER128O	GLY224C	GLY224C		GLY224C
TRP167CD1	TRP167CD1	TRP167CD1	TRP167CD1			ASP224N	
TRP167NE1	TRP167NE1	TRP167NE1	TRP167NE1			ASP224CA	
LEU168CA	LEU168CA	LEU168CA	LEU168CA			ASP224CB	
LEU168CB	LEU168CB	LEU168CB	LEU168CB			ASP224CG	
LEU168CG	LEU168CG	LEU168CG	LEU168CG			ASP224OD1	
LEU168CD1	LEU168CD1	LEU168CD1	LEU168CD1			ASP224OD2	
LEU168CD2	LEU168CD2	LEU168CD2	LEU168CD2			ASP224C	
LEU168C	LEU168C	LEU168C	LEU168C	VAL225N	VAL225N	VAL225N	VAL225N
LEU168O	LEU168O	LEU168O	LEU168O	VAL225CG2	VAL225CG2	VAL225CG2	VAL225CG2
VAL169CG1	VAL169CG1	VAL169CG1	VAL169CG1	ARG261CZ	ARG261CZ	ARG261CZ	ARG261CZ
SER219CB	SER219CB	SER219CB	SER219CB	ARG261NH1	ARG261NH1	ARG261NH1	ARG261NH1
SER219OG	SER219OG	SER219OG	SER219OG	ARG261NH2	ARG261NH2	ARG261NH2	ARG261NH2
SER219O	SER219O	SER219O	SER219O				

Table 15: Atomic Selection of Active Site. Atoms highlighted in yellow represent the additional atoms required to model the whole ("upper") active site.

```
T-COFFEE, Version_10.00.r1613 (2013-10-22 15:49:09 - Revision 1613 - Build 432)
Cedric Notredame
CPU TIME:0 sec.
SCORE=98
*
 BAD AVG GOOD
*
OXA-23      :  95
OXA-48      :  95
OXA-51      :  92
OXA-58      :  90
OXA-228     :  95
OXA-24      :  98
OXA-25      :  98
OXA-26      :  98
OXA-72      :  98
OXA-139     :  95
OXA-143     :  98
OXA-160     :  98
OXA-182     :  98
OXA-207     :  98
OXA-231     :  98
OXA-253     :  98
OXA-255     :  98
cons        :  98

OXA-23        1 M-NKYFTC-YVVAS--LFLSGCTV-QHNLINETPSQIVQ--GHNQVIHQYFDEKNTSGVLVIQTDKKINLYG   65
OXA-48        1 M-RVLALSAVFLVASIIGMPAVA------------KEWQ--ENKSWNAHFTEHKSQGVVVLWNENKQQGFT   56
OXA-51        1 M-N--IKT-LLLITSAIFISACSPYIVTANPNHSASKSD--EKAEKIKNLFNEVHTTGVLVIQQGQTQQSYG   66
OXA-58        1 --MKLLKI-LSLVCLSISIGACAEHSMSRAKTSTIPQVNNSIIDQNVQALFNEISADAVFVTYDGQNIKKYG   69
OXA-228       1 MKFKMKGL-FCVILSSLAFSGCVY-D-SKLQRPVISER-----VTEIPLLFNQAQTQAVFVTYDGIHLKSYG   64
OXA-24        1 M-KKFILP-IFSISILVSLSACSS-IKTKSEDNFHISSQ--QHEKAIKSYFDEAQTQGVIIIKEGKNLSTYG   67
OXA-25        1 M-KKFILP-IFSISILVSLSACSS-IKTKSEDNFHISSQ--QHEKAIKSYFDEAQTQGVIIIKEGKNLSTYG   67
OXA-26        1 M-KKFILP-IFSISILVSLSACSS-IKTKSEDNFHISSQ--QHEKAIKSYFDEAQTQGVIIIKEGKNLSTYG   67
OXA-72        1 M-KKFILP-IFSISILVSLSACSS-IKTKSEDNFHISSQ--QHEKAIKSYFDEAQTQGVIIIKEGKNLSTYG   67
OXA-139       1 M-KKFILP-IFSISILVSLSACSS-IKTKSEDNFHISSQ--QHEKAIKSYFDEAQTQGVIIIKEGKNLSTYG   67
OXA-143       1 M-KKFILP-ILSISTLLSVSACSS-IQTKFEDTFHTSNQ--QHEKAIKSYFDEAQTQGVIIIKKGKNISTYG   67
OXA-160       1 M-KKFILP-IFSISILVSLSACSS-IKTKSEDNFHISSQ--QHEKAIKSYFDEAQTQGVIIIKEGKNLSTYG   67
OXA-182       1 M-KKFILP-IFSISILLSLSACSS-IQTKFEDTFHISNQ--KHEKAIKSYFDEAQTQGVIIIKEGKNISSYG   67
OXA-207       1 M-KKFILP-IFSISILVSLSACSS-IKTKSEDNFHISSQ--QHEKAIKSYFDEAQTQGVIIIKEGKNLSTYG   67
OXA-231       1 M-KKFILP-ILSISTLLSVSACSS-IQTKFEDTFHTSNQ--QHEKAIKSYFDEAQTQGVIIIKKGKNISTYG   67
OXA-253       1 M-KKFILP-IFSISILLSLSACSS-IQTKFEDTSDISDQ--QQGKAIKSYFDEAQTQGVIIIKEGKNISTYG   67
OXA-255       1 M-KKFILP-IFSISTLLSLSACST-IQNKFEKTSDISDQ--QHEKAIKSYFDEAQTQGVIIIKEGKNIRIYG   67

cons          1                          : . .                        * :  : .*.:        :   72

OXA-23       66 NALSRANTEYVPASTFKMLNALIGLEN-QKTDINEIFKWKGEKRSFTAWEKDMTLGEAMKLSAVPVYQELAR  136
OXA-48       57 NNLKRANQAFLPASTFKIPNSLIALDLGVVKDEHQVFKWDGQTRDIATWNRDHNLITAMKYSVVPVYQEFAR  128
OXA-51       67 NDLARASTEYVPASTFKMLNALIGLEH-HKATTTEVFKWDGQKRLFPEWEKDMTLGDAMKASAIPVYQDLAR  137
OXA-58       70 THLDRAKTAYIPASTFKIANALIGLEN-HKATSTEIFKWDGKPRFFKAWDKDFTLGEAMQASTVPVYQELAR  140
OXA-228      65 NDLSRAKTEYIPASTFKMLNALIGLQN-AKATNTEVFHWNGEKRAFSAWEKDMTLAEAMQASAVPVYQELAR  135
OXA-24       68 NALARANKEYVPASTFKMLNALIGLEN-HKATTNEIFKWDGKKRTYPMWEKDMTLGEAMALSAVPVYQELAR  138
OXA-25       68 NALARANKEYVPASTFKMLNALIGLEN-HKATTNEIFKWDGKKRTYPMWEKDMTLGEAMALSAVPVYQELAR  138
OXA-26       68 NALARANKEYVPASTFKMLNALIGLEN-HKATTNEIFKWDGKKRTYPMWEKDMTLGEAMALSAVPVYQELAR  138
OXA-72       68 NALARANKEYVPASTFKMLNALIGLEN-HKATTNEIFKWDGKKRTYPMWEKDMTLGEAMALSAVPVYQELAR  138
OXA-139      68 NALARANKEYVPASTFKMLIALIGLEN-HKATTNEIFKWDGKKRTYPMWEKDMTLGEAMALSAVPVYQELAR  138
OXA-143      68 NNLTRAHTEYVPASTFKMLNALIGLEN-HKATTTEIFKWDGKKRSYPMWEKDMTLGDAMALSAVPVYQELAR  138
OXA-160      68 NALARANKEYVPASTFKMLNALIGLEN-HKATTNEIFKWDGKKRTYPMWEKDMTLGEAMALSAVPVYQELAR  138
OXA-182      68 NNLVRAHTEYVPASTFKMLNALIGLEN-HKATTNEIFKWDGKKRSYPMWEKDMTLGEAMALSAVPVYQDLAR  138
OXA-207      68 NALARANKEYVPASTFKMLNALIGLEN-HKATTNEIFKWDGKKRTYPMWEKDMTLGEAMALSAVPVYQELAR  138
OXA-231      68 NNLTRAHTEYVPASTFKMLNALIGLEN-HKATTTEIFKWDGKKRSYPMWEKDMTLGDAMALSAVPVYQELAR  138
OXA-253      68 NNLARAHTEYVPASTFKMLNALIGLEN-HKATTTEIFKWDGKKRSYPMWEKDMTLGDAMALSAVPVYQELAR  138
OXA-255      68 NNLVRAHTEYVPASTFKMLNALIGLEN-HKATTTEIFKWDGKKRSYPMWEKDMTLGDAMALSAVPVYQELAR  138

cons         73 . * **   ::******:  :**.*:                ::*:*.*: *    *::* .*  **  *.:****::** 144
```

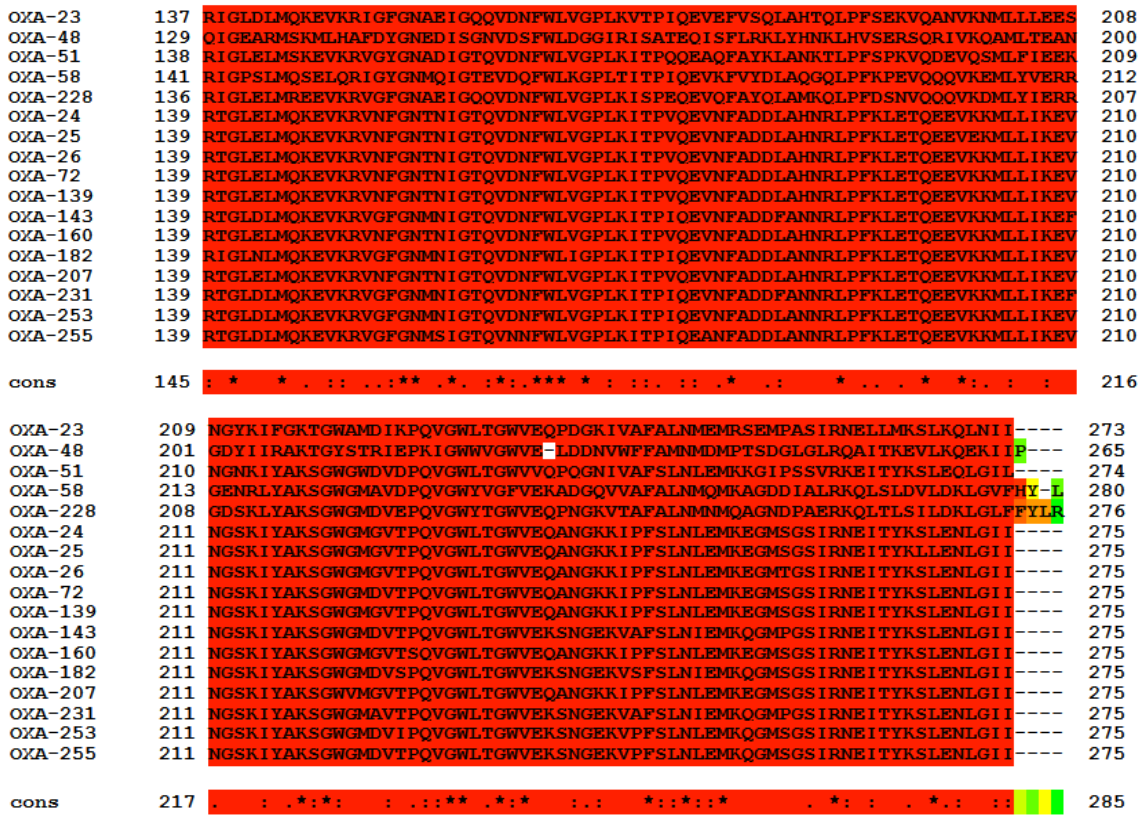

Fig. 37: M-Coffee Multiple Sequence Alignment of Class D CPases. Values at top represent percent of residues aligned identically between all multiple sequence alignment methods. Individual residues are color-coded accordingly: red indicates perfect alignment agreement between all methods, blue indicates the lowest agreement.

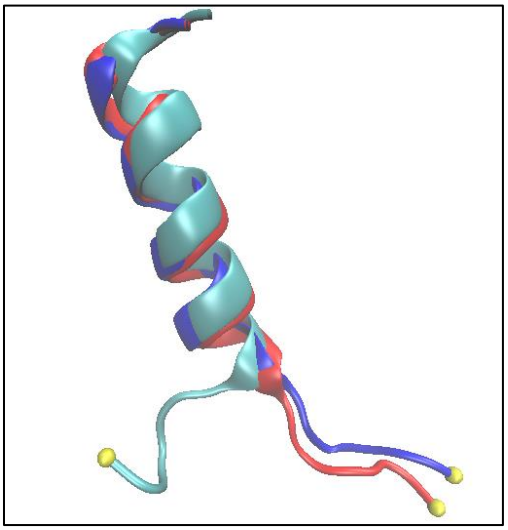

Fig. 38: G224D N-Terminal Outlier Structures. *Light blue*: Reference frame. *Dark Blue*: Peak present at ~5nsec in Figure 9. *Red*: Peak present at ~17nsec in Figure 9. Cα atoms of the N-terminal residue are colored yellow.

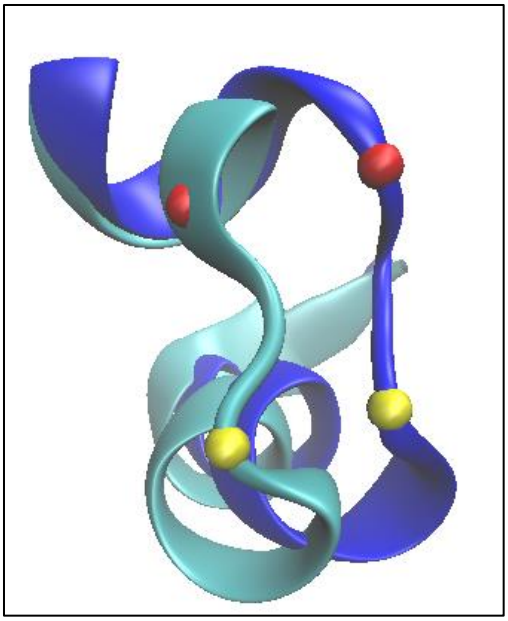

Fig. 39: M223A Ser128, Val130 Outlier Structures. *Light blue*: Reference frame. *Dark Blue*: Peak present at ~7nsec in Figure 11 Other Active Site Residues Cα Atoms. Ser128 Cα atoms are colored yellow. Val130 Cα atoms are colored red.

	WT Avg. (Å)	M223A Avg. (Å)	G224D Avg. (Å)	P227S Avg. (Å)
Ala80Cα - Gly222Cα	6.12 ±0.73	5.17 ±0.27	5.40 ±0.31	5.29 ±0.32
Ala80Cα - Leu168Cα	4.65 ±0.33	4.50 ±0.34	4.61 ±0.29	4.81 ±0.52
Ala80Cα - Trp221Cα	7.46 ±0.89	6.24 ±0.30	6.57 ±0.40	6.15 ±0.28
Ala88Cα - Val201Cα	6.97 ±0.29	7.21 ±0.35	7.13 ±0.43	7.12 ±0.33
Arg138Cα - Asp164Cα	6.72 ±0.34	6.73 ±0.42	6.67 ±0.37	6.58 ±0.42
Arg138NH2 - Asp164OD1	3.57 ±0.93	3.64 ±1.00	3.65 ±0.95	3.58 ±0.96
Asn87Cα - Tyr133Cα	7.16 ±0.22	7.22 ±0.24	7.25 ±0.24	7.26 ±0.24
Asn87ND2 - Tyr133O	3.17 ±0.26	3.13 ±0.26	3.20 ±0.28	3.25 ±0.31
Gln134Cα - Asp164Cα	6.04 ±0.42	6.04 ±0.47	5.78 ±0.46	5.94 ±0.40
Gln134NE2 - Asp164O	3.36 ±0.76	3.48 ±0.88	3.35 ±0.81	3.71 ±1.12
Glu76Cα - Ile174Cα	5.61 ±0.33	5.12 ±0.27	5.06 ±0.27	5.28 ±0.26
Glu93Cα - Phe193Cα	6.70 ±0.31	6.56 ±0.27	6.61 ±0.29	6.53 ±0.27
Glu101Cα - Arg139Cα	14.04 ±0.34	15.48 ±1.14	14.33 ±0.81	13.95 ±0.36
Ile159Cα - Ile174Cα	12.08 ±0.31	11.90 ±0.31	11.96 ±0.30	12.01 ±0.32
Ile159Cα - Leu172Cα	5.45 ±0.28	5.39 ±0.29	5.46 ±0.28	5.45 ±0.30

Ile159Cα - Phe166Cα	5.91 ±0.31	5.92 ±0.36	5.89 ±0.34	5.78 ±0.28
KCX84Cα - Val130Cα	8.65 ±0.34	8.68 ±0.53	8.98 ±0.50	8.83 ±0.40
KCX84HZ1 - Val130CG2	3.32 ±0.76	5.32 ±1.23	5.35 ±1.49	4.51 ±0.88
KCX84OQ1 - Lys218NZ	2.82 ±0.68	3.70 ±1.01	2.81 ±0.56	6.31 ±1.69
KCX84OQ1 - Trp167HE1	6.96 ±0.90	8.20 ±1.43	7.70 ±0.98	4.73 ±2.16
KCX84Cα – Ser219Cα	10.50 ±0.43	9.98 ±0.25	10.72 ±0.43	9.82 ±0.32
Leu92Cα - Thr197Cα	6.42 ±0.28	6.37 ±0.29	6.59 ±0.43	6.44 ±0.30
Leu142Cα - Val163Cα	5.41 ±0.29	5.54 ±0.42	5.57 ±0.41	5.33 ±0.26
Leu168Cα - Arg261Cα	19.78 ±0.94	18.71 ±0.59	18.70 ±0.52	18.80 ±0.56
Leu168Cα - Glu251Cα	17.55 ±0.48	15.66 ±0.42	15.87 ±0.40	15.92 ±0.38
Leu168Cα - Gly222Cα	7.94 ±1.07	6.45 ±0.44	6.59 ±0.38	6.71 ±0.37
Leu168Cα - Gly/Asp224Cα	7.85 ±0.97	6.78 ±0.70	7.05 ±0.47	6.68 ±0.78
Leu168Cα - Met/Ala223Cα	9.36 ±1.09	8.18 ±0.52	8.25 ±0.36	8.13 ±0.47
Leu168CD2 - Arg261NH2	12.87 ±1.31	12.42 ±1.39	11.74 ±0.86	13.75 ±1.36
Lys75Cα - Thr175Cα	5.65 ±0.21	5.56 ±0.21	5.58 ±0.23	5.59 ±0.21
Met/Ala223Cα - Arg261Cα	14.88 ±0.48	14.70 ±0.46	14.67 ±0.46	14.68 ±0.50
Met/Ala223Cα - Gln228Cα	5.38 ±0.35	5.08 ±0.32	5.34 ±0.32	5.35 ±0.34
Met/Ala223Cα - Glu251Cα	10.71 ±0.37	10.31 ±0.33	10.67 ±0.37	10.55 ±0.37
Phe83Cα - Trp167Cα	6.69 ±0.24	6.76 ±0.30	6.68 ±0.23	6.94 ±0.35
Phe154Cα - Ile159Cα	10.23 ±0.32	10.31 ±0.34	10.25 ±0.33	10.32 ±0.32
Phe154Cα - Leu168Cα	15.02 ±0.40	15.11 ±0.40	14.74 ±0.37	15.26 ±0.43
Phe154Cα - Phe166Cα	13.09 ±0.37	13.26 ±0.38	12.95 ±0.38	12.99 ±0.32
Phe154Cα - Trp167Cα	11.52 ±0.40	11.74 ±0.40	11.25 ±0.38	11.79 ±0.39
Phe154Cα - Val163Cα	15.56 ±0.38	15.79 ±0.48	15.50 ±0.44	15.60 ±0.37
Phe166Cα - Ile174Cα	12.24 ±0.27	12.52 ±0.29	12.26 ±0.27	12.43 ±0.26
Phe166Cα - Leu172Cα	6.36 ±0.34	6.34 ±0.36	6.20 ±0.35	6.22 ±0.26
Pro79Cα - Leu172Cα	7.45 ±0.25	7.52 ±0.25	7.53 ±0.24	7.44 ±0.27
Pro/Ser227Cα - Glu251Cα	6.99 ±0.35	7.01 ±0.28	7.20 ±0.34	7.06 ±0.27
Pro/Ser227CB - Glu251CD	4.29 ±0.56	4.27 ±0.47	4.56 ±0.63	4.15 ±0.45
Pro227CG - Glu251OE1	4.84 ±0.84	4.91 ±0.89	5.20 ±1.05	N/A

Pro227CG - Glu251OE2	4.71 ±0.80	4.85 ±0.88	5.15 ±0.99	N/A
Ser81Cα - Gly220Cα	4.87 ±0.25	4.70 ±0.24	4.83 ±0.20	4.61 ±0.25
Ser81Cα - Ser128Cα	7.90 ±0.52	8.77 ±0.48	8.09 ±0.43	7.51 ±0.82
Ser81Cα – Tyr112Cα	16.20 ±0.91	17.21 ±0.96	17.22 ±1.79	15.79 ±0.96
Ser81CA - Val130Cα	8.60 ±0.54	8.72 ±0.52	8.74 ±0.57	8.55 ±0.46
Ser81Cα - Val130CB	8.21 ±0.59	8.23 ±0.70	8.50 ±0.74	8.32 ±0.62
Ser81HG1 - KCX84OQ2	2.91 ±1.42	4.64 ±1.06	1.89 ±0.38	3.69 ±1.12
Ser128Cα - Ser219Cα	8.74 ±0.57	10.66 ±0.77	9.41 ±0.64	9.65 ±0.71
Ser128OG - Ser219OG	6.77 ±0.88	8.63 ±1.33	7.72 ±0.82	7.35 ±1.27
Ser219Cα - Arg261Cα	7.68 ±0.38	7.88 ±0.42	7.40 ±0.38	7.82 ±0.41
Ser219CB - Trp221CB	7.49 ±0.29	7.34 ±0.28	7.60 ±0.27	7.28 ±0.28
Ser219OG - Arg261NH2	3.57 ±0.58	3.68 ±0.68	3.52 ±0.59	3.60 ±0.68
Ser227HG1 - Glu251OE1	N/A	N/A	N/A	3.04 ±1.13
Ser227HG1 - Glu251OE2	N/A	N/A	N/A	3.03 ±1.08
Ser227OG - Glu251OE1	N/A	N/A	N/A	3.85 ±1.01
Ser227OG - Glu251OE2	N/A	N/A	N/A	3.84 ±0.97
Thr51OG1 - Glu251O	2.77 ±0.15	2.76 ±0.15	2.80 ±0.19	2.79 ±0.16
Trp167Cα - Ile174Cα	9.66 ±0.27	10.07 ±0.30	9.74 ±0.25	10.08 ±0.25
Trp167Cα - Leu172Cα	5.96 ±0.39	5.86 ±0.39	5.74 ±0.38	5.88 ±0.35
Tyr77Cα - Ile174Cα	5.49 ±0.15	5.52 ±0.15	5.51 ±0.15	5.54 ±0.14
Tyr77Cα - Lys173Cα	5.52 ±0.24	5.25 ±0.22	5.17 ±0.21	5.33 ±0.23
Tyr77N - Ile174O	2.94 ±0.14	2.96 ±0.15	2.94 ±0.14	2.91 ±0.19
Tyr77O - Ile174N	2.83 ±0.12	2.89 ±0.13	2.86 ±0.12	2.91 ±0.14
Tyr112OH - Met114SD	7.87 ±1.20	8.17 ±0.63	8.87 ±2.68	8.33 ±0.90
Tyr112Cα - Met/Ala223Cα	15.03 ±1.63	18.19 ±1.28	15.85 ±1.92	16.23 ±1.39
Tyr112Cα - Ser128Cα	10.50 ±0.55	10.47 ±0.59	10.87 ±1.31	10.56 ±0.51
Tyr112CZ - Ser128CB	8.54 ±1.02	8.69 ±1.14	9.41 ±2.37	8.83 ±0.91
Tyr112OH - Met223CE	6.35 ±3.13	N/A	8.41 ±3.68	6.89 ±1.80
Val78Cα - Gly170Cα	6.09 ±0.33	6.12 ±0.39	6.08 ±0.27	5.97 ±0.29
Val78Cα - Val225Cα	9.11 ±0.89	8.24 ±0.40	8.09 ±0.27	8.17 ±0.34

Val130Cα - Leu168Cα	10.00 ± 0.58	11.19 ±0.67	9.88 ±0.51	10.73 ±0.67
Val130CG2 - Leu168CD2	5.67 ±0.91	7.57 ±1.12	5.48 ±0.73	7.65 ±1.54
Val163Cα - Ile174Cα	17.34 ±0.27	17.61 ±0.37	17.39 ±0.28	17.66 ±0.36
Val163Cα - Leu172Cα	11.19 ±0.27	11.31 ±0.33	11.18 ±0.26	11.35 ±0.34
Val163Cα - Phe166Cα	6.22 ±0.23	6.37 ±0.30	6.36 ±0.22	6.50 ±0.29
Val163Cα - Gly/Asp224Cα	7.87 ±1.39	6.43 ±0.88	6.42 ±0.39	6.24 ±0.58
Val163Cα - Val225Cα	8.92 ±1.44	6.61 ±0.83	6.45 ±0.48	6.34 ±0.50
Val163CG1 - Gly/Asp224CA	7.80 ±2.00	6.43 ±0.88	5.28 ±0.48	4.73 ±0.73

Table 16: Average Distances of WT & Mutants. Measurements were calculated using a 1 nsec equilibration period.